

Vol. 37 / 1&2
January, 2025

ISRAPS Bulletin

NSRP-2025, SPECIAL ISSUE



Guest Editor
Dr. Juby K Ajish

A Publication of
**Indian Society for
Radiation and Photochemical Sciences**

ASTRELLA (FEMTOSECOND AMPLIFIER)



Applications:

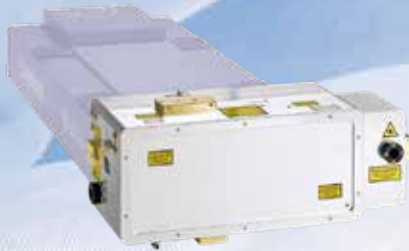
- Time-resolved Spectroscopy
- Multidimensional Spectroscopy



I-OPA (INDUSTRIAL GRADE OPTICAL PARAMETRIC AMPLIFIER)

Applications:

- Time-resolved Spectroscopy
- Multi-dimensional Spectroscopy



PULSED DYE LASER LIOPSTAR



Applications:

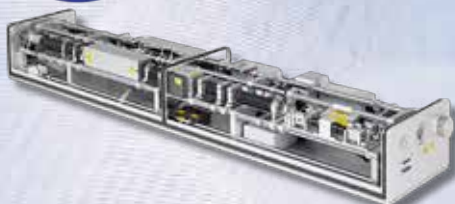
- Laser-induced fluorescence: LIF
- Light detection and ranging: LIDAR



LITRON LPY SERIES HIGH ENERGY LASER

Applications:

- OPO Pumping
- Dye Laser Pumping
- Spectroscopy



Message from the President and Secretary, ISRAPS

Dear ISRAPS members,

Warm greetings from the Executive Council of ISRAPS!

As we step into 2025, we extend our heartfelt wishes for a prosperous and successful New Year. This is also an opportune moment to express our gratitude for your unwavering support and enthusiastic participation in ISRAPS activities throughout the past year.

We are pleased to announce that one of ISRAPS's flagship biennial events, the National Symposium on Radiation and Photochemistry (NSRP), will be hosted at the National Institute of Science Education and Research (NISER), Bhubaneswar, from January 23–25, 2025. To commemorate this occasion, the ISRAPS Bulletin (NSRP-2025 Special Issue) will feature articles authored by eminent scientists invited to the symposium. This special issue captures recent advancements in radiation and photochemistry and reflects the collective expertise of our community. We extend our deepest thanks to Dr. Juby K. Ajish, the Guest Editor, for her diligent efforts in editing this scientifically enriching bulletin, which includes seven diverse articles highlighting cutting-edge techniques in radiation and photochemistry. We also acknowledge the invaluable contributions of all authors who made this publication an informative and engaging resource.

ISRAPS remains committed to fostering the dissemination of knowledge and promoting advanced research in radiation and photochemistry and its interdisciplinary applications, including spectroscopy, nanomaterials, atmospheric chemistry, supramolecular chemistry, radiation polymerization, radiation biology, medicine, and more.

Continuing our tradition of advancing academic discourse, ISRAPS recently organized the Discussion Meeting-Cum-One Day Symposium on "*Spectroscopy Across Energy Domains: From Fundamentals to Applications*" on September 28, 2024, at the Department of Chemistry, IIT Hyderabad. The event was graced by experts from leading research groups who delivered insightful talks. We express our sincere thanks to all participants and extend special gratitude to Prof. Krishna Gavvala for his pivotal role in ensuring the success of this meeting.

Once again, we deeply appreciate the constant support, encouragement, and active involvement of all our members. Your contributions are vital to the success of ISRAPS initiatives. We look forward to receiving your valuable suggestions and seeing your enthusiastic participation in our upcoming events. Researchers are also kindly requested to become ISRAPS members and actively contribute to its growth.

Wishing you all an inspiring and productive year ahead!

Sincerely,



Dr. A.C. Bhasikuttan
President, ISRAPS



Dr. P. Mathi
Secretary, ISRAPS



ISRAPS Bulletin

A Publication of
Indian Society for Radiation and Photochemical Sciences

Editor's Desk...

I am excited to present this special issue of the ISRAPS Bulletin, dedicated to "Advancements in Radiation and Photochemistry for Sensor Development, Molecular Design, and Studying Reactor Materials." This issue celebrates the auspicious occasion of the biennial 16th National Symposium on Radiation and Photochemistry (NSRP-2025), organized at the National Institute of Science Education and Research (NISER) Bhubaneswar, Odisha, from January 23-25, 2025.

This edition, containing seven articles, brings together groundbreaking research and insights from experts in the field, highlighting the pivotal role of radiation and photochemical processes in studies of both condensed and gas phases, as well as enhancing our understanding and ability to innovate within these critical areas.

In the realm of sensor development, photochemistry has paved the way for novel sensing technologies that significantly improve the accuracy and efficiency of detecting various stimuli. Meanwhile, advancements in molecular design have opened new avenues for creating customized materials, such as carbon dots and rare earth phosphors, that respond intelligently to environmental changes. Additionally, one of the articles discusses the study of reactor materials under radiation exposure, which is crucial for ensuring the safety and efficiency of nuclear systems. This issue explores the latest findings in this vital aspect of materials science. This bulletin features two articles on colorimetric and fluorometric sensors, one on the application of carbon dots as photosensitizers, and another on the design of defect-engineered intrinsic white light-emitting non-rare earth phosphors. The remaining two articles focus on the conformational study of peptides and single-particle-level studies of quantum dots.

As we delve into the contributions from our esteemed authors, we hope to inspire continued exploration and collaboration within this dynamic intersection of disciplines. We invite you to engage with the articles and reflect on the implications of these advancements for future research and practical applications.

On behalf of ISRAPS, I sincerely acknowledge the cooperation of all the contributors, and we hope you enjoy this enlightening edition. I also thank ISRAPS for entrusting this editorial responsibility to me.

Juby K Ajish (Guest Editor)

Radiation & Photochemistry Division
Bhabha Atomic Research Centre, Mumbai, INDIA



Juby K. Ajish joined the Bhabha Atomic Research Centre (BARC) in 2010 after graduating from the 53rd batch of the BARC Training School. She received her MSc from Calicut University in 2008 and completed her Ph.D. at the Homi Bhabha National Institute in Mumbai, India, in 2016. Her doctoral research focused on the "Synthesis and Study of Carbohydrate-Based Hydrogels for Biomedical Applications". Currently, Dr. Ajish is engaged in several significant projects relevant to the Department of Atomic Energy (DAE), alongside her directed research in the field of polymer chemistry. Her research interests encompass the fabrication of plastic scintillators and thin films for radiation detection, the synthesis of polymeric hydrogels for various biomedical applications, utilization of synthetic polymers and functionalized natural polymers for targeted drug delivery, and synthesis and application of glycopolymers in lectin recognition and bacterial detection.



INDIAN SOCIETY FOR RADIATION AND PHOTOCHEMICAL SCIENCES (ISRAPS)

EXECUTIVE COUNCIL (2024-2026)

President

Dr. A. C. Bhasikuttan

Vice-Presidents

Prof. Anindya Dutta

Dr. Yatender K. Bhardwaj

Secretary

Dr. P. Mathi

Jt. Secretary

Dr. Beena G. Singh

Treasurer

Dr. Sumana Sengupta

Executive Members

Dr. Atanu Barik

Dr. Awadhesh Kumar

Dr. Sukhendu Nath

Dr. Madhab C. Rath

Prof. Shamik Chakraborty

Dr. Amit Kunwar

Dr. Chandra N. Patra

Prof. Geeta K. Sharma

Dr. Ankur Saha

Dr. Sharmistha Dutta Choudhury

Dr. Jyotirmayee Mohanty

Dr. R. Puspalata

Dr. V. Sudarsan

Co-opted Members

Dr. Nihrendu Choudhury

Prof. Sriram K. Gundimeda

Dr. Nandita Maiti

Prof. Prakash D. Naik

Prof. Hirendra N. Ghosh

Dr. Manoj Kumbhakar

Prof. Jai P. Mittal

Prof. Anil K. Singh

Dr. Narender K. Goel

Prof. Avinash Kumbhar

Prof. Tulsi Mukherjee

Prof. Avesh K. Tyagi

Web Master

Dr. Abhishek Das and Shri. Subhamoy Saha

Contact details:

C/o Radiation & Photochemistry Division
Bhabha Atomic Research Centre, Mumbai-400085

E-mail: israps.secretary@gmail.com

Telephone:(022)- 25593771/25592668/25590302

Contents

Message from the President and Secretary, ISRAPS	i
Editor's Desk	iii
Probing conformational preferences of small peptides in condensed and gas phase <i>S. Kumar, S. Mandal and A. Das</i>	1
Versatility of Carbon Dots as a Photosensitizer <i>Somen Mondal</i>	14
Design of Defect Engineered Intrinsic White Light Emitting Non-Rare-Earth Phosphors: State-of-the-art <i>A. K. Dehury, R. Kainda, S. Khato, R. C. Mallick and Y. S. Chaudhary</i>	20
Water radiolysis and its impact on reactor materials <i>R. Puspallata, D. Mal, L. Muniyasamy, R. Ramakrishnan, S. Bera and T.V. Krishna Mohan</i>	34
Extensive Modulation of Fluorescence Quantum Yield in Quantum Dots by the Presence of Permanent Dark Particles: A Single Particle Level Study <i>K. Kaushik, C. Rao, A. Salam and C. K. Nandi</i>	42
Application of Pseudorotaxane and Rotaxane in Anion-Responsive Studies <i>M. Jaiswal and S. Dasgupta</i>	51
Unravelling Cyanide Sensing Mechanisms of Colorimetric and Fluorometric Sensors <i>G. L. P. Anisha, S. S. B. Rayudu, Dhananjay, R. K. Kanaparthi</i>	63

Probing conformational preferences of small peptides in condensed and gas phase

S. Kumar[#], S. Mandal[#], and A. Das^{**}

[#]Department of Chemistry, Indian Institute of Science Education and Research
Dr. Homi Bhabha Road, Pashan, Pune 411008, India

^{**}(email: a.das@iiserpune.ac.in)

Abstract

Conformational preferences of peptides are governed by hydrogen-bonding interactions in the backbone as well as specific amino acid residues present there. The three most important conformations or secondary structures of peptides are helices, sheets, and turns. Among these, turns play a unique role by reversing the direction of the polypeptide chains, facilitating diverse folding patterns. While well-known hydrogen-bonded rings such as C6, C7, C10, C13, and C15 in the peptide backbone are associated with δ , γ , β , α , and π turns, respectively, the weaker intraresidue C5 hydrogen bond, involving the N-H and carbonyl group of the same amino acid residue, has received comparatively less attention. Here, we have reviewed our understanding of the intrinsic conformational preferences of the C5 hydrogen bond in Z-Gly-Pro-OH dipeptide using gas phase spectroscopic techniques and quantum chemical calculations. Our findings reveal that the global minimum conformer observed in the experiment is stabilized by a weak intraresidue C5 hydrogen bond, while another higher energy observed conformer is folded through an OH... π interaction. To further investigate the sequence-dependent effects on peptide conformations, we examined the model systems Boc-Gly-^DPro-NHBn-OMe and Boc-^DPro-Gly-NHBn-OMe through NMR, FTIR, X-ray crystallography, and gas phase laser spectroscopy. Gas-phase spectroscopy identified three conformers for Boc-Gly-^DPro-NHBn-OMe and two conformers for Boc-^DPro-Gly-NHBn-OMe, while a dependence of the folding motifs of the two peptides with the change in the sequence is clearly observed. A similar result was observed from the condensed phase studies. This review signifies the critical role of backbone hydrogen bonds and sequence of residues in stabilizing specific peptide structures important for protein folding.

1. Introduction

Secondary structures of peptides or proteins generally provide the local folding pattern along the polypeptide chain.¹ Based on their hydrogen bonding network between the N-H and the carbonyl groups, secondary structures can be broadly classified as sheets, helices, and turns.²⁻⁶ Turns are one of the unique secondary structures as they are involved in the reversal of the direction of the polypeptide chain, which contributes to the specific folded structures of the proteins.⁷

Turns are classified into γ , β , α , and π types based on the inter-residue interactions between the backbone N-H and carbonyl groups of

the $i \rightarrow i + 2$, $i \rightarrow i + 3$, $i \rightarrow i + 4$, and $i \rightarrow i + 5$ residues, respectively. γ , β , α , and π types of turns result to the formation of C7, C10, C13, and C15 hydrogen-bonded rings, respectively.^{2,8} Although less explored in the literature, a relatively weak intraresidue C5 hydrogen bond does exist when the N-H and carbonyl groups of the same amino acid residue interact between each other.⁹ C5 hydrogen bonds are generally present in the β -strand or β -sheet structures of proteins. Although not named C5 hydrogen bond, Nyquist used IR spectroscopy in the solution phase to show that the trans conformer of N-alkyl α -halo/alkoxy acetamides is more stabilized compared to the cis conformer due to the formation of a five-membered hydrogen-bonded ring.¹⁰

Observation of C5 hydrogen bonds in small peptides containing Glycine such as Z-Gly-OH, Gly-Gly, and Ac-Gly-Phe-NH₂ using gas phase laser spectroscopy was reported in the literature.¹¹ Raines and co-workers demonstrated from their extensive Protein Data Bank (PDB) analysis that 94% of proteins contain C5 hydrogen bonds. They found that the s-type lone pair present on the carbonyl oxygen of the amide backbone in the β -sheet structures overlaps with the σ^* orbital of the N-H group, while the other p-type lone pair on the C=O oxygen interacts with the N-H group of the same residue forming a constrained C5 hydrogen bond.

The intrinsic property of peptides to form a particular secondary structure depends not only on specific amino acid residues but also on their particular sequences. Amino acids such as Gly, Pro, Asn, and Asp are found to have a higher propensity to form β -turns than helices and β -sheets.¹² It is also reported that the Pro-Gly sequence has a higher propensity to form β -turn conformation in proteins compared to the Gly-Pro sequence. On the other hand, Gly-Pro sequence is reported to prefer an extended polyproline type-II or β -strand conformation.¹³⁻¹⁵ β -turn conformation is also important for sites of enzymatic reactions, effective peptide-based drug design, peptidomimetics, catalysis, and self-assembly.¹⁶

Secondary structures of polypeptides are generally determined by investigating protected small peptides through FTIR (Fourier-transform infrared), 2D-NMR (nuclear magnetic resonance), and CD (circular dichroism) spectroscopy as well as X-ray crystallography.¹⁷⁻²¹ Gas phase spectroscopic techniques are also exploited to elucidate the intrinsic structures of small peptides in the absence of any solvent.²²⁻²⁶ Scheraga and co-workers have demonstrated through FTIR, CD, and temperature-dependent NMR spectroscopy that the dominant conformer of Pro-Gly peptides has β -turn structures in the solution phase, while the Gly-Pro peptides prefer β -strand or extended polyproline II type structures.¹⁴ Balram and co-

workers have shown that in the crystals of hexa-to-decapeptides, ^DPro-Gly moiety forms a type II' β -turn resulting in the β -hairpin conformation.²⁷⁻³⁰ Gellman and coworkers have also demonstrated that ^DPro-Gly sequence is very effective for the formation of the type II' β -turn that is a mandatory requirement for the β -hairpin formation.³¹

Here, we have presented a brief review of our understanding of the conformational preferences of several dipeptides containing Gly and Pro residues using several gas phase spectroscopic techniques, FTIR and 2D-NMR spectroscopy, X-ray crystallography, and quantum chemistry calculations. In the case of Z-Gly-Pro-OH (Z=benzyloxycarbonyl), we have explored the intrinsic conformational preferences of this dipeptide through gas phase laser spectroscopy and quantum chemical calculations. We have observed multiple conformers of this peptide in the gas phase experiment and demonstrated the importance of the weak intraresidue C5 hydrogen bond in stabilizing the global minimum conformer of the peptide. In the Z-Gly-Pro-OH peptide, both the N- and C- terminals were not capped. We further investigated the secondary structures of the capped dipeptides Boc-Gly-^DPro-NHBn-OMe and Boc-^DPro-Gly-NHBn-OMe by changing the sequence. Here, we studied sequence-dependent folding motifs of these two peptides employing 2D-NMR and FTIR spectroscopy, X-ray crystallography, and gas phase laser spectroscopy combined with quantum chemistry calculations. A schematic diagram of the chemical structures of all the peptides discussed in this paper is shown in **Figure 1**.

2. Methods

Experimental

The Z-Gly-Pro-OH was purchased from Sigma Aldrich, while other two peptides were synthesized according to the method reported earlier in the literature.³² Standard characterization methods such as ¹H NMR and HRMS are reported elsewhere.³³ NMR and IR spectra of

capped dipeptides in dilute CDCl_3 solution (Boc-DPro-Gly-NHBn-OMe and Boc-Gly-DPro-NHBn-OMe) were recorded using a standard FTIR-Bruker Vertex 70 spectrometer and 400 MHz NMR (Bruker-400) spectrometer, respectively. An APEX(II) DUO CCD diffractometer was used to get the crystal structure of the peptide.

A home-built laser desorption Time of Flight (TOF) mass spectrometer, described in detail elsewhere, was used to record the mass-selected conformation-specific electronic, and IR spectra of the peptides and other molecules in the gas phase.³³⁻³⁸ Here, a very brief description of the experimental setup and spectroscopic techniques are provided. In the case of Z-Gly-Pro-OH, a solid pellet of 2 mm thickness and 12 mm

diameter was made by mixing graphite and a sample and pressing in a hydraulic press (about 3 tons of pressure). After cutting through the center, one of the semicircular halves was mounted onto a sample holder connected to an XYZ manipulator allowing translation along the Z-axis. Desorption of Z-Gly-Pro-OH was done by focusing a 532 nm laser beam (500 $\mu\text{J}/\text{pulse}$) from an Nd:YAG laser (Continuum, Minilite-I, 10 Hz, 10 ns) through an optical fiber (400 μm core diameter) onto the solid pellet.^{39,40} In the case of the capped peptides Boc-DPro-Gly-NHBn-OMe and Boc-Gly-DPro-NHBn-OMe, the solid pellet was placed onto a rotating sample holder. A supersonically expanded Ar carrier gas was seeded into the desorbed peptide

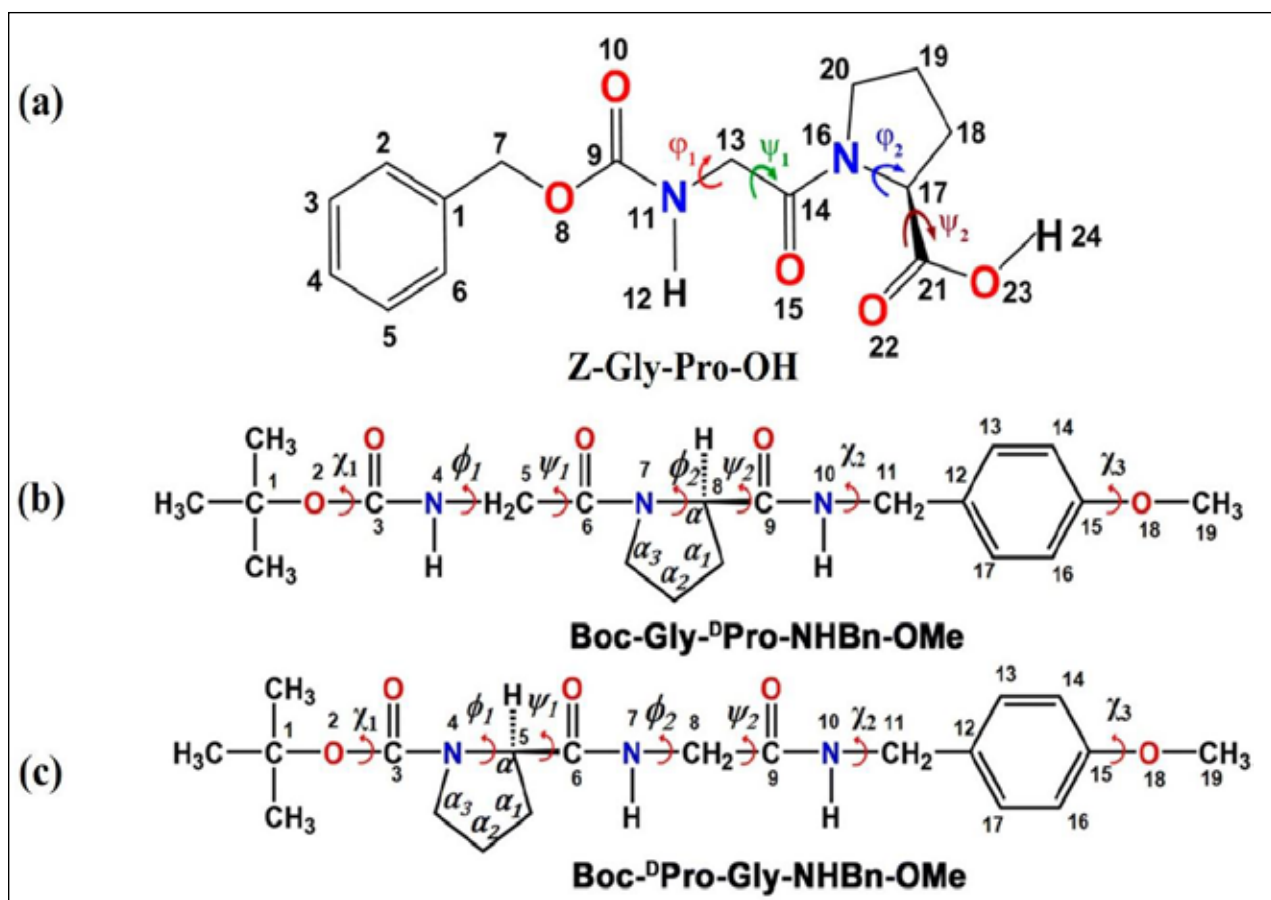


Figure 1. (a), (b), and (c) Chemical structures of Z-Gly-Pro-OH, Boc-Gly-^DPro-NHBn-OMe, and Boc-^DPro-Gly-NHBn-OMe peptides. Reproduced from ref. 33 and 34 with permission from [American Institute of Physics], Copyright [2019], and [Royal Society of Chemistry], copyright [2022], respectively.

molecules. The second harmonic output (0.2–0.3 mJ) of a tunable dye laser (ND6000, Continuum) pumped by frequency-doubled output of an Nd:YAG laser (10 nanoseconds, 10 Hz, Surelite II-10, Continuum) was scanned to measure the electronic spectrum of the peptide using resonant two-photon ionization (R2PI) technique. Discrimination of the presence of different conformers of the peptides was done by using UV-UV^{34, 41} and IR-UV hole-burning spectroscopy^{33, 34}, while conformation specific IR spectra were measured by resonant ion-dip infrared spectroscopy (RIDIRS)^{33, 34}.

Computational

A diverse set of conformers for Z-Gly-Pro-OH was generated using the Dreiding force field⁴², as implemented in the MarvinSketch software.⁴³ Geometry optimization and frequency calculations for conformers within 40 kJ/mol of the global minimum structure were performed using the Gaussian 09 software package.⁴⁴ Various levels of DFT theory were employed, including M05-2X/6-31+G(d), ω B97X-D/6-31++G(d,p), ω B97X-D/6-311++G(d,p), and M06-2X/6-311++G(d,p). The N-H and O-H stretching frequencies of the theoretically calculated conformers were scaled relative to previously reported data for Z-Gly-OH.

For the capped peptides Boc-^DPro-Gly-NHBn-OMe and Boc-Gly-^DPro-NHBn-OMe, hundreds of conformers were generated using the CONFLEX program with the MMFF94 force field.^{43, 45, 46} Conformers were grouped based on structural similarity and energy differences within 0.4 kJ/mol. Only the lowest-energy conformer from each group was selected for subsequent geometry and frequency optimization using the same Gaussian 09 and Gaussian 16 software.^{44, 47} Additional unique conformers were manually generated by rotating specific dihedral angles to introduce distinctive C7 hydrogen bonds and variations in the orientation of the benzyl

and methoxy groups. Significant numbers of conformers (50–70) were analyzed at different levels of theory, including M05-2X/6-31+G(d), B3LYP-D3/def2-TZVPP, ω B97X-D/def2-TZVPP, and B97-D3/def2-TZVPP. Redundant structures were discarded, and conformers within a 12 kJ/mol energy range were further optimized at the M06-2X/6-311++G(2d,2p) level of theory.

3. Results and Discussion

Z-Gly-Pro-OH: C5 hydrogen bond as a sole stabilizing interaction of the peptide backbone

Gas phase electronic and IR spectroscopy techniques combined with quantum chemistry calculations have been employed to explore the C5 hydrogen bonds as stabilizing interactions of the peptide backbone. Electronic spectrum of Z-Gly-Pro-OH measured in the S0-S1 region of the chromophore (Z-cap) using 1C-R2PI spectroscopy is presented in **Figure 2(a)**.³³ Several sharp bands

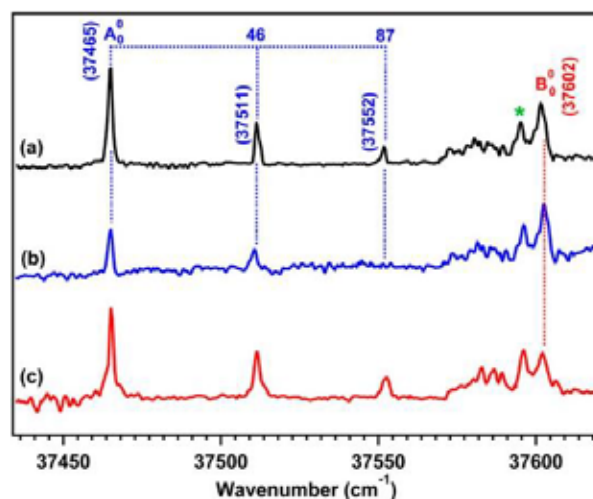


Figure 2. (a) Electronic spectrum of Z-Gly-Pro-OH recorded using the 1C-R2PI spectroscopic technique. (b, c) IR-UV hole-burning spectra of Z-Gly-Pro-OH obtained by fixing the IR laser to 3457 cm^{-1} and 3450 cm^{-1} , respectively. The band marked with an asterisk (37596 cm^{-1}) and the weak, broad feature on its red side did not produce any IR spectra or hole-burning signals. Reproduced from ref. 33 with permission from [American Institute of Physics], Copyright [2019].

are present in the electronic spectrum of Z-Gly-Pro-OH. Conformer-specific IR-UV hole-burning spectroscopy has been performed to determine the number of conformers contributing to all the bands observed in the electronic spectrum. **Figures 2(b) and 2(c)** display the IR-UV hole-burning spectra recorded by setting the IR laser to the N-H stretching frequencies of 3457 cm^{-1} and 3450 cm^{-1} , respectively, for Z-Gly-Pro-OH, while scanning the UV laser across the R2PI spectrum. The N-H stretching frequencies of 3457 cm^{-1}

and 3450 cm^{-1} are determined by fixing the UV laser at the 37465 cm^{-1} and 37602 cm^{-1} bands, respectively, in the electronic spectrum [**Fig. 2(a)**], using RIDIR spectroscopy as shown in **Figure 3**.

The hole-burning spectrum depicted in **Figure 2(b)** shows the depletion of the A_0^0 , $A_0^0 + 46$, and $A_0^0 + 87\text{ cm}^{-1}$ bands, which are assigned as conformer A. In contrast, the hole-burning spectrum displayed in **Figure 2(c)** shows the depletion of only the B_0^0 band termed as

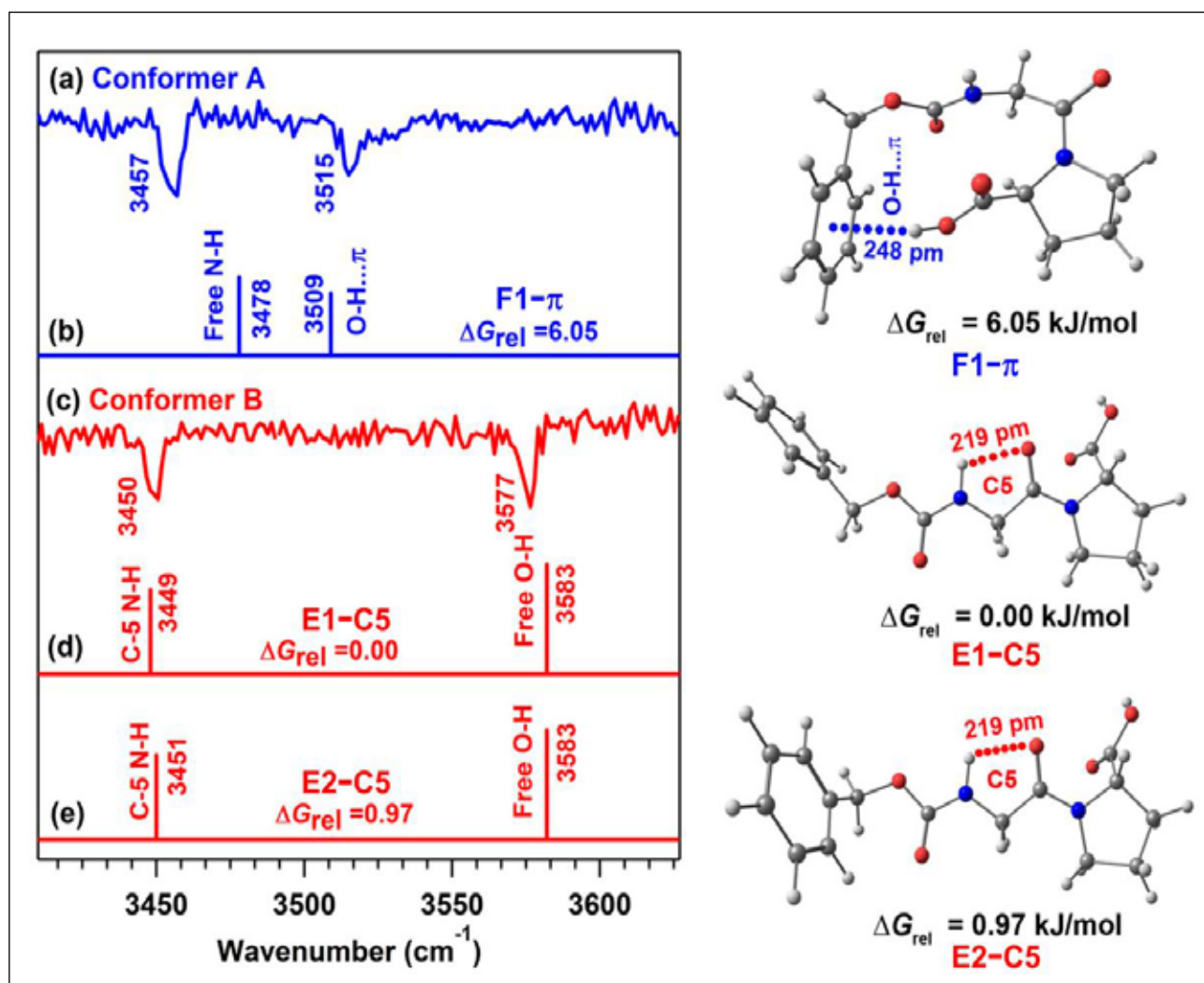


Figure 3. (a) and (c) Experimental IR spectra of different conformers of Z-Gly-Pro-OH obtained using RIDIR spectroscopy, with the UV laser fixed at 37465 cm^{-1} and 37602 cm^{-1} , respectively. (b), (d), (e) Scaled theoretical IR spectra of various conformers of Z-Gly-Pro-OH, along with their relative Gibbs free energy (ΔG_{rel} , in kJ/mol) values, calculated at the $\omega\text{B97X-D/6-31++G(d,p)}$ level of theory. The N-H and O-H stretching frequencies were scaled using factors of 0.944 and 0.933, respectively (see text for details). Reproduced from ref. 33 with permission from [American Institute of Physics], Copyright [2019].

conformer B. The band marked by an asterisk and a neighboring very broad feature in the electronic spectrum [Figure 2(a)] of Z-Gly-Pro-OH are insensitive in both the hole-burning spectra, and those bands could not provide also any IR spectrum. Hence, those electronic bands are unassigned.

The IR spectra of the conformers A and B of Z-Gly-Pro-OH in the N-H and O-H stretching region obtained by fixing the UV lasers at their respective origin bands are provided in Figure 3(a) and 3(c), respectively. It can be noticed in Figure 3 that the theoretical IR spectra of the global minimum conformer E1-C5 [Figure 3(d)] and the next higher energy conformer E2-C5 [Figure 3(e)] of Z-Gly-Pro-OH calculated at the ω B97X-D/6-31++G(d,p) level of theory match very well with the experimental IR spectrum of the conformer B provided in Figure 3(c). Hence, the most stable conformer of Z-Gly-Pro-OH observed in the experiment has an extended C5 hydrogen bonded structure. Conformer B could not be assigned to a single conformer as both theoretical conformers E1-C5 ($\Delta G_{\text{rel}} = 0.0$ kJ/mol) and E2-C5 ($\Delta G_{\text{rel}} = 0.97$ kJ/mol) are isoenergetic and have similar structures. This means either of them is observed experimentally. The bands at 3450 and 3577 cm^{-1} in the IR spectrum of conformer B [Figure 3(c)] are assigned as C5 hydrogen bonded N-H and free O-H stretching frequencies, respectively. The experimental IR spectrum of conformer A [Figure 3(a)] has a very good match with the theoretical IR spectrum of the conformer F1- π [Figure 3(b)], which is higher in energy by 6.05 kJ/mol with respect to the global minimum conformer. The F1- π conformer is folded through O-H... π hydrogen bonding interaction between the carboxylic OH group and phenyl ring in Z-Gly-Pro-OH. The 3515 and 3457 cm^{-1} IR bands of conformer A are assigned to the π -hydrogen bonded OH and free NH stretching frequencies, respectively, of Z-Gly-Pro-OH. The π -hydrogen bonded OH stretching frequency in conformer A is red-shifted by 62 cm^{-1} with respect to the free OH frequency of the C5

conformer. On the other hand, the NH frequency of the C5 conformer is red-shifted by 7 cm^{-1} in comparison to the free NH stretching frequency of the F1- π conformer. It is noteworthy that the extended C5 conformer is more stable than the folded F1- π conformer, most likely due to the larger entropic contribution to the former one. Hence, the spectroscopic studies of the Z-Gly-Pro-OH peptide demonstrate that the most stable conformer of a peptide can be stabilized solely due to the weak intraresidue C5 hydrogen bonds.

Boc-Gly-^DPro-NHBn-OMe vs Boc-^DPro-Gly-NHBn-OMe: Sequence dependent folding motifs of the peptides

Sequence dependent folding motifs of protected dipeptides have been explored using mass-selected electronic and vibrational spectroscopy, quantum chemistry calculations, 2D-NMR spectroscopy, and X-ray crystallography.

The electronic spectrum of Boc-Gly-^DPro-NHBn-OMe, recorded using the 1C-R2PI technique, is displayed in Figure 4(a). This spectrum reveals numerous sharp bands in the 35250–35600 cm^{-1} region. Figures 4(b–d) show UV-UV hole-burning spectra corresponding to the electronic bands marked as A_0^0 , B_0^0 , and C_0^0 , respectively, in Figure 4(a). The experiment

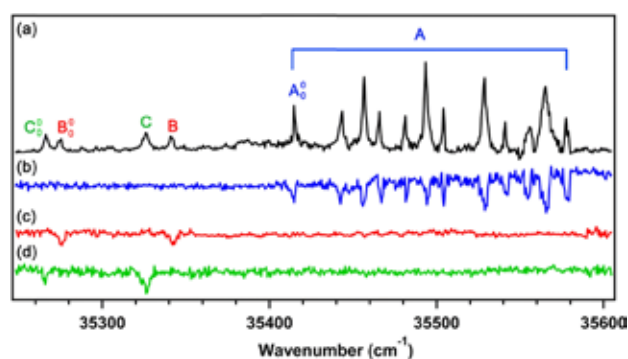


Figure 4. (a) Electronic spectrum of Boc-Gly-^DPro-NHBn-OMe recorded using the 1C-R2PI spectroscopic technique. (b–d) UV-UV hole-burning spectra of Boc-Gly-^DPro-NHBn-OMe obtained by fixing the pump UV laser at 35416, 35276, and 35267 cm^{-1} , respectively. Reproduced from ref. 34 with permission from [Royal Society of Chemistry], copyright [2022].

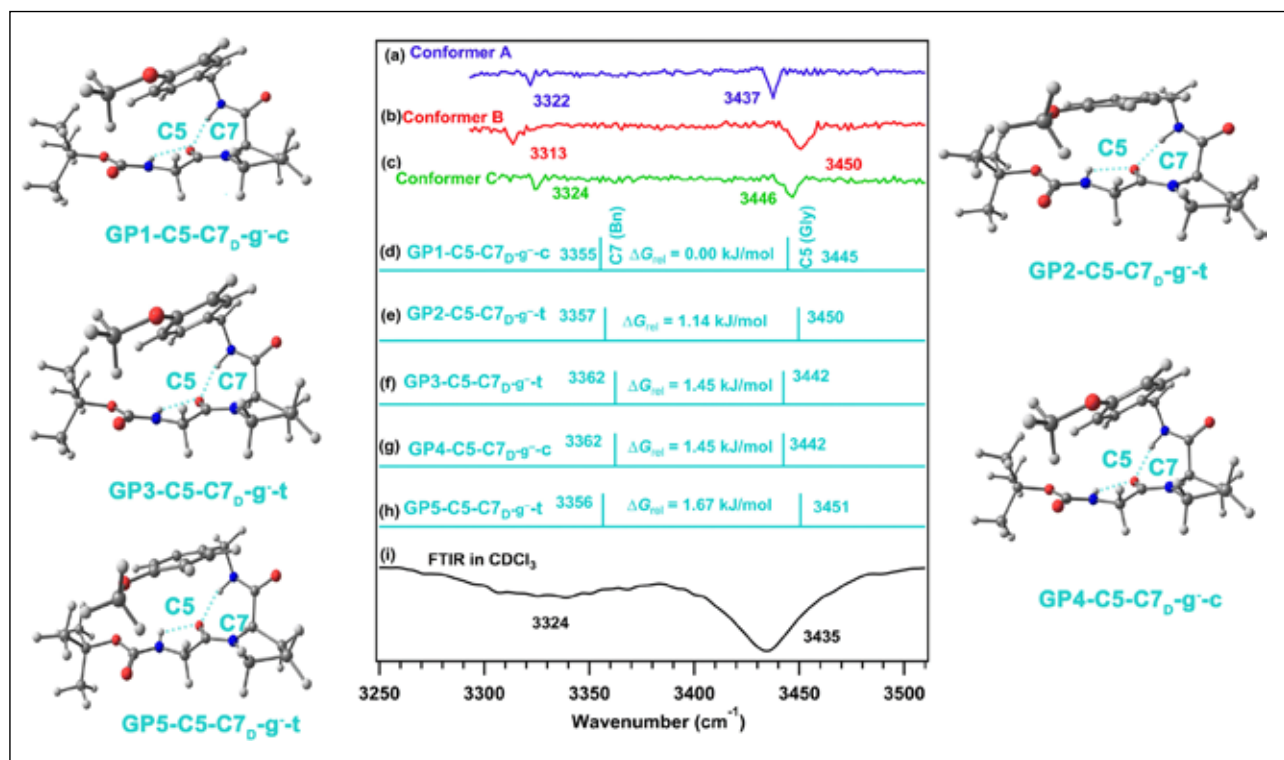


Figure 5. (a–c) Gas-phase IR spectra of conformers A, B, and C of Boc-Gly-^DPro-NHBn-OMe in the N–H stretching region, measured using RIDIR spectroscopy. (d–h) Scaled theoretical IR spectra of the conformers GP1–C5–C7_{D_{g-c}}, GP2–C5–C7_{D_{g-t}}, GP3–C5–C7_{D_{g-t}}, GP4–C5–C7_{D_{g-c}}, and GP5–C5–C7_{D_{g-t}} respectively, calculated at the M06-2X/6-311++G(2d,2p) level of theory. The theoretical harmonic N–H stretching frequencies of all conformers were scaled using a scaling factor of 0.948. (i) Solution-phase IR spectrum of Boc-Gly-^DPro-NHBn-OMe in the N–H stretching region, measured in CDCl₃ solvent. Reproduced from ref. 34 with permission from [Royal Society of Chemistry], copyright [2022].

identifies three conformers of the peptide, with the origin bands A₀⁰, B₀⁰, and C₀⁰ located at 35416 cm⁻¹, 35276 cm⁻¹, and 35267 cm⁻¹, respectively.

The IR spectra of Boc-Gly-^DPro-NHBn-OMe recorded in the N–H stretching region using RIDIR spectroscopy and theoretically calculated scaled IR spectra of low energy conformers of the peptide are shown in **Figure 5**. The IR spectra of the conformers A, B, and C reported in **Figure 5 (a–c)**, respectively, have been recorded by fixing the UV laser at the , , and bands of the electronic spectrum (**Figure 4a**) and scanning the IR laser in the region of N–H stretching frequency. **Figure 5(d–h)** represents the scaled theoretical stick diagram of five low-energy conformers of the peptide with the highest energy conformer of energy 1.67 kJ/mol with respect to the global minimum calculated at the M06-2X/6-311++G(2d,2p) level of theory. Experimentally

observed three conformers could not be directly assigned to a particular theoretical structure as all the five low energy conformers have similar energies and frequencies. However, all the five theoretical structures have C5–C7 backbone. Hence, it could be concluded that all the three observed conformers of Boc-Gly-^DPro-NHBn-OMe have C5–C7 folding motif with the Glycine N–H forming an intrasidue C5 hydrogen bond and the NHBn N–H involving in the C7 hydrogen bond with the Glycine C=O group.

The bands in the 3437–3450 cm⁻¹ region in the experimental IR spectra of the three conformers are assigned to the C5 hydrogen bonded Gly N–H, while the IR band in the 3313–3324 cm⁻¹ region in the spectra correspond to the C7 hydrogen bonded NHBn group. The solution phase IR spectrum of Boc-Gly-^DPro-NHBn-OMe recorded in CDCl₃ has been shown in **Figure 5(i)**. It is

anticipated to have broad IR bands in the solution phase FTIR spectrum, and hence, the presence of multiple conformers of the peptide cannot be identified there, unlike the gas phase spectrum. However, the peak positions of the two broad bands at 3324 and 3435 cm^{-1} in the FTIR spectrum are quite similar to the ones observed in the gas phase.

The electronic and IR-UV hole-burning spectra of Boc-^DPro-Gly-NHBn-OMe are presented in **Figure 6**. Several sharp peaks are found in the electronic spectrum of Boc-^DPro-Gly-NHBn-OMe shown in **Figure 6(a)**. **Figures 6(b)** and (c) display the IR-UV hole-burning spectra of the Pro-Gly peptide obtained by fixing the IR laser at the glycine N-H frequency of the conformers A (3411 cm^{-1}) and B (3391 cm^{-1}), respectively. Two conformers (A and B) of the peptide are identified from the hole-burning spectra.

The IR spectra of the two conformers of Boc-^DPro-Gly-NHBn-OMe recorded using RIDIR spectroscopy have been shown in **Figure 7**. A comparison between the experimental N-H stretching frequencies (**Figures 7a and c**) with the scaled theoretical IR spectra (**Figures 7b and d**)

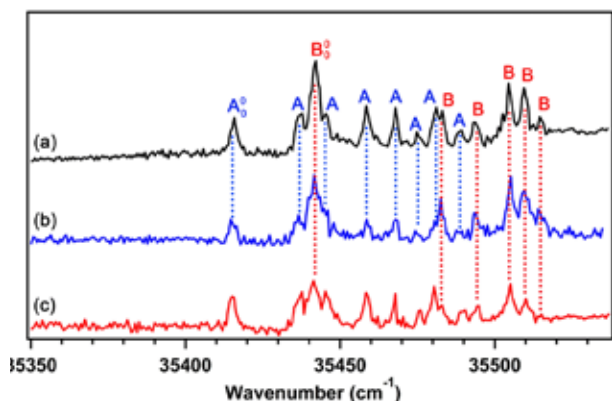


Figure 6. (a) Electronic spectrum of Boc-^DPro-Gly-NHBn-OMe recorded using the 1C-R2PI spectroscopic technique. (b, c) IR-UV hole-burning spectra of Boc-^DPro-Gly-NHBn-OMe obtained by fixing the pump IR laser at the N-H stretching frequencies of 3346 cm^{-1} and 3365 cm^{-1} , respectively. Reproduced from ref. 34 with permission from [Royal Society of Chemistry], copyright [2022].

calculated at the M06-2X/6-311++G(2d,2p) level of theory suggests that both the conformers have C7_D-C7_L structure. The only structural difference of the two observed conformers is about the *cis* and *trans* orientation of the -OMe group of the phenyl ring. The 3346 and 3365 cm^{-1} bands in the two experimental IR spectra are assigned to the C7 hydrogen bonded Gly N-H, while the 3391 and 3411 cm^{-1} bands are assigned to the C7 hydrogen bonded NHBn N-H group of the two observed conformers.

The FTIR spectrum of the Boc-^DPro-Gly-NHBn-OMe peptide depicted in Figure 7e shows two broad peaks centered at 3336 and 3436 cm^{-1} . Although the gas phase IR spectra indicate the absence of the C10 conformer of the Pro-Gly peptide, slightly different FTIR spectrum of the

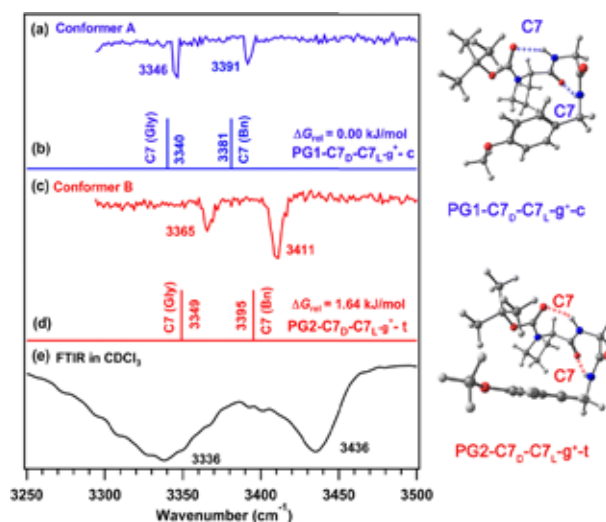


Figure 7. (a and c) Gas-phase IR spectra of conformers A and B of Boc-^DPro-Gly-NHBn-OMe in the N-H stretching region, measured using RIDIR spectroscopy. (b, d) Scaled theoretical IR spectra of conformers PG1-C7_D-C7_{L-g+c} and PG2-C7_D-C7_{L-g-t} respectively, calculated at the M06-2X/6-311++G(2d,2p) level of theory. The theoretical harmonic N-H stretching frequencies were scaled using a scaling factor of 0.948. (e) Solution-phase IR spectrum of Boc-^DPro-Gly-NHBn-OMe in the N-H stretching region, measured in CDCl₃ solvent. Reproduced from ref. 34 with permission from [Royal Society of Chemistry], copyright [2022].

peptide qualitatively hints towards the presence of the C10 conformer or both C7-C7 and C10 conformers in the solution phase.

To accurately determine the structure of both Gly-Pro and Pro-Gly peptides in the solution phase, we have recorded 2D-NMR spectra of Boc-Gly-^DPro-NHBn-OMe and Boc-^DPro-Gly-NHBn-OMe in CDCl₃ solution. **Figure 8** shows the partial ROESY (Rotating Frame Overhauser Effect Spectroscopy) spectra of both the peptides in the CDCl₃ solution recorded using a 400 MHz NMR spectrometer. Correlations between various

protons obtained from the ROESY spectrum aid in the prediction of the 3D conformation of the peptides in solution phase. Cross-correlation between glycine (3.92 ppm) and proline CH₂ (3.39 ppm) protons of the Gly-Pro peptide shown in **Figure 8(a)** suggests that Glycine N-H is involved in a weak intraresidue C5 hydrogen bond whereas NHBn N-H is involved in C7 hydrogen bond with the carbonyl group of glycine residue.

The partial ROESY spectrum of Boc-^DPro-Gly-NHBn-OMe provided in **Figure 8(b)** shows cross-correlations between Gly_{NH} (6.93

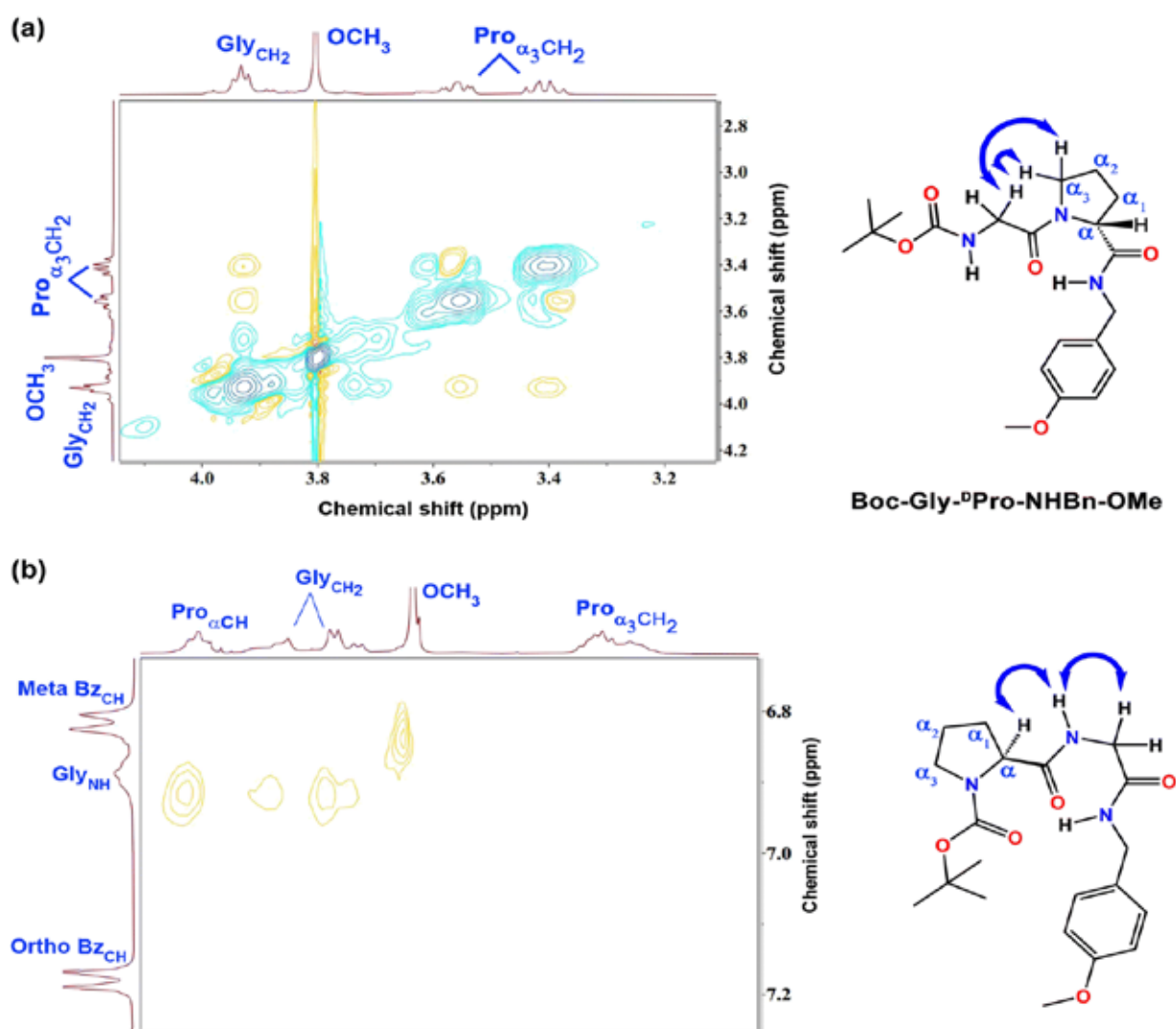


Figure 8. Partial ROESY spectra of (a) Boc-Gly-^DPro-NHBn-OMe and (b) Boc-^DPro-Gly-NHBn-OMe, recorded in CDCl₃ solvent. Reproduced from ref. 34 with permission from [Royal Society of Chemistry], copyright [2022].

ppm) and Gly_{CH₂} (3.90, 4.00 ppm) protons along with cross-correlations between Gly_{NH} (6.93 ppm) and Pro α_{CH} (4.20 ppm) protons. The C10 structure shown in **Figure 8b** matches with cross-correlations between various protons obtained from the 2D-NMR spectrum. Hence, 2D-NMR spectroscopy demonstrates that Pro-Gly peptide prefers a C10 structure in the solution phase

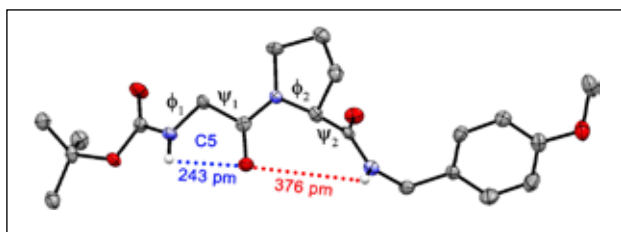


Figure 9. ORTEP diagram of the crystal structure of Boc-Gly-^DPro-NHBn-OMe, with thermal ellipsoids shown at the 50% probability level. For clarity, only the N-H hydrogen atoms are included. Reproduced from ref. 34 with permission from [Royal Society of Chemistry], copyright [2022].

whereas the observed structure in the gas phase is C7-C7.

This suggests that solvent plays an important role in the stabilization of the C10 structure in the solution phase whereas the gas phase is free of any external perturbations.

Furthermore, we attempted to determine the structures of the two dipeptides in the solid-state using X-ray crystallography, but we got the crystal structure of only the Gly-Pro peptide. The crystal structure of Boc-Gly-^DPro-NHBn-OMe was obtained by a slow evaporation of the peptide dissolved mixed solvent of ethyl acetate and n-hexane over a period of couple of days. Single crystal XRD of Boc-Gly-^DPro-NHBn-OMe was obtained using APEX(II) DUO CCD diffractometer. A good quality crystal, fit for diffraction could not be obtained for Boc-^DPro-Gly-NHBn-OMe. The crystal structure of Boc-Gly-^DPro-NHBn-OMe has been shown in

Table 1. Ramachandran angles and other important geometrical parameters of one of the observed structures of the Gly-Pro and Pro-Gly peptides in the gas phase along with the crystal structure of Gly-Pro

Geometrical parameters	Gly-Pro		Pro-Gly
	Crystal structure	Gas phase structure (GP1-C5-C7 _D -g-c)	Gas phase structure (PG1-C7 _D -C7 _D -g ⁺ -c)
ϕ_1 (°)	150	-155	86
ψ_1 (°)	-177	174	-64
ϕ_2 (°)	-79	84	-80
ψ_2 (°)	143	-72	72
χ_1 (°)	-167	178	176
χ_2 (°)	-99	-68	86
χ_3 (°)	9	-2	-1
C5 H-bond distance (pm)	243	215	-
C5 H-bond angle (°)	99	106	-
C7 (1 st) H-bond distance (pm)	376	198	196
C7 (1 st) H-bond angle (°)	85	148	149
C7 (2 nd) H-bond distance (pm)	-	-	203
C7 (2 nd) H-bond angle (°)	-	-	145

Figure 9. The crystal structure of the Gly-Pro peptide has a similar extended structure with C5-C7 interaction to the one observed in the gas phase and solution phase.

Table 1 shows the Ramachandran angles and other important geometrical parameters of one of the observed structures of the Gly-Pro and Pro-Gly peptides in the gas phase along with the crystal structure of Gly-Pro. We find that the j_1 , γ_1 , and j_2 values of the crystal structure of Boc-Gly-^DPro-NHBn-OMe match well with the corresponding gas phase observed structures, while γ_2 deviates significantly. This change in γ_2 between the gas phase and crystal structures may arise due to the crystal packing which includes intermolecular interactions between multiple units. Hence, the extended β -strand structure of Gly-Pro is maintained throughout solution, crystal, and gas phase with slight variations in some dihedral angles. The Ramachandran angles of the observed C7-C7 gas phase structure of the Pro-Gly peptide listed in **Table 1** are at par with those for the C7 backbone reported in the literature.⁴⁸

4. Conclusions

Gas phase laser spectroscopic techniques such as R2PI, RIDIR, and IR-UV hole-burning spectroscopy along with quantum chemical calculations are used to explore the conformational landscape of Z-Gly-Pro-OH. The most stable conformer out of the two observed conformers is found to have an extended β -strand structure stabilized solely by a weak intraresidue C5 hydrogen bond. Another experimentally observed conformer in the gas phase was found to have a folded structure stabilized by O-H... π interaction.

Sequence-dependent folding motifs of Boc-Gly-^DPro-NHBn-OMe and Boc-^DPro-Gly-NHBn-OMe peptides are investigated using gas phase electronic and IR spectroscopy combined with quantum chemistry calculations, solution phase FTIR, and 2D-NMR spectroscopy and

X-ray crystallography. The gas-phase low-energy conformers of Boc-Gly-^DPro-NHBn-OMe exhibit extended β -strand or PP-II structures with C5 and C7 hydrogen-bonded rings, mirroring solution-phase and solid-state structures observed via FTIR, NMR, and XRD. For the Pro-Gly peptide, gas-phase conformers show C7-C7 (2_7 -ribbon) structures, while solution-phase NMR and FTIR indicate a C10 (β -turn) structure, likely influenced by solvent presence. This study highlights the transition from an extended β -strand in Gly-Pro to a β -turn in Pro-Gly and underscores the complementary insights gained from gas-phase, solution-phase, and solid-state analyses in understanding peptide folding motifs.

5. Acknowledgments

The authors express their gratitude to the Science and Engineering Research Board (SERB), India (Grant Nos. CRG/2020/002696, EMR/2015/000486, SR/S1/PC/0054/2010) for partially funding this research. They also gratefully acknowledge the financial support provided by IISER Pune. The computational resources and support from the 'PARAM Brahma Facility' under the National Supercomputing Mission, Government of India, at IISER Pune are deeply appreciated. The authors thank Prof. H. N. Gopi of IISER Pune for his valuable discussions on the results presented in this manuscript. The authors also acknowledge all the members of the group and collaborators who have contributed to this research. Additionally, they extend their thanks to Dr. Sayan Bagchi of the National Chemical Laboratory, Pune, for facilitating the measurement of solution-phase IR spectra using the FTIR spectrometer in his laboratory.

6. References

1. H. A. Scheraga, *Pure Appl. Chem.*, 1973, **36**, 1-8.
2. K. C. Chou, *Anal. Biochem.*, 2000, **286**, 1-16.
3. D. L. Nelson and M. M. Cox, *Lehninger Principles of Biochemistry*, W. H. Freeman and Company Ltd, New York, USA, Fifth edn., 2008.
4. E. Vass, M. Hollósi, F. Besson and R. Buchet, *Chem. Rev.*, 2003, **103**, 1917-1954.

5. J. M. Berg, J. L. Tymoczko and L. Stryer, *Biochemistry*, W. H. Freeman, New York, 5th edn., 2002.
6. L. Pauling, R. B. Corey and H. R. Branson, *Proc. Natl. Acad. Sci. U. S. A.*, 1951, **37**, 205-211.
7. G. D. Rose, L. M. Gierasch and J. A. Smith, in *Adv. Protein Chem.*, eds. C. B. Anfinsen, J. T. Edsall and F. M. Richards, Academic Press, 1985, vol. 37, pp. 1-109.
8. J. K. Myers and C. N. Pace, *Biophys. J.*, 1996, **71**, 2033-2039.
9. R. W. Newberry and R. T. Raines, *Nat. Chem. Biol.*, 2016, **12**, 1084.
10. R. A. Nyquist, *Spectrochim. Acta*, 1963, **19**, 509-519.
11. V. Yatsyna, R. Mallat, T. Gorn, M. Schmitt, R. Feifel, A. M. Rijs and V. Zhaunerchyk, *J. Phys. Chem. A*, 2019, **123**, 862-872.
12. P. N. Lewis, F. A. Momany and H. A. Scheraga, *Proc. Natl. Acad. Sci. U. S. A.*, 1971, **68**, 2293.
13. S. S. Zimmerman, L. L. Shipman and H. A. Scheraga, *J. Phys. Chem.*, 1977, **81**, 614-619.
14. E. R. Stimson, S. S. Zimmerman and H. A. Scheraga, *Macromolecules*, 1977, **10**, 1049-1060.
15. C. M. Venkatachalam, *Biopolymers*, 1968, **6**, 1425-1436.
16. S. K. Brahmachari and V. S. Ananthanarayanan, *Proc. Natl. Acad. Sci. U. S. A.*, 1979, **76**, 5119-5123.
17. H. E. Stanger and S. H. Gellman, *J. Am. Chem. Soc.*, 1998, **120**, 4236-4237.
18. S. Rao Raghothama, S. Kumar Awasthi and P. Balam, *J. Chem. Soc., Perkin Trans. 2*, 1998, 137-144.
19. R. Mahalakshmi, S. Raghothama and P. Balam, *J. Am. Chem. Soc.*, 2006, **128**, 1125-1138.
20. A. Ravi, B. V. V. Prasad and P. Balam, *J. Am. Chem. Soc.*, 1983, **105**, 105-109.
21. T. S. Haque, J. C. Little and S. H. Gellman, *J. Am. Chem. Soc.*, 1996, **118**, 6975-6985.
22. E. Gloaguen, M. Mons, K. Schwing and M. Gerhards, *Chem. Rev.*, 2020, **120**, 12490-12562.
23. E. Gloaguen and M. Mons, in *Gas-Phase IR Spectroscopy and Structure of Biological Molecules*, eds. A. M. Rijs and J. Oomens, Springer International Publishing, Cham, Switzerland, 2015, pp. 225-270.
24. P. S. Walsh, K. N. Blodgett, C. McBurney, S. H. Gellman and T. S. Zwier, *Angew. Chem. Int. Ed.*, 2016, **55**, 14618-14622.
25. W. Chin, I. Compagnon, J. P. Dognon, C. Canuel, F. Piuzzi, I. Dimicoli, G. von Helden, G. Meijer and M. Mons, *J. Am. Chem. Soc.*, 2005, **127**, 1388-1389.
26. W. Chin, J. P. Dognon, F. Piuzzi, B. Tardivel, I. Dimicoli and M. Mons, *J. Am. Chem. Soc.*, 2005, **127**, 707-712.
27. I. Karle, H. N. Gopi and P. Balam, *Proc. Natl. Acad. Sci. U. S. A.*, 2002, **99**, 5160-5164.
28. S. Aravinda, V. V. Harini, N. Shamala, C. Das and P. Balam, *Biochemistry*, 2004, **43**, 1832-1846.
29. I. L. Karle, S. K. Awasthi and P. Balam, *Proc. Natl. Acad. Sci. U. S. A.*, 1996, **93**, 8189.
30. I. L. Karle, C. Das and P. Balam, *Proc. Natl. Acad. Sci. U. S. A.*, 2000, **97**, 3034.
31. T. S. Haque and S. H. Gellman, *J. Am. Chem. Soc.*, 1997, **119**, 2303-2304.
32. I. Haym and M. A. Brimble, *Synlett*, 2009, 2315-2319.
33. S. Kumar, K. K. Mishra, S. K. Singh, K. Borish, S. Dey, B. Sarkar and A. Das, *J. Chem. Phys.*, 2019, **151**, 104309.
34. S. Kumar, K. Borish, S. Dey, J. Nagesh and A. Das, *Phys. Chem. Chem. Phys.*, 2022, **24**, 18408-18418.
35. S. Kumar, P. Biswas, I. Kaul and A. Das, *J. Phys. Chem. A*, 2011, **115**, 7461-7472.
36. S. K. Singh, S. More, S. Kumar, K. K. Mishra, K. N. Ganesh and A. Das, *Phys. Chem. Chem. Phys.*, 2019, **21**, 4755-4762.
37. S. K. Singh, P. R. Joshi, R. A. Shaw, J. G. Hill and A. Das, *Phys. Chem. Chem. Phys.*, 2018, **20**, 18361-18373.
38. S. Kumar, S. K. Singh, C. Calabrese, A. Maris, S. Melandri and A. Das, *Phys. Chem. Chem. Phys.*, 2014, **16**, 17163-17171.
39. F. Piuzzi, I. Dimicoli, M. Mons, B. Tardivel and Q. Zhao, *Chem. Phys. Lett.*, 2000, **320**, 282-288.
40. G. Meijer, M. S. de Vries, H. E. Hunziker and H. R. Wendt, *Appl. Phys. B*, 1990, **51**, 395-403.
41. A. Das, K. K. Mahata and T. Chakraborty, *J. Chem. Phys.*, 2001, **114**, 8310-8315.
42. S. L. Mayo, B. D. Olafson and W. A. Goddard, *J. Phys. Chem.*, 1990, **94**, 8897-8909.
43. G. Imre, G. Veress, A. Volford and Ö. Farkas, *J. Mol. Struct. Theochem*, 2003, **666-667**, 51-59.
44. M. J. Frisch, G. W. Trucks, H. B. Schlegel, G. E. Scuseria, M. A. Robb, J. R. Cheeseman, G. Scalmani, V. Barone, G. A. Petersson, H. Nakatsuji, X. Li, M. Caricato, A. V. Marenich, J. Bloino, B. G. Janesko, R. Gomperts, B. Mennucci, H. P. Hratchian, J. V. Ortiz, A. F. Izmaylov, J. L. Sonnenberg, Williams, F. Ding, F. Lipparini, F. Egidi, J. Goings, B. Peng, A. Petrone, T. Henderson, D. Ranasinghe, V. G. Zakrzewski, J. Gao, N. Rega, G. Zheng, W. Liang, M. Hada, M. Ehara, K. Toyota, R. Fukuda, J. Hasegawa, M. Ishida, T. Nakajima, Y. Honda, O. Kitao, H. Nakai, T. Vreven, K. Throssell, J. A. Montgomery Jr., J. E. Peralta, F. Ogliaro, M. J. Bearpark, J. J. Heyd, E. N. Brothers, K. N. Kudin, V. N. Staroverov, T. A. Keith, R. Kobayashi, J. Normand, K. Raghavachari, A. P. Rendell, J. C. Burant, S. S. Iyengar, J. Tomasi, M. Cossi, J. M. Millam, M. Klene, C. Adamo, R. Cammi, J. W. Ochterski, R. L. Martin, K. Morokuma, O. Farkas, J. B. Foresman and D. J. Fox, *Gaussian 09. Journal*, 2009.
45. H. Goto and E. Osawa, *J. Am. Chem. Soc.*, 1989, **111**, 8950-8951.
46. H. Goto and E. Osawa, *J. Chem. Soc., Perkin Trans. 2*, 1993, 187-198.
47. M. J. Frisch, G. W. Trucks, H. B. Schlegel, G. E. Scuseria, M. A. Robb, J. R. Cheeseman, G. Scalmani, V. Barone, G. A. Petersson, H. Nakatsuji, X. Li, M. Caricato, A. V. Marenich, J. Bloino, B. G. Janesko, R. Gomperts, B. Mennucci, H. P. Hratchian, J. V. Ortiz, A. F. Izmaylov, J. L. Sonnenberg, Williams, F. Ding, F. Lipparini, F. Egidi, J. Goings, B. Peng, A. Petrone, T. Henderson, D. Ranasinghe, V. G. Zakrzewski, J. Gao, N. Rega, G. Zheng, W. Liang, M. Hada, M. Ehara, K. Toyota, R. Fukuda, J. Hasegawa, M. Ishida, T. Nakajima, Y. Honda, O. Kitao, H. Nakai, T. Vreven, K. Throssell, J. A. Montgomery Jr., J. E. Peralta, F. Ogliaro, M. J. Bearpark, J. J. Heyd, E. N. Brothers, K. N. Kudin, V. N. Staroverov, T. A. Keith, R. Kobayashi, J. Normand, K. Raghavachari, A. P. Rendell, J. C. Burant, S. S. Iyengar, J. Tomasi, M. Cossi, J. M. Millam, M. Klene, C. Adamo, R. Cammi, J. W. Ochterski, R. L. Martin, K. Morokuma, O. Farkas, J. B. Foresman and D. J. Fox, *Gaussian 16 (Revision C.01)*, Gaussian, Inc. *Journal*, 2016.
48. L. L. Porter and G. D. Rose, *Proc. Natl. Acad. Sci. U. S. A.*, 2011, **108**, 109-113.

	<p>Alope Das received his B.Sc. (1994) and M.Sc. (1996) degrees from Jadavpur University, Kolkata, India. He earned his Ph.D. degree in the area of gas phase laser spectroscopy from Indian Institute of Technology Kanpur in 2002 under the supervision of Professor Tapas Chakraborty. Subsequently, he moved to Purdue University to do his postdoctoral research with Professor Timothy S. Zwier and worked on conformation-specific UV and IR spectroscopy of flexible aromatic hydrocarbons, which are isomeric products in fuel combustion processes (2002-2004). Later, he was a post-doctoral fellow with Professor Erwin D. Poliakoff at the Louisiana State University to study vibrationally resolved Vacuum-Ultraviolet (VUV) photoelectron spectroscopy of polyatomic molecules in the gas phase using synchrotron radiation at the Advanced Light Source of the Lawrence Berkeley National Laboratory (2004-2007). In 2007, he joined the Indian Institute of Science Education and Research (IISER) Pune as an Assistant Professor in the Department of Chemistry. Dr. Das is a Professor at the Indian Institute of Science Education and Research (IISER) Pune since 2019. His research includes a molecular-level understanding of various types of non-covalent interactions through gas-phase laser spectroscopy of isolated molecules and complexes relevant to biomolecules and materials using laser desorption as the vaporization source. Currently, a major focus of his research is on understanding $n \rightarrow \pi^*$ non-covalent interaction, Sulfur hydrogen-bonding, sequence-dependent folding motifs of peptides, etc.</p>
	<p>Dr. Satish Kumar got his Integrated MSc degree in chemistry from the National Institute of Science Education and Research, Bhubaneswar in 2015. He completed his Ph.D. in chemistry from the Indian Institute of Science Education and Research under the supervision of Prof. Alope Das. His work during his Ph.D. focused on the study of inherent conformation preferences of small capped peptides in the gas phase as well as the condensed phase. He is currently a post-doctorate fellow at the University of Utah, USA.</p>
	<p>Mr. Sourav Mandal is a Senior Research Fellow in the Department of Chemistry at the Indian Institute of Science Education and Research (IISER) Pune since August 2023. He joined IISER Pune as a Junior Research Fellow in August 2021. He received his B.Sc. in Chemistry from Vidyasagar University in 2018 and his M.Sc. in Chemistry from Calcutta University, Kolkata, in 2020. He is currently working under the supervision of Prof. Alope Das to investigate the folding motifs of peptides with varying sequences employing gas phase laser spectroscopy, NMR, and X-ray crystallography.</p>

Versatility of Carbon Dots as a Photosensitizer

Somen Mondal*^a

^a Institute of Chemical Technology, Mumbai, Marathwada Campus, Jalna, Maharashtra 431203, India

E-mail: s.mondal@marj.ictmumbai.edu.in

Abstract

Carbon dots (C-dots) are highly promising light-harvesting materials with great potential as photosensitizers, owing to their environmentally friendly nature, biocompatibility, and cost-effectiveness. Their versatility as photosensitizers has sparked significant interest, positioning them as a key material for future advancements. Furthermore, the flexibility of C-dots in charge transfer arises from their dual ability to act as both electron acceptors and electron donors. The charge transfer between photosensitizers (C-dots) and molecular quenchers is a fundamental process underlying various applications in photocatalysis, sensing, and optoelectronics. The processes of charge transfer between C-dots and quenchers are extensively studied using a range of techniques, including steady-state and time-resolved photoluminescence, ultrafast transient absorption, and fluorescence up-conversion. The extensive array of reported electron donor-acceptor systems highlight the versatility of C-dots as photosensitizer, with tuneable electronic properties designed to meet the challenges of emerging technologies.

1. Introduction

Carbon dots (C-dots), one of the most interesting 0-D allotropes of carbon, are first identified during the purification of single-walled carbon nanotubes (SWCNTs) using gel electrophoresis as by-products.^[1] Since its inception, C-dots have significant attention as versatile photosensitiser due to its high aqueous solubility, easy functionalization, high quantum yield, high photostability, low toxicity, and chemical inertness etc.^[2-10] A progressively increasing volume of research publications of C-dots are noticed in the field of optoelectronics, photocatalysis, energy storage, drug delivery, bioimaging and sensing as shown in the diagram (**Figure 1a,b**).^[2-10] However, the complete understanding of structure and optical properties of C-dots remains elusive due to their complex photophysical behaviour. Resulting from a decade of research, various scientific groups have established two perspectives on the heterogeneous behaviour of C-dots. The first overview and the most widely accepted explanation is that the C-dots contain

two distinct emissive species: blue emission arises from the core state, attributed to an sp²-hybridized aromatic network surrounded by an amorphous sp³-hybridized domain, while green and red emissions originate from the surface state, influenced by functional groups present at the edges of the carbon core.^[11-14] The second opinion is that the formation of molecular fluorophores or aggregated structures within the carbon core during the time of synthesis.^[15,16] The major drawback is the lack of proper purification of C-dots, which hinders the determination of their structure and optical properties. Therefore, it is recommended to use purified C-dots followed the following techniques such as high-performance liquid chromatography (HPLC), column chromatography, or gel electrophoresis for purifying C-dots, rather than relying on dialysis. Interestingly, the pure C-dots serve as excellent photosensitizers and exhibit outstanding properties as both electron donors and electron acceptors due to presence of core as well as surface in a single particles.^[12,13,17-21]

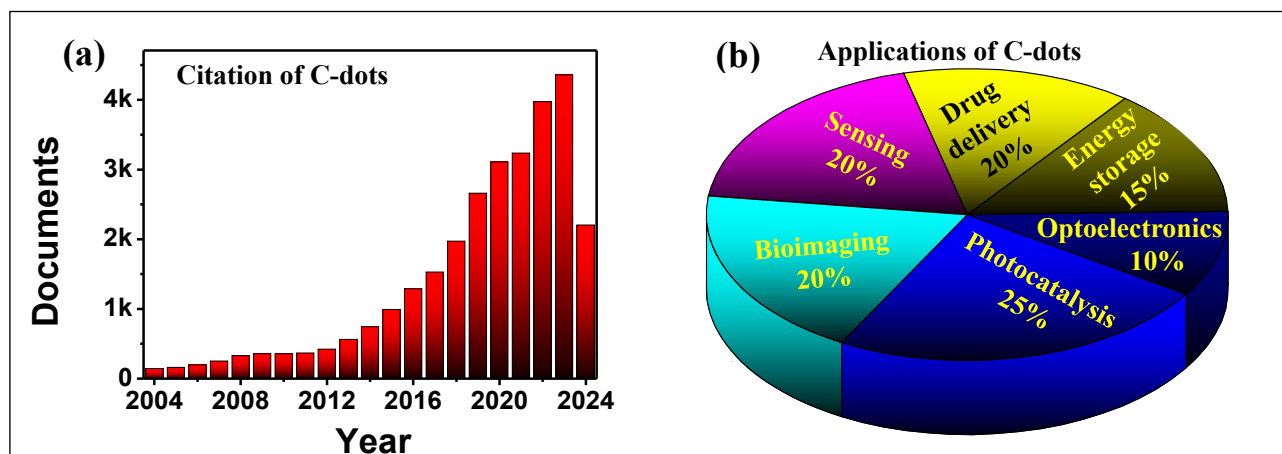


Figure 1: (a) The number of citations of C-dots since 2004; search results are obtained from the Scopus (b) Pie chart of applications perspective of C-dots (AI based statistics).

Photoinduced electron transfer (PET) is a fundamental process in photosensitizers and a critical chokepoint in advancing new optoelectronic devices, photocatalytic systems, and other light-activated applications. In PET process, the photosensitizer absorbs light, thereby creating a photoexcited electron-hole pair. After that, the photoexcited electron or hole transfer from photosensitizer to quencher depends on the suitable band alignment of quencher. The PET process in between C-dot and quencher (A for electron acceptor, D for hole acceptor) can be explained using the following steps and **Scheme 1**:

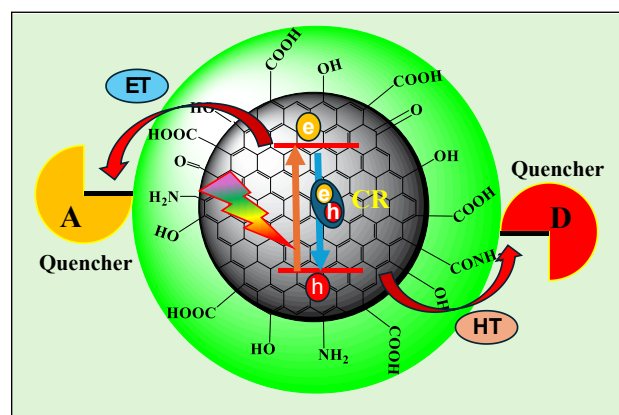
Step 1: Photoexcitation: $\text{C-dots} + \text{light} \rightarrow \text{C-dots}^* (e + h)$

Step 2: Charge transfer (CT): $\text{C-dots}^* (e + h) + \text{A} \rightarrow \text{C-dots} (h) + \text{A} (e)$

$\text{C-dots}^* (e + h) + \text{D} \rightarrow \text{C-dots} (e) + \text{D} (h)$

Step 3: Charge recombination (CR): $\text{C-dots}^* (e + h) \rightarrow \text{C-dots} + \text{PL}$

Various electron acceptors (EA), including 4-nitrotoluene,^[22] 2,2,6,6-tetramethylpiperidinoxyl (TEMPO),^[23] methyl viologen (MV^{2+}),^[20] metal nanoparticles,^[24] fumarate reductase, and [NiFeSe]-hydrogenase,^[2] have been utilized to



Scheme 1: PET process in C-dots based Donor (D) and Acceptor (A) system where C-dots act as a photosensitizer

investigate the electron-accepting properties of C-dots. Additionally, C-dots have been employed as electron donors (ED) in the presence of compounds such as N,N-diethylaniline (DMA),^[25] triethanolamine (TEOA),^[26] zinc porphyrins,^[27] and ethylenediaminetetraacetic acid (EDTA).^[28] In this review, we focus on the ability of C-dots to act as photosensitizers, using methyl viologen (MV^{2+}) as a molecular quencher, where it primarily functions as an electron acceptor. MV^{2+} was chosen due to its strong surface binding affinity and relatively mild reduction potential (-0.45 V vs. NHE in aqueous solution), which aligns well with the band structure of C-dots. Furthermore, the quenching process with MV^{2+} is straightforward to monitor because the resulting

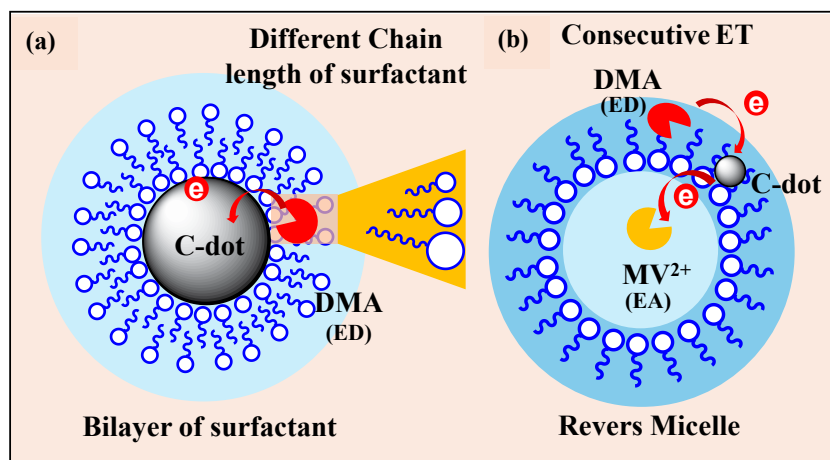


Figure 2: (a) Surfactant chain length controls PET process in cationic surfactant (CTAB, TTAB and DTAB) bilayer protected C-Dots (b) A consecutive ET process in encapsulated C-dots and DMA (ED, at nonpolar environment) and MV²⁺ (EA, at polar environment). Ref. 25, 29

MV²⁺ radical, which is relatively stable under anaerobic conditions, exhibits a distinct spectral signature with an absorbance peak at 605 nm. Here, we explore the PET process in confined environments, aggregated nanostructures and the role of doped C-dots via exploring the dynamics of ET process in different systems. Thus, our focus is on achieving a sustainable and efficient photosensitizer for various light-activated applications.

Effect of confined environment in PET process in C-Dots

A “confined environment” refers to a restricted space where physical and chemical properties differ significantly from those observed in bulk systems. Examples include nanopores, micelles, reverse micelles, liposomes, or polymer matrices, which offer well-defined microenvironments capable of influencing and controlling the PET process. The confined environments provide a restricted and trapped solvent molecules that often enhance ET efficiency by introducing proximity effects, reducing degrees of freedom, and strengthening interactions. Here, C-dots along with quencher are incorporated in the micelle via the formation of bilayer surrounding the C-dots and revers micelle to investigate the

photosensation capability of C-dots. First surfactant-protected core-shell C-Dots are developed by cationic surfactant (namely: Cetyltrimethylammonium bromide (CTAB), Dodecyltrimethylammonium bromide (DTAB), Tetradecyltrimethylammonium bromide (TTAB)) with different chain length and have successfully applied it in PET where we used DMA as an ED (Figure 2a). It is observed that the degree of PET enhances with increase the width of the shell where the solvent reorganization energy decreases with increase the surfactant chain

length due to higher compactness of the surfactant molecules. Furthermore, the behaviour of C-dots as efficient photosensitizer explores in the confined environment of reverse micelles where the ED, DMA, are incorporated in the nonpolar environment of the reverse micelles while the EA, MV²⁺, locates at the polar environment (Figure 2b). Resultant, the confined environment of reverse micelles provides two different phases for facilitating the consecutive ET process from DMA to MV²⁺ via C-dots.^[25,29] These finding will help in the areas of photocatalysis, light active chemical reaction where we can use C-Dot as photosensitiser in the confined environment.

Aggregation induced PET process in C-dots

An aggregated nanoscale assembly is formed when nanoscale materials come together to create larger structures through either covalent or non-covalent interactions. In this study, we developed a nanoparticulate array of C-dots to enhance PET using a host-guest approach. The surface of the C-dots was modified post-synthetically with boronic acid, which was further linked to α -cyclodextrin (α -CD) to create the aggregated nanoscale assembly. Three derivatives of methyl viologen were utilized to form this assembly: 1,1'-diheptyl-4,4'-bipyridinium dibromide

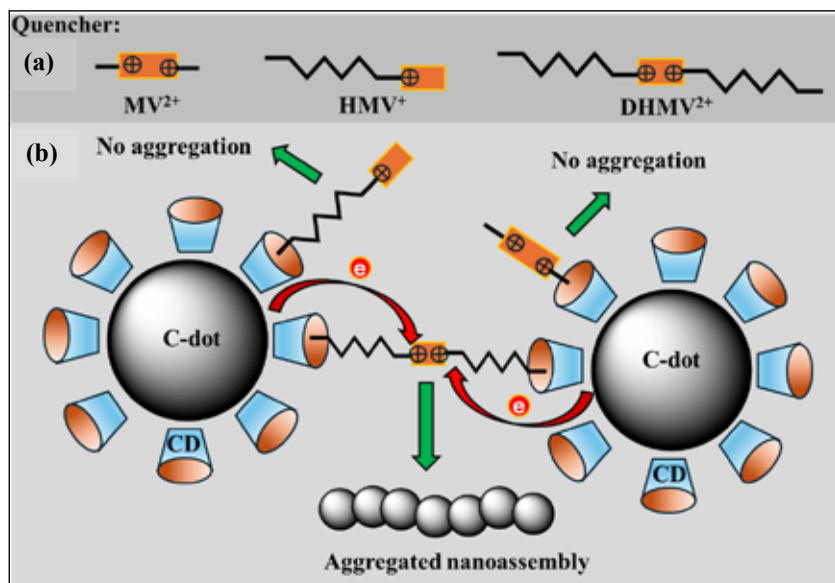


Figure 3: (a) Different derivatives of MV²⁺ used as a quencher to form the aggregated nano-assembly of α -CD-C-dots (b) pronounced PET is observed in the aggregated nano-assembly of α -CD-modified C-dots and the dual long hydrophobic chain-containing DHMV²⁺ quencher. However, a less efficient PET process is observed with HMV⁺ and MV²⁺ due to the lack of aggregation. Ref. 30

(DHMV²⁺), 1-heptyl-4-(4-pyridyl)pyridinium bromide (HMV⁺), and methyl viologen (MV²⁺) (Figure 3a). Among the three quenchers, DHMV²⁺ facilitated the formation of nanotubular aggregates due to strong hydrophobic interactions between its long hydrophobic tail and the hydrophobic cavity of α -CD. But no aggregation is observed for HMV⁺ and MV²⁺, as they contain either a single hydrophobic tail or none. Interestingly, a 1D aggregated nanoscale assembly of α -CD/C-dots and DHMV²⁺ is observed, facilitating long-range electron transfer (ET) through a molecular electronic junction spanning micrometres. As shown in Figure 3b, these derivatives enhanced the aggregation-induced PET process. Furthermore, the rate of ET is found to be 1.5 times faster in DHMV²⁺ than the other two viologen derivatives, HMV⁺ and MV²⁺. This enhancement is attributed to the formation of nanotubular aggregates, which promote electron hopping by lowering the activation energy.^[30] In summary, the self-assembly of aggregates in solution offers a fascinating strategy for modulating the photosensitizing capabilities of C-dots.

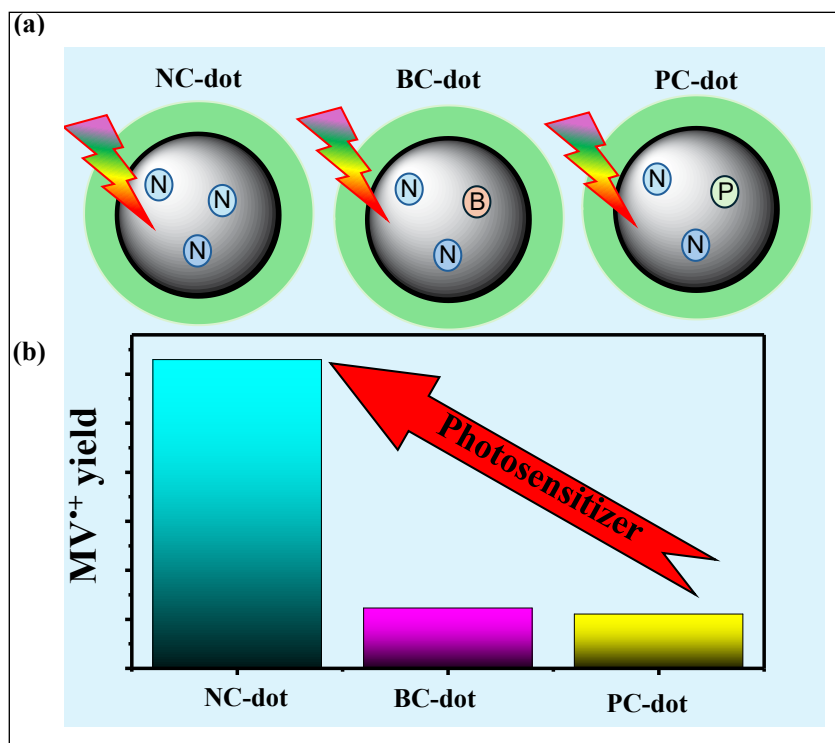


Figure 4: (a) Representation of nitrogen doped C-dots and boron, phosphorus doped NC-Dot (namely: BC-dots, PC-dots), (b) yield of MV⁺ radical generation after excitation with a 340 nm light source using different doped C-dots as a photosensitizer. Ref.20

Effect of doping in PET process in C-dots

Doping is one of the most effective ways to manipulate the electronic, optical, and chemical properties of nanoparticles, thereby influencing the efficiency and mechanism of PET. Notably, C-dots are often doped with

heteroatoms such as nitrogen, phosphorus, sulphur, and boron to control their optical properties and electron transfer capabilities. In this review, we focus on three doped C-dots, namely, BC-dots, PC-dots and NC-dots, where boron, phosphorus, are doped with N-doped C-Dots (NC-dots) to investigate the effect of doping in photosensitization capability of C-dots. The photosensitizing capabilities of various doped C-dots were evaluated through the photoreduction of MV^{2+} upon illumination with 340 nm light. Distinct absorption and transient absorption (TA) spectroscopy bands appeared at 605 nm, confirming the formation of MV^{\bullet} radicals. The photosensitizing performance of the different C-dots was assessed by calculating the quantum yield of MV^{2+} radical generation, as depicted in **Figure 4**. This quantum yield trend correlated well with the average charge recombination (CR) rates, where NC-dots exhibited slower CR rates compared to BC- and PC-dots.[20] These findings can aid in the design and development of highly efficient carbon-based photosensitizers, offering a promising alternative to commonly used heterogeneous catalysts.

2. Conclusions

In summary, C-dots offer a wide range of applications as photosensitizers due to their versatility in various microenvironments, the ability to incorporate heteroatom doping, and the formation of aggregated nanoscale assemblies. This review highlights the role of molecular electron donors and acceptors in enhancing charge transfer and charge separation within C-dot-quencher assemblies. Charge transfer is a critical factor for advancing photosensitization. Thus, the investigation and understanding of fundamental charge-transfer properties in different forms of C-dots are essential for optimizing their performance. Additionally, the encapsulation of C-dots within microenvironments, heteroatom doping, and the formation of aggregated nanoscale assemblies significantly influence the charge separation, charge recombination, and the generation of long-lived excited states. These factors

collectively enhance the efficiency of C-dots in photocatalysis, photo-sensing, photosensitization, and optoelectronic applications.

3. Acknowledgements

Dr. Somen Mondal thanks the Institute of Chemical Technology Mumbai, Marathwada Campus, India for providing the resources and facilities.

4. References

1. Y. Sun, B. Zhou, Y. Lin, W. Wang, K. A. S. Fernando, P. Pathak, M. J. Mezziani, B. A. Harruff, X. Wang, H. Wang, P. G. Luo, H. Yang, M. E. Kose, B. Chen, L. M. Veca, S. Xie, S. Carolina, *J. Am. Chem. Soc.* 128, (2006), 7756–7757.
2. G. A. M. Hutton, B. Reuillard, B. C. M. Martindale, C. A. Caputo, C. W. J. Lockwood, J. N. Butt, E. Reisner, *J. Am. Chem. Soc.* 138, (2016), 16722–16730.
3. F. Yan, Y. Jiang, X. Sun, Z. Bai, Y. Zhang, X. Zhou, *Microchimica Acta* 185, (2018), 420.
4. S. N. Baker, G. A. Baker, *Angew. Chem.* 49, (2010), 6726–6744
5. Y. Liu, H. Huang, W. Cao, B. Mao, Y. Liu, Z. Kang, *Mater. Chem. Front.*, 4, (2020), 1586–1613.
6. H. Li, Z. Kang, Y. Liu, S. T. Lee, *J. Mater. Chem.*, 22, (2012), 24230–24253.
7. J. Lui, R. Li, B. Yang, *ACS Cent. Sci.* 6, (2020), 2179–2195.
8. G. A. M. Hutton, B. C. M. Martindale, E. Reisner, *Chem. Soc. Rev.*, 46, (2017), 6111–6123.
9. A. Sciortino, A. Cannizzo, F. Messina, *C*, 4, (2018), 67.
10. S. Y. Lim, W. Shen, Z. Gao, *Chem. Soc. Rev.* 44, (2015), 362–381.
11. T. C. Wareing, P. Gentile, A. N. Phan, *ACS Nano*, 15, (2021), 15471–15501.
12. L. Wang, S. J. Zhu, H. Y. Wang, S. N. Qu, Y. L. Zhang, J. H. Zhang, Q. D. Chen, H. L. Xu, W. Han, B. Yang and H. B. Sun, *ACS Nano*, 8, (2014), 2541.
13. S. Deshmukh, A. Deore, S. Mondal, *ACS Appl. Nano Mater.*, 4, (2021) 7587–7606.
14. N. Ghorai, S. Bhunia, S. Burai, H. N. Ghosh, P. Purkayastha, S. Mondal, *Nanoscale*, 14, (2022), 15812–15820.
15. E. V. Kundelev, N. V. Tepliakov, M. Y. Leonov, V. G. Maslov, A. V. Baranov, A. V. Fedorov, I. D. Rukhlenko, A. L. Rogach, *J. Phys. Chem. Lett.*, 11, (2020), 8121–8127.
16. N. Soni, S. Singh, S. Sharma, G. Batra, K. Kaushik, C. Rao, N. C. Verma, B. Mondal, A. Yadav, C. K. Nandi, *Chem. Sci.*, 12, (2021), 3615–3626.
17. S. Mondal, M. Chatti, A. Mallick, P. Purkayastha, *Chem. Comm.*, 50, (2014), 6890–6893.
18. S. Burai, N. Ghorai, H. N. Ghosh, S. Mondal, *J. Phys. Chem. C*, 126, (2022), 20092–20100.
19. S. Bhunia, N. Ghorai, S. Burai, P. Purkayastha, H. N. Ghosh, S. Mondal, *J. Phys. Chem. C*, 125, (2021) 27252–27259.
20. S. Mondal, A. Yucknovsky, K. Akulov, N. Ghorai, T. Schwartz, H. N. Ghosh, N. Amdursky, *J. Am. Chem. Soc.*, 141, (2019), 15413–15422.
21. U. S. Sayyad, S. Waghmare, S. Mondal, *Nanoscale*, 16, (2024), 8143–8150.

22. X. Wang, L. Cao, F. Lu, M. J. Meziani, H. Li, G. Qi, B. Zhou, B. A. Harruff, F. Kermarrec, Y. P. Sun, *Chem. Comm.*, 25, (2009), 3774–3776.
23. F. Lin, D. Pei, W. He, Z. Huang, Y. Huang, X. Guo, *J. Mater. Chem.*, 22, (2012), 11801–11807.
24. H. Zhang, H. Huang, H. Ming, H. Li, L. Zhang, Y. Liu, Z. Kang, *J. Mater. Chem.*, 22, (2012), 10501–10506.
25. S. Mondal, T. Das, A. Maity, S. K. Seth, P. Purkayastha, *J. Phys. Chem. C*, 119, (2015), 13887–13892.
26. C. Dolle, J. T. Margraf, W. Bauer, T. J. Nacken, E. Spiecker, V. Strauss, W. Peukert, B. Butz, T. Clark, D. M. Guldi, J. Walter, *J. Am. Chem. Soc.*, 136, (2014), 17308–17316.
27. A. Cadranel, V. Strauss, J. T. Margraf, K. A. Winterfeld, C. Vogl, L. Dordević, F. Arcudi, H. Hoelzel, N. Jux, M. Prato, D. M. Guldi, *J. Am. Chem. Soc.*, 140, (2018), 904–907.
28. L. Cao, S. Sahu, P. Anilkumar, C. E. Bunker, J. Xu, K. A. S. Fernando, P. Wang, E. A. Gulians, K. N. Tackett, Y. P. Sun, *J. Am. Chem. Soc.*, 133, (2011), 4754–4757.
29. S. Mondal, T. Das, P. Ghosh, A. Maity, A. Mallick, P. Purkayastha, *Materials Letters*, 141, (2015), 252–254.
30. S. Mondal, P. Purkayastha, *J. Phys. Chem. C*, 120, (2016), 14365–14371.



Dr. Somen Mondal obtained his M.Sc. from NIT-Durgapur (2011), Ph.D. from IISER-Kolkata (Prof. Pradipta Purkayastha, 2017). He undertook postdoctoral research with Prof. H. N. Ghosh (INST-Mohali, India) and Prof. Nadav Amdursky (Technion-IIT-Israel) and working as an Assistant Professor in the Dept. of Chemistry at ICT-Mumbai, Marathwada Campus. His current research interest is to explore the photo-physics and carrier dynamics of carbon dot- and QD-based HS using ultrafast spectroscopy and also nanomaterial-doped biopolymers to control the conductivity of protein-based biomaterials for long-range electron and proton transport and applications toward the optoelectronic devices.

Design of Defect Engineered Intrinsic White Light Emitting Non-Rare-Earth Phosphors: State-of-the-art

A. K. Dehury^{1,2}, R. Kainda^{1,2}, S. Khato^{1,2}, R. C. Mallick^{1,2} and Y. S. Chaudhary^{1,2*}

¹Materials Chemistry and Interfacial Engineering Department, CSIR-Institute of Minerals and Materials Technology, Bhubaneswar-751 013, India

²Academy of Scientific and Innovative Research (AcSIR), Ghaziabad-201 002, India

*E-mail: yschaudhary@immt.res.in

Abstract

Defect-driven emission has gained significant attention as a versatile and efficient approach to achieve white light emission, a foundation for modern lighting and display technologies. This review provides a comprehensive overview of recent advancements on the design, synthesis, and application of defect-engineered phosphors for intrinsic white light generation. The role of intrinsic and extrinsic defects, such as vacancies, interstitials, and surface states, is explained, highlighting their ability to create intra-band localized energy states that facilitate broadband emission across the visible spectrum. These single-phase white light phosphors have been categorized into defect-engineered materials, including metal oxides, chalcogenides, quantum dots, composites, hybrid nanostructures, and charge transfer-based phosphors. The underlying emission mechanisms, tunability, and performance are discussed at length. State-of-the-art characterization techniques used to probe defect structures and their impact on photophysical properties are also elaborated. Furthermore, the article explores strategies for optimizing defect-induced emission through synthesis approaches, post-synthetic modifications, and environmental tailoring. These single intrinsic white emissive layer-based phosphor converted white LEDs (PC-W-LEDs) offer advantages such as enhanced color rendering index (CRI), correlated color temperature (CCT), and luminous efficacy (LE), as well as being cost-effective, easy to fabricate, and free from the blue tinge associated with conventional PC-W-LEDs that use multiple phosphors. Challenges such as non-radiative losses, stability, and reproducibility are critically assessed, alongside potential applications in white light-emitting diodes (W-LEDs) and displays. By integrating insights from defect physics, materials science, and device engineering, this review aims to provide a roadmap for leveraging defect-engineered materials to design next-generation self-activated white light emitters.

1. Introduction

Light sources have evolved from the early days of flame to modern electric lighting, such as incandescent lamps to fluorescent tubes to white light-emitting diodes (W-LEDs).^{1,2} With the advent of the inchoate semiconductor LED in the 1960s, a type of lighting lamp with a longer lifespan, safety, and environmental protection started to enter the field of vision of scientists. In 1993, Nakamura et al. discovered high-brightness blue LEDs, paving the way for the energy-efficient bright W-LEDs. These W-LEDs have become popular for lighting and display applications

owing to their energy efficiency.³ Nonetheless, these W-LEDs suffer from intensity dampening, low color-rendering index (CRI) (<75Ra), and a bluish tinge, leading to damage to retina cells in the human eye and involve sophisticated high vacuum-based synthesis protocol.⁴ Typically, the W-LEDs are fabricated by combining blue-LED chip- phosphors emitting green and red light, or ultraviolet (UV) or violet LED chip coupled with phosphors (RGB). However, the use of multiple phosphors leads to the degradation of phosphors over time due to different lifetimes, color reabsorption by different color components,

and the cost of phosphor and processes remain a matter of concern.^{1,4,8} To overcome these issues, the phosphors exhibiting broad emission spanning over the entire white light spectral region are being explored extensively in recent times, which can offer better color-balanced white light emission with a high CRI, high LE, enhanced color stability, facile fabrication process (devoid of multiple phosphor use), and devoid of a bluish tinge.^{1,4,8,9}

Further, the research thrust for W-LEDs has centered around achieving high LE, stable chromaticity, excellent color rendering properties, and competitive pricing compared to fluorescent lamps, which profoundly rely upon phosphor characteristics. A comprehensive understanding of the nature and phosphors structural chemistry, as well as the factors influencing the overall characteristics of W-LEDs are crucial for their advanced applications.

Defects that break the symmetry of the molecules can contribute to the emission phenomenon by creating different intermediate states between the conduction band (CB) and valence bands (VB). Some examples of such defects include oxygen vacancy, carbon-

based defects, sulfur vacancy, metal vacancy, interstitial defects, deep and shallow localized defects, and metal excess defects, **Figure 1**.^{10,11} As the annealing process can cause recovery of the structural defects and efficiently eliminate the non-radiative recombination centers, the defect-related photoluminescence (PL) strongly depends on the calcination temperature and time. Several methods such as wet chemical synthesis, pyrolysis, etching, annealing, etc., have been undertaken to cause defects that may be stoichiometric or non-stoichiometric. Moreover, each recombination luminescence includes the following processes: ionization, migration, recombination, and emission. This recombination process results in a longer lifetime (μs or ms). The defects generally have an impact on both lattice symmetry and energy levels of the phosphor, which generate a local potential in the defect site that could trap holes in the lattice of the crystalline solids. The hole-trapping phenomenon can easily be understood by considering a series of mid-gap states, including surface defect states or deep levels in the energy gap of the system that could be related to the broad emission phenomenon. The recombination of conduction band electrons with an oxygen vacancy or oxygen vacancy to a valence band can give rise to emission in the visible spectral region.¹⁰⁻¹³

The primary aim of this article is to provide the state-of-the-art to synthesize intrinsic white-light-emitting phosphors and their subsequent use to fabricate the W-LEDs, specifically focusing on (a) materials, methodologies being adopted including the underlying mechanisms; (b) strategies to tailor the excitation and emission spectra of phosphors; and (c) emerging insights to design single phase (component) white light-emitting phosphors to develop W-LEDs. The interplay between mechanisms, luminescent properties such as photoluminescence quantum efficiency (PLQE), CIE, external quantum efficiency (EQE), absorption efficiency (AE), etc., and device characteristics (CIE, CRI, CCT, LE) has also been elaborated. Further, emphasis is given

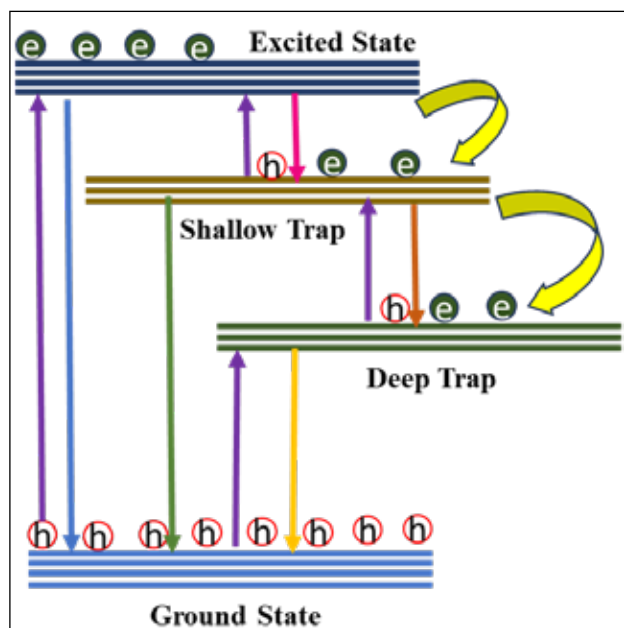


Figure 1 Simplified defect-based emission mechanism for single-phase white light emitting materials.

to the development of phosphors comprising abundant, non-rare-earth-based elements which eventually eliminates the issues of toxicity, scarcity, purification process, etc.

Defect-based Single-Phase White Light-Emitting Phosphors

Over the decade, numerous single-phase white light-emitting phosphors based on defect-activated emissions have been discovered. Still, many rely on rare earth materials that activate the white light emission in combination with the characteristic emission due to the f-f transition. Because of their optoelectronic and chemical characteristics, inorganic binary, ternary, and quaternary oxide phosphors have emerged as a viable option for developing direct white-light materials for solid-state lighting and luminescent device applications. Non-rare-earth binary oxide-ZnO based materials have been studied extensively for white light emission, and a variety of different synthesis conditions and doping methods to promote defects and defect-based emission have been attempted.

Defect Engineered Oxide Based Phosphors

For example, Shuai et al. synthesized broad white-emitting indium-doped ZnO nanoparticles using the sol-gel route that creates structural defects in the material, which shows new peaks at 465 nm, 535 nm, and 630 nm when doped with 10 atomic% indium.¹⁴ Similarly, Defects induced in Ga and In co-doped ZnO thin films by a solid-state route show white light emission, with CIE (0.31, 0.33) and a CCT of 6650 K. The emission covers the entire visible region which is generally a combination of green and red emissions originating from oxygen (V_o) and zinc (V_{zn}) vacancies and the violet-blue and blue emissions from zinc interstitial (Zn_i) and Zinc vacancy (V_{zn}), respectively, as confirmed by XPS analysis.¹⁵ ZnO nano petals exhibit enhanced broad defect emissions when synthesized at low temperatures. The multiple blue emissions are due to the zinc interstitial (Zn_i) that forms several sub-states related to the defect center at the surface of ZnO.

The green emission can be assigned to singly ionized oxygen vacancy (V_o^+) that recombines with a hole and red emission due to the deep zinc acceptor centers (V_{zn}). A core-shell paradigm is proposed to explain the defect-based emissions where negatively charged zinc vacancies (V_{zn}^-) (core) and positively charged oxygen vacancies (V_o^+) (shell) are controlled for red emission.¹⁶ Similarly, Lewis et al. synthesized broadband emitting ZnO due to defect-related emissions around 457 nm and 470 nm ascribed to transitions from Zn_i to V_{zn} , and at around 481 nm, 488 nm, and 492 nm attributed to the transition from the CB to V_o all transition observed in the violet-blue region by tuning the annealing temperature. By tuning the excitation wavelengths, the color temperatures of optimized samples could be tuned from warm (~4000 K) to cool (~8500 K). The fabricated PC-W-LED prototype exhibits white-light emissions with CIE coordinates (0.33, 0.33) and CRI ~95.¹⁷

While coupling doping with defects engineering in ZnO:Mn led to the broad photoluminescence spectra spanning over the entire visible spectral range. $Zn_{0.95}Mn_{0.05}O$ films show CIE values with (0.333,0.322), and a CCT of 5475 K.¹⁷ Trung et al. also explored the cationic doping effect of Al, which lead to warm white light emission from ZnO: Al exhibits emission in the visible region with CIE coordinate of (0.42,0.48), a PLQE of 43%, a CRI ~ 74, a CCT of 3873 K.¹⁸ Moreover, Das et al. reported highly reproducible, stable, phase-pure zinc oxide (ZnO) nanopowder synthesized by a simple, low-temperature aqueous solution-precipitation method showing white emission. The white light consisted of narrow blue and broad yellow-orange photoluminescence with CIE (0.36,0.33). The presence of Zn_i and O_i defects is responsible for such white and shows bi-exponential lifetime fitting corresponding to these two radiative processes with average lifetime (4-32 ms) and an PLQE (12-14%). These findings reveal that defect-related emissions are the primary contributors for white light emission in ZnO hosts or doped matrix. The synthesis conditions and doping

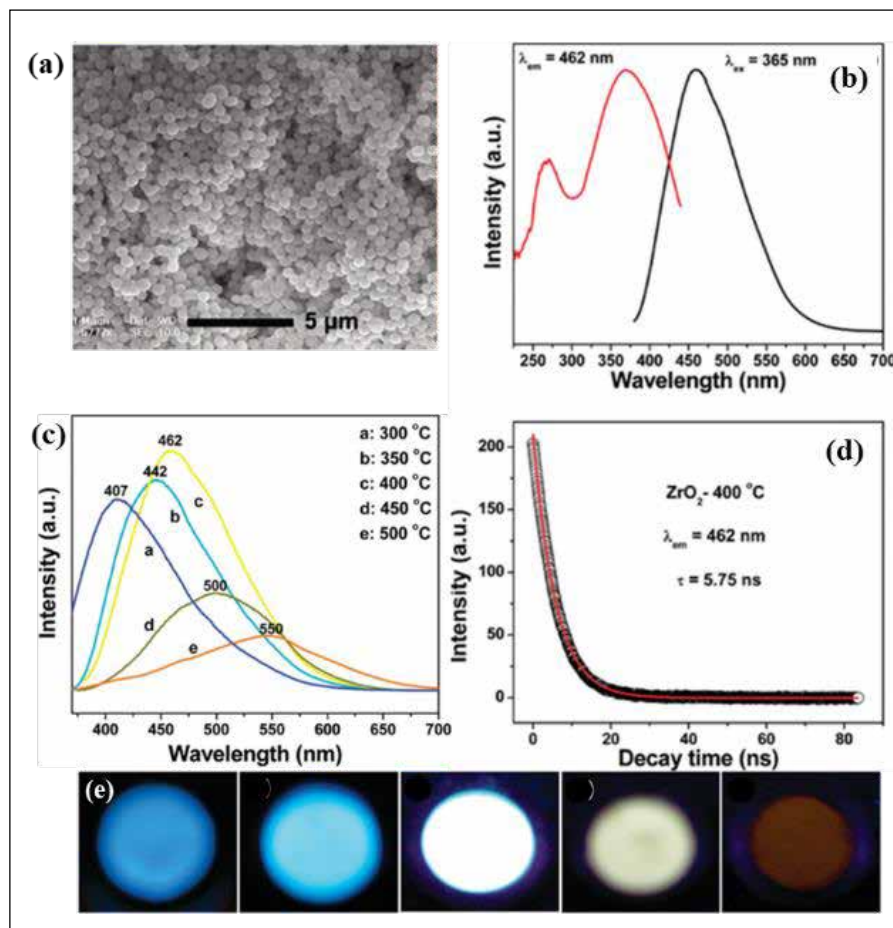


Figure 2 (a) SEM image of ZrO_2 sample, (b) Excitation and emission spectra, (c) Emission spectra of ZrO_2 samples annealed at different temperatures, (d) PL decay spectra for the ZrO_2 phosphor annealed at 400°C for 2h in air, (e) Luminescence photographs of for samples under the excitation of a 365 nm UV lamp (Reprinted with permission from Zhang et. al. Copyright {2009} American Chemical Society²⁰).

methods can be tailored to promote optimal defects and tune the emission properties of these phosphors.¹⁹

Similarly, binary oxide-based ZrO_2 was reported, which emits intense and broad emissions covering the visible spectral region. The emission can be tuned from blue to white and orange spectral regions by varying synthesis temperature owing to some chemical bond manipulation, carbon impurities and/or defects in the systems, **Figure 2**.²⁰ Besides binary oxides, some single-phase ternary oxides have also been reported that exhibit intrinsic white light emission owing to defects. Tavares research group investigated the photoluminescence of $CaIn_2O_4$

nanocrystals synthesized by the spray pyrolysis method, showing a broad emission spectrum upon excitation at 350.7 nm. These observed broad emissions are due to a typical multi-photon process defect generated during the synthesis process.²¹ The CIE coordinates for the $CaIn_2O_4$ nanocrystals were (0.312,0.382), revealing the white light emission from the phosphor.

Defect Engineered Chalcogenides Based Phosphors

Like metal oxide-based phosphors, chalcogenide (S, Se, Te) based intrinsic white light emitting phosphors based on S, Se, and Te are also being explored. Zinc sulfide (ZnS) is a highly versatile phosphor emitting blue, green, or orange light with long-lasting phosphorescence. Its applications are widespread,

including in cathode ray tube (CRT) screens. ZnS has been doped and/or synthesized at varying temperatures, and pressure, sintering conditions to achieve white light emission. In 2020, Saavedra et al. successfully co-doped ZnS nanoparticles with Co^{2+} and Mn^{2+} . This resulted in the generation of near-white light emission when excited with ultraviolet light. The emission color and intensity can be tailored by considering the interband energy transfer between Co^{2+} and Mn^{2+} ions and the creation of deep-level defect states in the host nanocrystals. The spectrum of the emission consists of multiple bands, corresponding to $V_s \rightarrow E_v$ (396–400 nm), $E_g \rightarrow V_{Zn}$ (444 nm), $E_g \rightarrow V_{Zn}^*$ (500 nm), $V_s^* \rightarrow V_{Zn}^g$ (570 nm), and $V_s^* \rightarrow V_{Zn}^*$ (630 nm) transitions of

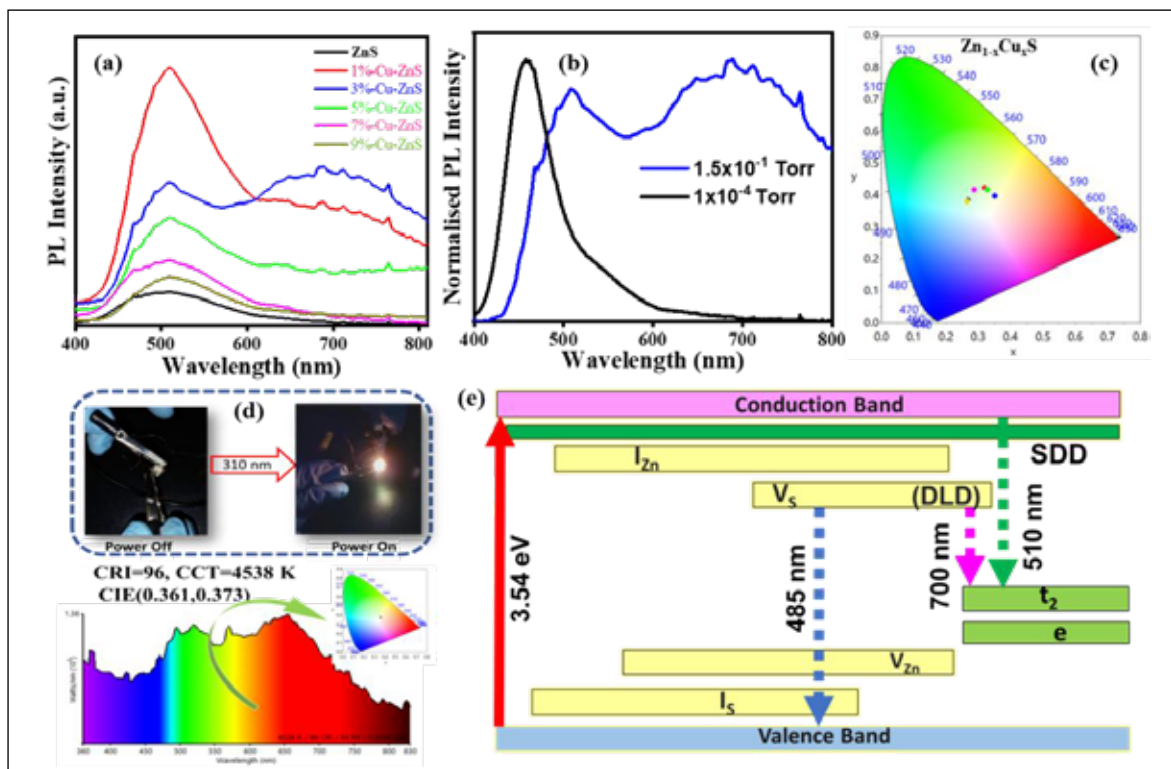


Figure 3 (a) Emission Spectra for different dopant concentration, (b) Emission spectra at different vacuum pressure, (c) CIE coordinate, (d) fabricated device at on and off condition, and emission spectra and CIE coordinates of fabricated W-LED prototype, (e) Mechanism of white light emission (Reprinted with permission from Dehury et. al, Copyright, {2022} Wiley-VCH GmbH²³).

the host intrinsic defect levels, as well as the ${}^4T_1 \rightarrow {}^6A_1$ transition of the Mn^{2+} ions (595 nm). At 1:1 Co^{2+}/Mn^{2+} ion ratio, CIE (0.30,0.32) with 3% PLQE and 4.52 ms lifetime was obtained.²² Our group reported Cu-doped ZnS with different dopant concentrations and varying vacuum pressure during the synthesis to instigate the red emission in the Cu-doped ZnS. We successfully optimized the reaction condition to achieve cool to warm and neutral white light emission. By optimizing the dopant concentration of Cu^{2+} and vacuum pressure intense red emission can be controlled along with the prevalent blue and green emission, which resulted in the intrinsic white light emission. The red emission manifested by introducing deep localized defect states mainly due to sulfur vacancies and activation of the t_2 energy level of Cu, which give rise to the recombination of electrons from the deep localized defect states to the t_2 energy level

of Cu. The fabricated W-LED prototype exhibits high CRI (97), CIE (0.361,0.373), and warm CCT (4538 K), **Figure 3**.²³

Recently, a green-bio-based ZnS nanoparticles have been synthesized by coprecipitation method showing white light emission, employing *Phyllanthus emblica* extract. The origin of white light is attributed to different defect states activated during the synthesis. The capped ZnS nanoparticles display cool white emission with CIE (0.305, 0.303) with a high CCT (7255 K) and excellent CRI (93).²⁴ Rosenthal's group reported another system based on CdSe nanocrystals with wide-band emission due to surface-state and band-edge emission.²⁵ The observed wide-band emissions are due to the recombination of charges from mid gap states created from the linkage of uncoordinated surface selenium sites. Further, the enhancement of the white light emission was achieved by

post-synthesis treatments along with improved quantum yield of up to 45% owing to a partial ligand exchange or surface trap.²⁵

Nanoparticle size plays a crucial role in the emission behavior owing to the quantum confinement phenomenon. Quantum dots (QDs) are generally well known for their single intense emission. Whereas, broad emission can be achieved by modifying the surface with suitable ligands and causing a defect in the core that will produce defect-originated emissions, which intrinsically balances to provide white light emission. Sapra et. al, has achieved white light emitting trap-rich CdS QDs with a 17% PLQE.²⁶ Alloying the QDs with other elements shows white emission in $Zn_{0.93}Cd_{0.07}Se$ QDs with PLQE of 12%.²⁶ However, the intrinsic high toxicity of Cd restricts its long-term practical applications. Additionally, Mn-doped zinc chalcogenide QDs demonstrated to exhibit white emission with the interaction of Mn^{2+} (${}^4T_1-{}^6A_1$) transition emission (yellow/orange light) and surface trap-states emission (blue/green light).²⁷ Mn-doped QDs are devoid of toxicity unlike Cd based but surface defect-based white light emissions from QDs, which are extremely sensitive synthesis condition and thus are thought-provoking to control and reproduce. To resolve the problem of toxicity and stability the route of co-doped QDs to achieve white light have been proposed. Different groups developed a method to produce Mn and Cu co-doped ZnSe QDs (Cu-Mn-ZnSe QDs) via a versatile synthesis approach. As a result, the QDs show white light emission. The blue emission (400 nm) observed is due to the band-edge transition, the green emission (480 nm) is attributed to the presence of Cu dopant, and the orange emission (580 nm) is associated with Mn dopant. Consequently, co-doping produces white light emission from QDs, and the intensities of each color emission can be controlled by adjusting the amount of dopant concentration in the QDs.²⁸ Panda et al. synthesized the same quantum dots by hot injection route, showing bright white light emission with PLQE of 17%. This demonstrates

the robustness and potential for extension to other host materials. It enables co-doping with various dopants to produce high-quality white light emitting phosphors that can potentially cover a wide range of the visible region for future lighting and display applications.²⁹

Defect Engineered Nitride Based Phosphors

Nitrides such as undoped GaN nanoparticles (NPs) having inherent vacancies (V_{Ga} and $V_{N'}$) which act as luminescence centers, have been centre stage for developing W-LEDs, exhibiting tunable broad emission properties covering RGB colors. Nonetheless, GaN is well known for its extensive use as a blue and UV-emitting LED application, whereas broad white emission is quite rare. Vacancies generate defect energy levels among the band edges and relate to their respective luminescence bands.^{24,25,30-32} Recently, GaN NPs by carbothermal reduction and nitridation process has been synthesized.³¹ Upon excitation with 325 nm using a He-Cd laser, GaN NPs emit a broadband covering the entire visible and UV region. The CIE coordinates of the GaN phosphors are closer to the standard white light (0.33, 0.33). White light emissions observed is due to the generation of defect levels between the band edges upon varying experimental conditions.

Defect Engineered Hybrid Inorganic-Organic Phosphors

The inorganic-organic hybrid phosphors are also being explored that can exhibit white light emission. In a study by Layek et al., white light was obtained from a ZnO-based nanoconjugate where ZnO nanocrystals (NCs) were coupled with organic dye solutions of ATTO 590 and ATTO 565, **Figure 4(a-c)**. This resulted in a tunable PLQE of 15-20% by manipulating the defect states. The hybrid organic-inorganic fluorophore nanophosphor shows white light emission due to the electronic coupling between ZnO NCs and the organic dye through FRET. This facilitated by the spectral overlap between the defect-induced emission of ZnO NCs and S_0

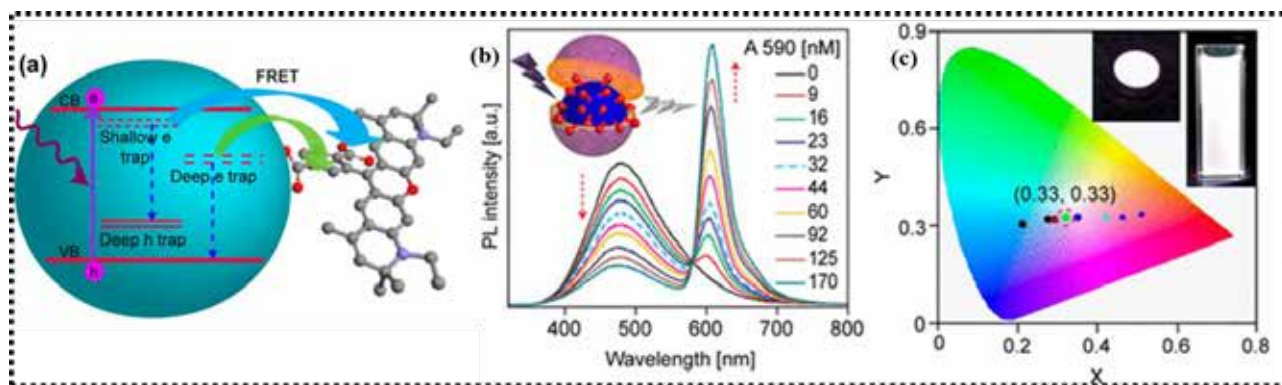


Figure 4 (a) Schematic of ATTO 590-conjugated ZnO NCs. (b) PL spectra. (c) CIE-1931 diagram (Insets: Colloidal suspension of white light-emitting ZnO-ATTO 565 nanoconjugates and a W-LED prototype) (Reprinted from Layek et al, Copyright {2023} American Chemical Society³².)

to S_1 absorption of conjugated dye system. The ability to modify blue ZnO emission by NC size and the orange-red emission of dye allows tuning of the white light emission characteristics. This hybrid phosphor shows an average lifetime of 45 to 34 ns with CIE coordinates of (0.33, 0.33), CCT (~5100-5300 K) and CRI values up to 95.³² In a similar study by Das et al., ZnO and DNA complex emitting white-light emission with CIE coordinates (0.33, 0.35) was achieved. The defect-related emissions generally occur near the blue-green, yellow, and orange-red corresponding to corresponding to singly ionized oxygen vacancies (V_O^+), doubly ionized oxygen vacancies (V_O^{2+}), interstitial oxygen (O_i), respectively. They showed that the DNA molecule suppresses the defect emission.³³ Nonetheless, Chen and co-workers fabricated direct white light-emitting organic ligand (trioctylphosphine oxide & stearic acid) capped ZnSe NCs. The white light emission due to mixing of blue emission of ZnSe NCs with green-red emission of radiative deep defect levels from ZnSe surface. The Fabricated W-LED prototype shows white light with CIE coordinates of (0.38, 0.41).³⁴ M. A. Schreuder et al. demonstrated direct white light emission using ultrasmall white-light CdSe NCs coated with biphenylperfluorocyclobutyl polymer with a 10% quantum efficiency, CIE coordinates of (0.333, 0.333) and a high CRI 93.³⁵ Likewise, Nizamoglu et al. and Shea-Rohwer et al. investigated broad and

white light emission from CdS NCs by modifying surface states and ligand displacement.³⁶⁻³⁷ Feng Li et al. recently reported single-phase CdS NCs that emitted intense white light due to surface defect 550 nm and exciton-based blue emissions. This exhibited a CRI value of 79.5 and a cold CCT value of 6238 K.³⁸

Defect Engineered Composite Phosphors

Core-shell systems are more effective in charge transfer by dipole interaction. In some cases, the core emission overlaps with shell emission to produce white light emission. For instance, Kar et al. synthesized a system based on an Mn: ZnS nanorod core and ZnO shell that shows white light emission. The emission peaks ~400 and 459 nm blue bands were attributed to sulfur-based vacancies and surface defect states in the phosphor whereas the green band at ~511 nm was attributed to singly ionized oxygen vacancy of the ZnO shell and the orange emission corresponds to ${}^4T_1 - {}^6A_1$ transition of the Mn^{2+} ions. Thus, the Mn-doped ZnS core emissions and the outer ZnO shell combine to produce white light with CIE (0.34, 0.38).³⁹ Furthermore, Ren et al. demonstrated a warm W-LED prototype with p-ZnO:Sb/n-GaN (NWs/film) heterojunction structure with the CIE (0.418, 0.429). Sb-doping activates deep and shallow acceptor levels, and electron-hole recombination between the CB of GaN and deeply trapped oxygen vacancy

center give rise to green emission. Whereas, yellow-orange emissions assigned to the CB of GaN to interfacial oxygen due to Li doping in ZnO. The weak blue emission is attributed to the emission from n type GaN to p-type ZnO:Sb. The contribution from all these states generates the white light emission.⁴⁰

Similarly, Poly (9,9-di-n-hexyl fluorenyl-2,7-dial) (PF) is used to encapsulate ZnO and Mn-doped ZnS results core-shell nanocomposites. The phosphor produces visible luminescence with tunable CCT ranging from warm to pure white light, with a PLQE of up to 91%. The blue and yellow emissions are attributed to $\pi^* \rightarrow \pi$ transition of PF, ${}^4T_1 \rightarrow {}^6A_1$ transition of Mn-doped ZnS nanoparticles and the interface-states transition respectively. The spectra and CCT can be tuned by tuning the ZMS(PF)ZnO ratio.⁴¹ Similarly, Luong et al. reported a core-shell structure based on ZnSe/ZnS: Mn core/(doped) shell and ZnSe/ZnS: Mn/ZnS core/(doped) shell/shell heterojunction NCs that emit white light due to bandgap based blue emission of ZnSe core and ${}^4T_1 \rightarrow {}^6A_1$ transition based yellow/orange emission from the of Mn^{2+} ions doped in ZnS. The green emission is attributed to surface defects which affects PLQE of core/(doped) shell and core/(doped) shell/shell NCs. The emission from the Mn: ZnS can be tuned from 580-600 nm by regulating the feeding molar ratio of [Zn]/[Mn]. By optimizing the dopant concentration, the phosphor shows white light with a quantum yield of about 27.6% and 20.5%, for ZnSe/ZnS:

Mn and ZnSe/ZnS: Mn/ZnS NCs respectively.⁴² Kim and coworkers synthesized CuGaS/ZnS QDs with varying Cu/Ga ratios and studied the critical roles of Cu deficiency in controlling their absorption and PL properties. They observed white light emission at a nominal ratio of Cu/Ga = 1/8 with high PLQE. The white emission combines the effect of exciton and defect-based emission, and the highest PLQE up to 76% was also achievable by further adjusting the ZnS-shelling period of Cu/Ga = 1.8 based QDs.⁴³ In a study by Roy et al., a highly luminescent and stable composite was developed by forming a blue-emitting Zn(N-methylsalicylaldimine)₂ complex on the surface of a yellow-emitting ZnO QDs. This resulted phosphor emits in the entire white light region with a CIE of (0.31,0.38) and (0.31,0.36), CRI of 74 and 82, and CCT of 6505 and 6517 K in solution and solid phases, respectively. The study also showed that the degree of complexation can be controlled to adjust the chromaticity and CCT, **Figure 5(a-c)**.⁴⁴

Similarly, Zhang and his team synthesized white emissive Cu, Mn: Zn-In-S/ZnS QDs exhibit excellent color properties with CIE (0.305,0.290), a CRI of 85, and a CCT of 7488 K.⁴⁵ Li et al. successfully optimized ZnS: Mn²⁺/ZnS/ZnS: Cu²⁺/ ZnS QDs by adjusting the ratios of the precursor injection temperature of an extra sulfur source. The QDs exhibit a blue emission peak at 450 nm from Cu²⁺ dopants, alongside 405 and 430 nm emission peaks corresponding to a defect emission center. Additionally, orange light

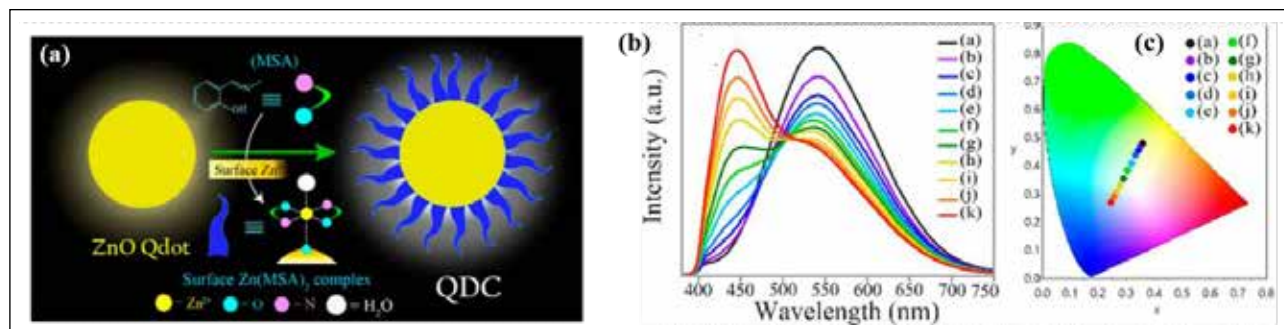


Figure 5 (a) Schematic Illustration of the Fabrication of White Light-Emitting Quantum Dot Complex (QDC) Nanocomposite, (b) Emission spectra, (c) chromaticity color coordinates in CIE diagram (Reprinted with permission from Roy et al, Copyright {2017} American Chemical Society⁴³).

is generated at 585 nm from Mn^{2+} dopants. The combination of blue and orange light produces white light emission with 38% PLQE. A white light device prototype fabricated emits warm white light with a CIE color coordinate of (0.32, 0.34) upon excitation by a commercial 370 nm UV LED chip.⁴⁶

Charge Transfer Based White Light Emitting Phosphors

Self-activated charge transfer-based emission can be observed in inorganic, organic, and hybrid phosphors. Some of the inorganic phosphors include vanadate, tungstate, cerate, gallates, and molybdates, which are reported to exhibit broad emission bands in the range of 400 to 700 nm or beyond due to charge transfer in the $[\text{MO}_x]^{n-}$ system where 'x' is the number of oxygens involved in the charge transfer moiety, and 'n' is the charge of the metal oxide cluster. The charge transfer may be Metal to ligand (MLCT) or ligand to Metal (LMCT) type consisting of different hybrid energy states with varying gaps of energy corresponding to different wavelengths (Blue, green, red, etc.) that are internally balanced to originate white light emission. The elemental energy bands are hybridized after the molecule formation to give some hybrid bands where the energy absorption and photon emission happen. Sometimes, the charge transfer spectra are not active; some distortion is required in the lattice to make them active. This kind of emission is also seen in the case of NCs and QDs, where the surface ligand to core metal established an LMCT system. C.R. Garcia and his group have reported a charge transfer system based on spinel-structured zinc gallate ternary oxide- ZnGa_2O_4 that shows excellent broad emission. The white light emission in ZnGa_2O_4 originate owing to the self-activation of the octahedral GaO_6 moiety. They prepared crystalline ZnGa_2O_4 phosphors with two different kinds of precursors such as Gallium acetylacetonate and Gallium nitrate, whereas former precursor shows the presence of oxygen vacancies with intense blue-green-yellow emission. GaO_6 exhibits blue emission, whereas

oxygen defects exhibit green-yellow emission with a prolonged lifetime of 212 s. The white light-emitting phosphor shows CIE (0.281, 0.373), which is in the vicinity of the CIE coordinate for ideal white light sources.⁴⁷

Similarly, SMM Zawawi et al. reported three different phases of tungstate, scheelite (BaWO_4), wolframite (NiWO_4), and perovskite layer (Bi_2WO_6) prepared using the sucrose-templated method. Broad emissions with a considerable blue shift were observed from emission spectra due to the quantum confinement effect results wider band gap. White emission is attributed to the $^1\text{T}_2$ excited state, and $^1\text{A}_1$ ground state electron-hole recombination of $[\text{WO}_4]^{2-}$ charge transfer species and defects due to oxygen vacancy levels are responsible for the white light emission.⁴⁸

Researchers have rigorously studied other charge transfer system based on vanadium-based materials showing broad-emission spectra.⁴⁹⁻⁵³ T. Nakajima et al. reported near white from the Charge transfer (CT) transition in the VO_4 tetrahedra in metavanadates AVO_3 (A: K, Rb, and Cs). The phosphors show CT transitions from VO_4 tetrahedra, i.e., $^3\text{T}_1$ - $^1\text{A}_1$ and $^3\text{T}_2$ - $^1\text{A}_1$ transitions with two distinct emission peaks. KVO_3 shows CIE (0.362, 0.453), CCT 4859K, and CRI of 73 with a low internal quantum efficiency (IQE) of 4%. Whereas the PLQE are reported to increase up to 79 and 83% for RbVO_3 and CsVO_3 due to increase in metal ion size with CIE (0.316, 0.424), (0.306, 0.418), CCT 5993K, 6334 K and CRI of 70 and 60 respectively. RbVO_3/PET shows luminous efficacy of f 15-48 mW cm^{-2} which is quite good for this phosphor.⁴⁹ They also studied another class of vanadate phosphor $\text{M}_3\text{V}_2\text{O}_8$ (M = Mg and Zn), exhibiting broadband emission from 400 to 700 nm, showing bluish-green to yellow emission with a high IQE.⁴⁹ The $\text{M}_3\text{V}_2\text{O}_8$ (M: Mg and Zn) also exhibits broadband (410-900 nm), yellow emission due to difference in the structural distortion of the VO_4 tetrahedra between the AVO_3 and $\text{M}_3\text{V}_2\text{O}_8$ which produces a large difference in energy levels arrangement in

ground and excited states. The $\text{Zn}_3\text{V}_2\text{O}_8$ showed high IQE (52%) compared to the $\text{Mg}_3\text{V}_2\text{O}_8$ (6%). They also studied the same systems based on the alkaline earth metals $\text{Ca}_3\text{V}_2\text{O}_8$ (CIE:0.328,0.407), $\text{Sr}_3\text{V}_2\text{O}_8$ (CIE:0.329,0.415), and $\text{Ca}_3\text{V}_2\text{O}_8$ (CIE: 0.303,0.591). The IQE values of M328 (M: Ba, Sr, Ca, Mg, and Zn) were 0.5, 3.7, 0.7, 6, and 52%, respectively. The emission spectral nature is also depending on the nature and size of the cation used which CIE and IQE.⁴⁹⁻⁵¹

The same group studied the other class of vanadate where the η values of $\text{M}_2\text{V}_2\text{O}_7$ (M: Ba, Sr, Ca) are 25, 8, and 0.4%, respectively, synthesized by a solid-state route. The phosphors observed emission of green (0.277, 0.389), yellow-green (0.393, 0.488), and yellowish-orange CIE (0.494, 0.439) for $\text{Ba}_2\text{V}_2\text{O}_7$, $\text{Sr}_2\text{V}_2\text{O}_7$ and $\text{Ca}_2\text{V}_2\text{O}_7$, respectively.⁵² Aditya Sharma et al. synthesized broad-band emitting pyro-vanadate $\text{Ca}_2\text{V}_2\text{O}_7$, $\text{Sr}_2\text{V}_2\text{O}_7$, and $\text{Ba}_2\text{V}_2\text{O}_7$ by a modified chemical precipitation method.⁵¹ They also observed broadband emission spectra from 400 to 700 nm exhibits a red shift varying with the ionic-radii of alkali-earth metal ions. The phosphors exhibit Yellow-orange (0.5308,0.4151), green-blue (0.2445,0.3357), and blue indigo (0.2053,0.2666) emission from $\text{Ca}_2\text{V}_2\text{O}_7$, $\text{Sr}_2\text{V}_2\text{O}_7$, and $\text{Ba}_2\text{V}_2\text{O}_7$ phosphors, respectively. Such tuning of color coordinates result in advancements in PL properties, depends on the synthesis procedure where the electronic state changes with different route of synthesis.⁵¹

Similarly, Pavitra et al. doped Rb to CsVO_3 that led more distorted VO_4^{3-} , which allows spin-forbidden transitions for CsVO_3 :Rb phosphors, resulting in enhanced IQE and EQE of 94.7% and 84.5% with superior emission than CsVO_3 host. The fabricated W-LED prototype exhibits white emission CIE (0.346,0.443), a good CRI of 69.7–81.5, and high LE of 94.8–58.7 lmW^{-1} .⁵² Likewise, M. M. Teixeira et al. developed a new stoichiometric $\text{Ca}_{10}\text{V}_6\text{O}_{25}$ vanadate phosphor capable of white-light emission on ultraviolet excitation using co-precipitation and microwave-assisted hydrothermal methods by varying temperatures. The changes in emission

characteristics of the phosphor material depend on the structural and morphology properties, which in turn depend upon the synthesis procedure. In addition, the effect of temperature on emission properties also exhibits a decrease in intensity as temperature increases at low activation energy values. The calculated CIE chromaticity coordinates are positioned entirely in the white region (0.311,0.348) and (0.350,0.368) in two different route syntheses.⁵³ They also studied a new system based on strontium vanadate ($\text{Sr}_{10}\text{V}_6\text{O}_{25}$) synthesized in a microwave-assisted hydrothermal process, which allowed to tune the structure and morphology of the phosphor. The phosphors obtained here show CIE in the range $x = 0.28-0.35$ and $y = 0.30-0.37$, which is nearer to the white light region.⁵⁴ Bharat et al. synthesized $\text{Ca}_2\text{KZn}_2(\text{VO}_4)_3$ phosphors using a citrate-assisted sol-gel method at low calcination temperatures. The W-LED prototype fabricated showed a yellowish-green emission CRI value of 84.3 and CCT of 5349 K. The vanadate phosphors are highly thermally stable rare-earth free phosphors where some modification may lead to white light emission.⁵⁵

We recently reported defect-engineered self-activated $\text{Ba}_3\text{V}_2\text{O}_8$ nanophosphor showing white light emission in 400-750 nm region by a one-pot microwave approach, to tune the molecular level distortion and to create oxygen vacancies that enables intrinsic white light emission with CIE (0.31,0.38,) high PLQE of 35%. The short- and long-range defects, in particular the oxygen vacancies, which eventually form an intermediate energy level in the forbidden region between the VB and CB are the primary contributors for red emission along with the host blue-green emission. fabricated W-LED prototype exhibits white-light-emission with CIE (0.353,0.392), CCT (~4867 K), CRI (~85), and high LE (~102 lm/W), **Figure 6**⁵⁶.

We also have developed new stoichiometric single-phase $\text{Ba}_3\text{V}_4\text{O}_{13}$, in the same procedure as mentioned above. The optimized phosphor exhibits white light emission which is a combination of host-based charge transfer as explained before and oxygen vacancy base

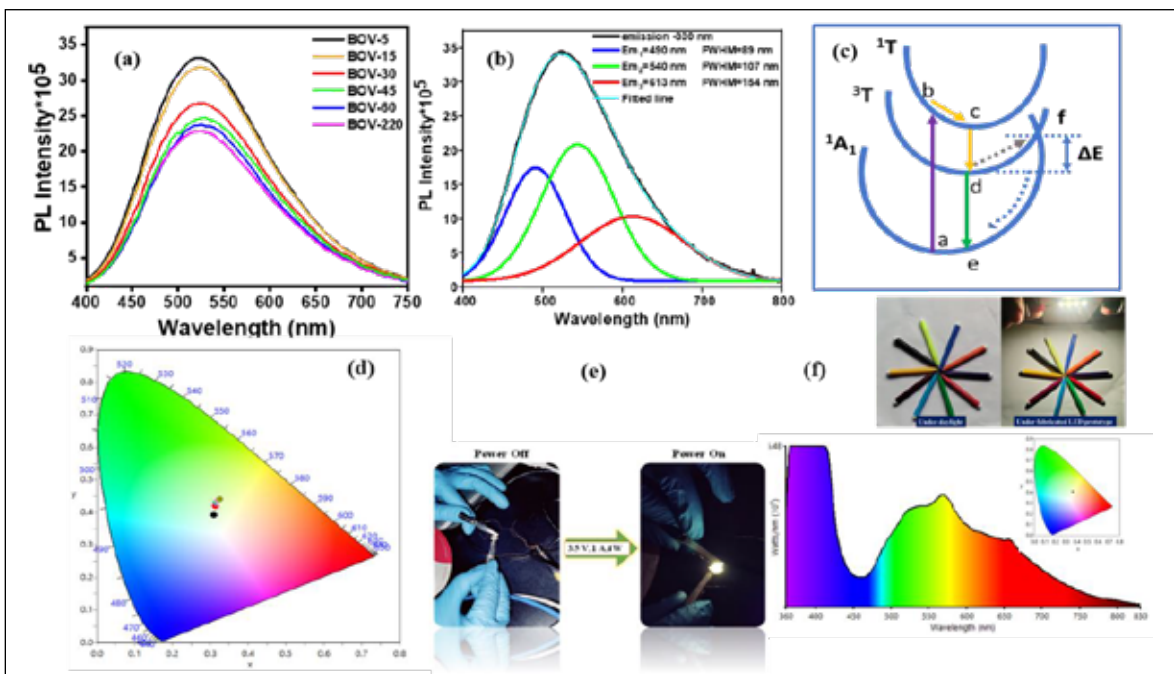


Figure 6 (a) Emission spectra for reaction condition, (b) Deconvoluted PL emission, (c) plausible mechanism for emission, (d) CIE plot, (e) Fabricated prototypes and emission spectra pictures under the fabricated LED and corresponding CIE plot, (f) Objects in daylight and under the fabricated W-LED (Reprinted with permission from Dehury et al, Copyright {2023} American Chemical Society.⁵⁶)

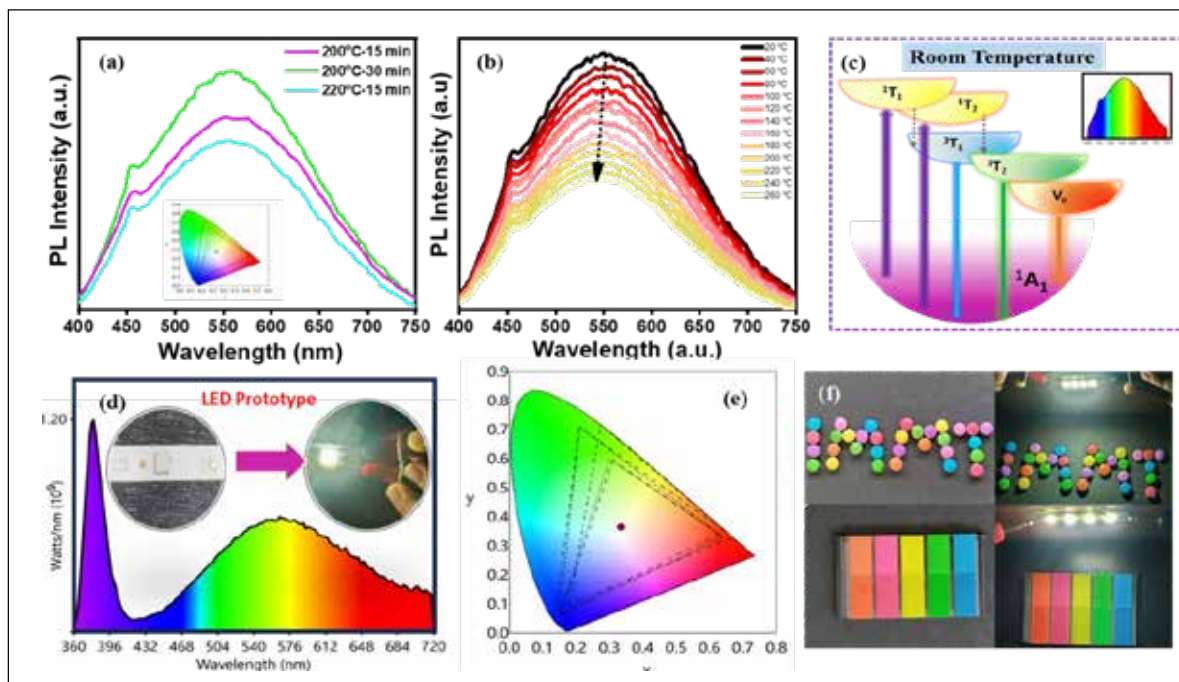


Figure 7 (a) Emission spectra for different reaction conditions, (b) temperature dependent emission spectra showing stability, (c) plausible mechanism for emission, (d) Fabricated prototypes and emission spectra pictures under the fabricated LED, (e) corresponding CIE plot, (f) Objects under the fabricated LEDs (Reprinted with permission from Dehury et al, Copyright, {2024} Royal Society of Chemistry.⁵⁷)

emission with CIE (0.333, 0.368) and 23.3% IQE and is stable up to 250°C. The fabricated W-LED prototype exhibiting a high CRI (~86.1), CCT (~5998 K), and high LE (~128.4 lm/W), **Figure 7**⁵⁷.

2. Conclusion

Defect-engineered, single-phase white light-emitting phosphors represent a promising avenue for the development of efficient, sustainable, and versatile phosphor materials for solid-state lighting and display applications. Over the past decade, significant advancements have been made in leveraging defects in binary, ternary, and quaternary oxides, chalcogenide, nitrides, hybrids, composites-based materials to achieve broad, tunable white light emission with intense white emission, high CRI, tunable CCT and high LE. Modifying materials with dopants, composite formation, modification of surfaces and controlled defect engineering can tailor the band position and/or introduce new energy bands in between the band edges to achieve intrinsic white light emission with impressive chromaticity and color rendering indices. These findings underscore the potential of defect-based approaches to circumvent reliance on rare-earth materials, addressing both economic and environmental concerns. Future research should focus on advancing synthesis techniques for precise defect modulation, enhancing PLQE, improving the stability and scalability of these phosphors for practical applications. With continued innovation, defect-engineered single-phase phosphors can play a transformative role in next-generation solid-state lighting technologies.

3. References

1. R. K. Tamrakar, D. P. Bisen, K. Upadhyay, I. P. Sahub and M. Sahud, *RSC Adv.*, 6, (2016), 92360-92370.
2. G. B. Nair, H.C. Swart and S.J. Dhoble, *Prog. Mater.Sci.*, 109, (2020), 100622.
3. Y. Qi, J. Zhang, H. Yu, J. Sun, X. Li, L. Cheng and B. Chen, *J. Rare Earth.*, 34, (2016), 1-6.
4. S.K. Behera, R. Kainda, S.Basu, and Y.S. Chaudhary, *Appl. Mater. Today* 27, 101407.
5. G. Liu, *Chem. Soc. Rev.*, 44, (2015), 1635-1652.
6. J. Cho, J. H. Park, J. K. Kim and E. F. Schubert, *Laser Photonics Rev.*, 11, (2017), 1600147.
7. S.K. Behera, R. Kainda, A.K. Dehury and Y.S. Chaudhary, *Journal of Luminescence* 269, 120546.
8. B. Bitnar, *Semicond. Sci. Technol.*, 18, (2003), S221.
9. J. I. Pankove, *Optical processes in semiconductors.*, Dover. 1971 ISBN 0-486-60275-3.
10. C. Zhang and J. Lin, *Chem. Soc. Rev.*, 41, (2012), 7938-7961.
11. L. Ma, B. Han, F. Zhang, L. Xu, T. Fang, S. Wang and J. Song, *Appl. Mater. Today*, 22, (2021), 100946.
12. J. Zhou, G. Zheng, X. Liu, G. Don and J. Qiu, *Coord. Chem. Rev.*, 448, (2021), 214178.
13. T. Koida, A. Uedono, A. Tsukazaki, T. Sota, M. Kawasaki and S. F. Chichibu, *Phys. Status Solidi A*. 201, (2004), 2841-2845.
14. Q. Pen, and Z. Shuai, *Aggregates*, 2, (2021), e91.
15. S. Chirakkara and S. B. Krupanidhi, *Phys. Status Solidi RRL*, 6, (2012), 34-36.
16. C. S. Biju, S. Suresha, S. Sahaya, J. Dhasa and R. G. S. Rao, *Superlattices Microstruct.*, 120, (2018), 363-369.
17. P. M. Lewis, D. Hebbar N., K. S. Choudhari and S. D. Kulkarni, *Materials Science in Semiconductor Processing*, 138, (2022), 106284.
18. D. Q. Trung, N. V. Quang de, M. T. Tran, N. V. Du bd, N. Tu, N. D. Hung f, Dao Xuan Viet f, D. D. Anh d and P. T. Huy, *Dalton Trans.*, 50, (2021), 9037-9050.
19. S. Das, U. K. Ghorai, R. Dey, C. K. Ghosh and M. Pal, *New J. Chem.*, 46, (2022), 17585.
20. C. Zhang, C. Li, J. Yang, Z. Cheng, Z. Hou, Y. Fan, and J. Lin, *Langmuir*, 25, (2009), 7078-7083.
21. M. T. S. Tavares, M. M. Melo, V. D. Araújo, R. L. Tranquilin, C. R. R. Almeida, C. A. Paskocimas, M. R. D. Bomio, E. Longo and F. V. Motta, *J. Alloys Compd.*, 658, (2016), 316-323.
22. G. S. Rodriguez, U. Pal, R. S. Zeferino, and M. E. Álvarez-Ramos, *J. Phys. Chem. C*, 124 (2020), 3857-3866.
23. A. K. Dehury, S. K. Behera, S. Chirrauri, S. Basu, and Y. S. Chaudhary, *Chemistry-An Asian Journal* 17 (24), e202200948.
24. A. Surendran & R. Tintu, *J Mater Sci: Mater Electron.*, 35, (2024), 812-824.
25. M. J. Bowers, J. R. McBride and S. J. Rosenthal, *J. Am. Chem. Soc.*, 127, (2005), 15378.
26. S. Sapra, S. Mayilo, T. A. Klar, A. L. Rogach and J. Feldmann, *Adv. Mater.*, 19, (2007), 569-572.
27. C. C. Shen and W. L. Tseng, *Inorg. Chem.*, 48, (2009), 8689.
28. V. K. Sharma, B. GuzelTURK, T. Erdem, Y. Kelestemur, and H. V. Demir, *ACS Appl. Mater. Interfaces*, 6, (2014), 3654-3660.
29. Ch. Rajesh, C. Phadnis, K. G. Sonawane, and S. Mahamuni, *Journal of Experimental Nanoscience*, 10, (2015), 1082-1092.
30. S. K. Panda, S. G. Hickey, H. V. Demir, and A. Eychmüller, *Angew. Chem.*, 123, (2011), 4524-4528.
31. Z. F. Wang, F. L. Yuan, X. H. Li, Y. C. Li, H. Z. Zhong, L. Z. Fan and S. H. Yang, *Adv. Mater.*, 29, (2017), 1702910.
32. A. Layek, P. C. Stanish, V. Chirmanov, and P. V. Radovanovic, *Chem. Mater.* 27, (2015), 1021-1030.
33. H. S. Chen, S. J. Wang, C. Jeu Lo and J. Y. Chi, *Appl. Phys. Lett.*, 86, (2005), 131905.
34. M. A. Schreuder, J. D. Gosnell, N. J. Smith, M. R. Warnement, S. M. Weissbc and S. J. Rosenthal, *J Mater. Chem.*, 18, (2008), 970-975.

35. S. Nizamoglu, E. Mutlugun, O. Akyuz, N. K. Perkgoz, H. V. Demir, L. Liebscher, S. Sapra, N. Gaponik and A. Eychmu'ller, *New J. Phys.*, 10, (2008), 023026.
36. L. E. Shea-Rohwer and J. E. Martin, *J. Lumin.*, 127, (2007), 499.
37. F. Li, C. Nie, L. You, X. Jin, Q. Zhang, Y. Qin, F. Zhao, Y. Song, Z. Chen and Q. Li *Nanotechnology*, 29, (2018), 205701.
38. S. Kar and S. Biswas, *J. Phys. Chem. C*, 112, (2008), 11144-11149.
39. X. Ren, X. Zhang, N. Liu, L. Wen, L. Ding, Z. Ma, J. Su, L. Li, J. Han, Y. Gao, *Adv. Funct. Mater.*, 25, (2015), 2182-2188.
40. P. C. Shen, M. S. Lin, and C. F. Lin, *Sci. Rep.*, 4, (2014), 4, 5307.
41. B. T. Luong, E. Hyeong, S. Yoon, J. Choi and N. Kim, *RSC Adv.*, 3, (2013), 23395-23401.
42. J. H. Kim, D. Y. Jo, K. H. Lee, E. P. Jang, C. Y. Han, J. H. Jo and H. Yang, *Adv. Mater.*, 28, (2016), 5093-5098.
43. S. Roy, S. Pramanik, S. Bhandari, and A. Chattopadhyay, *Langmuir*, 33, (2017), 14627-14633.
44. W. J. Zhang, C. Y. Pan, F. Cao and X. Yang, *J. Mater. Chem. C*, 5, (2017), 10533-10542.
45. F. Li, Z. Xia and Q. Liu, *ACS Appl. Mater. Interfaces.*, 9, (2017), 9833-9839.
46. C.R. Garcia, J. Oliva, L.A. Diaz-Torres, E. Montes, G. Hirata, J. Bernal-Alvarado and C. Gomez-Ceram. *Int.*, 45, (2019), 4972-4979.
47. T. Nakajima, M. Isobe, T. Tsuchiya, Y. Ueda and T. Kumagai, *Nat. Mater.*, 7, (2008), 735.
48. Y. Matsushima, T. Koide, M. H. Oka, M. Shida, A. Sato, S. Sugiyama and M. Ito, *J. Am. Ceram. Soc.*, 2015, 98, 1236.
49. T. Nakajima, M. Isobe, T. Tsuchiya, Y. Ueda and T. Manabe, *J. Phys. Chem. C*, 114, (2010), 5160.
50. M. Takahashi, M. Hagiwara, and S. Fujihara, *Inorg. Chem.*, 55, (2016), 7879.
51. T. Nakajima, M. Isobe, T. Tsuchiya, Y. Ueda and T. Manabe, *Opt. Mater.*, 32, (2010), 1618.
52. E. Pavitra, G. S. R. Raju, L. K. Bharat, J. Y. Park, C. H. Kwak, J. W. Chung, Y. K. Han, and Y. S. Huh, *J. Mater. Chem. C*, 6, (2018), 12746-12757.
53. M. M. Teixeira, Y. G. Gobato, L. Gracia, L. F. da Silva, W. Avansi Jr, M. Assis, R. C. de Oliveira, G. A. Prando and J. Andrés, E. Longo, *J. Lumin.*, 220, (2020), 116990.
54. M. M. Teixeira, A. F. Gouveia, Al. Gama de Sousa, L. Fernando da Silva, R. Cristina de Oliveira, M. A. San-Miguel, M. S. Li and Elson Longo, *J. Phys. Chem. C*, 124, (2020), 14446.
55. L. Bharat, S. K. Jeon, K. Krishna and J. S. Yu, *Sci. Rep.*, 7, (2017), 42348.
56. A. K. Dehury, R. Kainda, Y. S. Chaudhary, *Inorg. Chem.* 62,42, (2023), 17163-17181.
57. A. K. Dehury, M. K. Sahoo, R. Kainda, Y. S. Chaudhary, *J. Mater. Chem. C*, 12, (2024), 17807-17817



Dr. Yatendra S. Chaudhary is Senior Principal Scientist at CSIR-Institute of Minerals & Materials Technology, Bhubaneswar, India and Professor at the Academy of Scientific and Innovative Research (AcSIR), India. He is the recipient of several national and international awards/recognitions, such as the IIM Bhubaneswar Chapter Award from IIM India, the Green Talent-2011 Award from the BMBF, Germany, CSIR-Young Scientist Award-2013 from the CSIR, India, and the prestigious Marie Curie Fellowship by the European Commission for his scientific contributions. The research activities in his group are focused on various facets of materials chemistry for the development of innovative engineered materials for their application in solar fuel generation and optoelectronic devices.



Mr. Asish. K. Dehury received M. Sc degree in chemistry from Ravenshaw University Cuttack, and joined the Materials Chemistry and Interfacial Engineering Department, CSIR-IMMT, Bhubaneswar in 2019 as a Ph.D. student under the supervision of Dr. Yatendra S. Chaudhary. His current research is focused on the synthesis of nanostructures for white light emission and their fabrication of W-LED prototypes.



Ms. Rajeswari Kainda received M. Sc degree in chemistry from, NIT, Rourkela and joined the Materials Chemistry and Interfacial Engineering Department, CSIR-IMMT, Bhubaneswar in 2019 to undertake Ph.D thesis work under the supervision of Dr. Yatendra S. Chaudhary. Her current research is focused on the synthesis of nanostructures for tunable white light emission..



Mr. Soumyadarshi Khato completed his Master's in chemistry from Banaras Hindu University, Varanasi, and is currently pursuing his Ph.D in the Materials Chemistry and Interfacial Engineering Department under the supervision of Dr. Yatendra S. Chaudhary. His research interest mainly focuses on the design of nanohybrids for energy conversion applications.



Mr. Ramesh C. Mallick completed his M.Sc. in physics from Ravenshaw University, Cuttack and is currently pursuing his Ph.D in the Materials Chemistry and Interfacial Engineering Department, CSIR-IMMT, Bhubaneswar, under the supervision of Dr. Yatendra S. Chaudhary. His research areas focus on synthesis and characterization of heterostructured nanomaterials for advanced optoelectronics applications.

Water radiolysis and its impact on reactor materials

R. Puspallata^{1,2*}, D. Mal¹, L. Muniyasamy^{2,3}, R. Ramakrishnan³, S. Bera^{1,2} and T.V. Krishna Mohan¹

¹Water and Steam Chemistry Division, BARC Facilities, Kalpakkam

²Homi Bhabha National Institute, Mumbai

³PRPD, BARC Facilities, Kalpakkam

(e-mail: pushpa@igcar.gov.in)

Abstract

Radiation field in the nuclear reactors generates highly reactive radiolytic species from the radiolysis of coolants in water-cooled PWR, BWR and PHWRs using water/heavy water as coolant or moderator in their primary circuits. While an oxidizing environment will accelerate the corrosion of structural materials, reducing species; hydrogen, can pose a safety hazard. Most materials in the vicinity of nuclear facilities are exposed to fairly high radiation fields and prone to radiation-induced degradation. A comprehensive understanding of radiation-induced water decomposition and its subsequent effects on associated materials is necessary for ensuring the safe and efficient operation of nuclear reactors. Hence, it is extremely crucial to accurately analyse the concentrations of hydrogen and hydrogen peroxide/oxygen generated from radiolysis and religiously maintain water chemistry parameters. In this article, the effect of radiation on various ion exchange resins used in purification systems of nuclear reactors and metal surfaces is compiled.

1. Introduction

Materials used in nuclear technological facilities such as nuclear power plants and nuclear fuel reprocessing plants, are exposed to extremely harsh conditions of high temperature, pressure and intense radiation fields from radioactive isotopes generated from fission reactions. The knowledge gained from aqueous radiation chemistry is essential for technological applications associated with various areas of water-cooled nuclear reactors and other related technology. The two major molecular products from water radiolysis H_2 and O_2 / H_2O_2 are flammable and the cause of structural materials failure due to corrosion, respectively. These are crucial issues for the long-term safe operation of nuclear installations. Though radiolysis of water and its effect on different materials are well studied, in actual application sites the solid materials of importance are always in contact with the aqueous phase and the processes occurring at the interfaces can affect the bulk properties. Whether it is a nuclear power plant,

fuel reprocessing plant, spent fuel storage bay or radioactive waste immobilisation (repositories) facilities there are different materials, metals or alloys, which see diverse types of radiation at varying dose rates and up to different time frames [1,2]. It is reported that gamma irradiation lowers the pitting potential and shifts the corrosion potential of SS 304 L and SS 316 L (in the repository site ground-water medium) to more positive potentials (150-250 mV) due to radiolytically formed H_2O_2 [3]. Similar behaviour is also reported for carbon steel (CS) alloy [4-6]. However, such studies are scarce. In this article the effect of radiation-assisted corrosion of CS alloy ASTM 106 Gr. B and ion exchange (IX) resins (micro and macro porous) in contact with aqueous medium are discussed.

2. Radiation effect on carbon steel and the IX resins

Irradiation Effects on Carbon Steel

Carbon steel (CS) alloy forms the primary heat transport (PHT) system in a pressurised

heavy water reactor (PHWR) which transfers the heat generated in the core. The closed-loop PHT system utilizes heavy water as the coolant, circulating it through the reactor core and then to the steam generators where heat is transferred to the light water, producing steam to drive turbines for the generation of electricity. The feeder which connects multiple fuel channels (made of zirconium alloys) to the inlet and outlet headers (coupled to the tube sides of steam generators), is also primarily made of CS due to its excellent weldability. CS drums are also used for storing radioactive wastes in spent nuclear fuel repositories. While carbon steel offers

several advantages, it's essential to address the potential challenges caused by general corrosion and radiation embrittlement increasing the risk of failure. Any damage to the structural material can cause huge financial loss and can lead to loss-of-coolant-accident (LOCA) scenarios.

Processes occurring at the interface of metal-water in the presence of ionizing radiation are mainly due to exposure to both reductive and oxidative species formed from water radiolysis. These species at the water-metal interface can significantly affect the stability of CS. Hence, it was of interest to see the effect of gamma-irradiation on the corrosion of CS in neutral and alkaline pHs simulating air ingress conditions during reactor shutdown and moisture/water seepage into radioactive storage condition.

Figure 1 shows the change in surface morphology with increasing dose. The surface showed coarsening of grain structure and exfoliation of oxide at the grain boundary. Formation and agglomerations of oxide on the coupon surfaces were observed.

Irradiation-induced oxide formation and segregation at grain boundary is clearly visible at 460 kGy dose in neutral and alkaline pH (Figure 2).

In neutral pH, the roughness increased with dose, whereas for LiOH-exposed samples, it decreased. The conductivity and Fe release increased and the pH decreased on irradiation. Contact angle and AFM measurement (Figure 3) showed increasing contact angle with irradiation indicating the surface energy and wettability of the oxide surface was decreasing with dose. XRD and Raman studies (not given

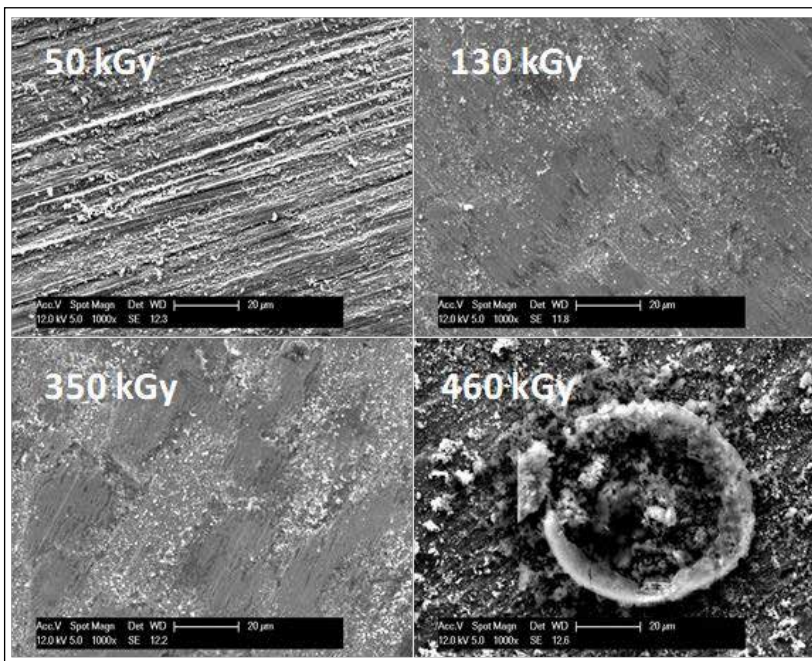


Figure 1: SEM images of CS surface exposed to different gamma doses in neutral pH.

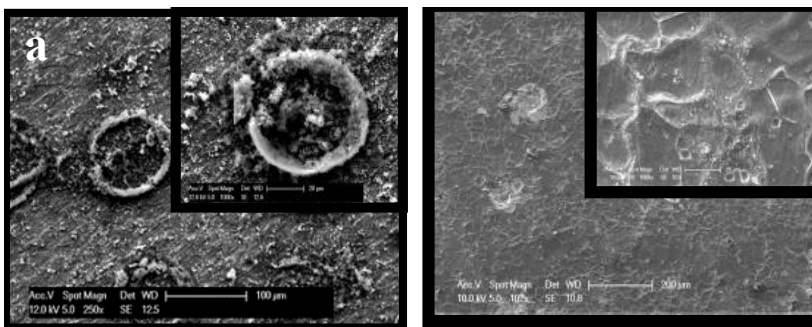


Figure 2: SEM images of CS surface exposed to 460 kGy in (a) neutral and (b) alkaline pHs.

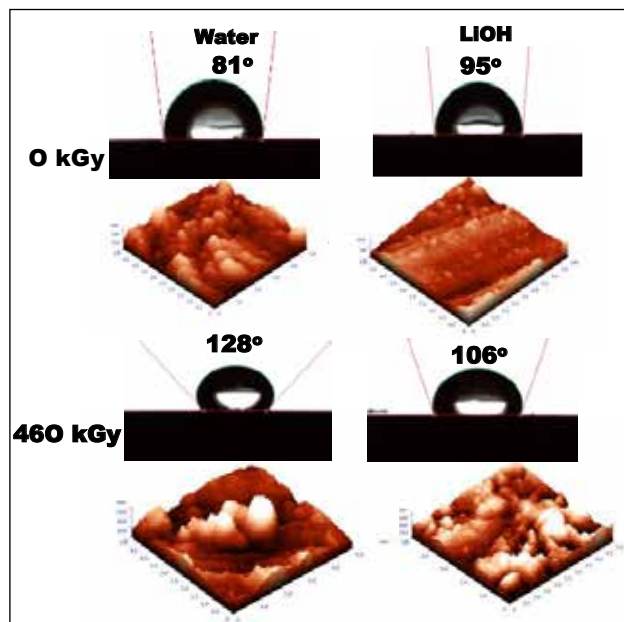


Figure 3: Contact angle and AFM micrographs of CS surfaces before and after γ -irradiation in neutral and alkaline pH.

here) indicated the presence of Fe_3O_4 , Fe_2O_3 and FeOOH

The structural materials are susceptible to corrosion in the presence of certain impurities in the coolant. Therefore, strict water chemistry control is necessary to minimize corrosion and maintain the integrity of the systems using ion exchange resins. Maintaining a clean system ensures good control over activity transport and reduces radiation field build-up in nuclear plants.

Ion exchange resins

As mentioned before ion exchange resins are indispensable in the nuclear industry, playing a critical role in maintaining the water chemistry of various circuits within nuclear power plants. These circuits, including coolant, moderator and auxiliary systems, require precise control of chemistry parameters for uninterrupted operation. Annually, nuclear facilities utilize a substantial volume of ion exchange resins, typically ranging from 10,000 to 25,000 liter, for this essential task [7]. Cation exchange resins are particularly vital in this process for effectively removing radioactive cationic contaminants

from the coolant water. These contaminants can originate primarily from radioactive (by neutron activation in the reactor core) corrosion products generated from the oxides formed on the surface of various structural materials and/or fission products released from breached/failed fuel pins. By efficiently removing these contaminants, cation resins significantly minimize radioactive transport and prevent their re-deposition within the coolant circuits thereby keeping a check on the man-rem related issues.

To withstand the demanding environment of a nuclear power plant, specially designed nuclear-grade resins are employed. These resins possess several key characteristics such as (i) high exchange capacity for efficient contaminant removal, (ii) exceptional mechanical strength to endure operational pressures and (iii) inherent resistance to thermal shocks and radiation.

Nuclear grade ion exchange (IX) resins of strong cation and anion forms, from both gel (micro-porous) and macro-porous types are being used in different purification circuits of water-cooled nuclear reactors. The macroporous resins with a pore size (voids between the polystyrene chains) ~ 20 - 100 nm, can also act as filters to trap bigger-sized particles (foulants or crud or organics) along with their normal ion exchange behavior [8]. Macro-porous resins comparatively have higher strength due to higher cross-linking ($\sim 12\%$) and hence can withstand high flow conditions. Hence, macro-pore resins are mostly used in the secondary side of the nuclear reactors i.e. mostly in steam generator condensate polishing units which get a flow of ~ 70 m^3 h^{-1} and pressure of ~ 10 bar. The operational life of these resins is finite. **Figure 4** gives a schematic diagram showing the morphology of gel and macro-porous resin beads with their pores. As the resins remove radioactive contaminants from the coolant water, they become loaded with various radionuclides, transforming them into radioactive waste. Over time, these spent resins undergo auto-irradiation due to the presence of these radioactive nuclides. This continuous radiation exposure can gradually

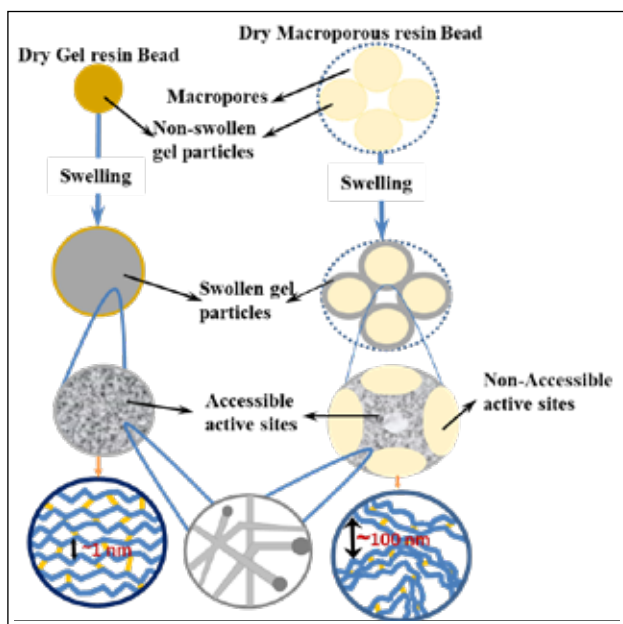


Figure 4: Schematic diagram of the macro-to-micro morphology of gel and macro-porous resin beads in the dry and swollen state.

damage the resin’s functional groups, potentially compromising its performance. The extent of radiation damage is influenced by the chemical composition, ionic form, moisture content, degree of crosslinking and the specific synthesis method employed. In general, weakly acidic resins exhibit greater radiation resistance compared to strongly acidic resins.

The stability of these resins during their long-term operational cycles or during storage as active waste, can envisage situations simulating their exposure to radiation doses which though may not be very high, but can be for an extensively long period.

The radiation stability and the extent of degradation of macro-porous (Indion 790 cation and Indion 810 anion) and nuclear grade gel (Tulsion T 46 cation and Tulison A33 anion) cation and anion resins are compared both separately and in their mixed form. The following nomenclature is used: M and G to represent macro and gel form, CIX or AIX for cation and anion exchange resins, respectively. Metal ion (Cu^{2+} and Co^{2+}) loaded (prepared by equilibrating resins with a high concentration of the metal ion

solutions) macro-porous and gel cation resins are assigned as MCIX/GCIX-Cu/Co and carbonate loaded anion resins as MAIX- CO_3^{2-} .

Figure 5 shows the change in pH and conductivity of the dispersed water medium (2 ml of resins were taken with 10 ml ultrapure water) exposed to different doses with the wet and swelled resins. The pH decreased continuously with increasing absorbed dose for cations and increased for anions.

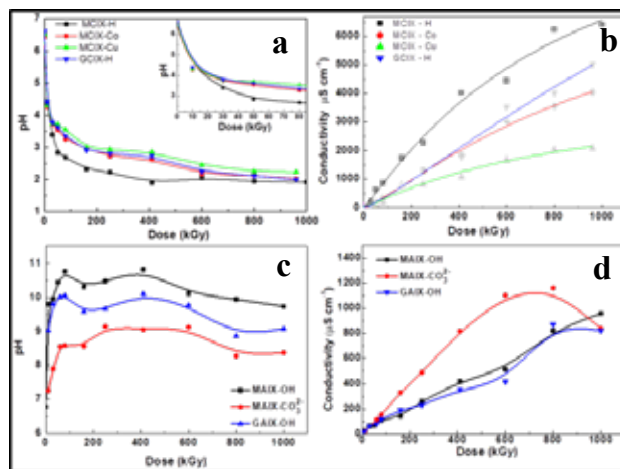


Figure 5: Variation of pH and conductivity in the aqueous phases for macro/gel cation (a, b) and anion (c, d) resins {MCIX (-■-), MCIX-Co (-●-), MCIX-Cu (-▲-) and GCIX (-▼-)} as a function of absorbed dose (Inset in (a): pH changes at lower doses).

The pH decrease was very fast at initial doses of irradiation (shown in the inset) and then tapered off at higher doses (beyond 100 kGy) indicating a faster acidity release. Within an absorbed dose of 30 kGy the pH was ~ 3.5 for all the resins. After 1000 kGy, the final pHs for MCIX-H (-■-), MCIX-Co (-●-), MCIX-Cu (-▲-) and GCIX-H (-▼-) resins were 1.91, 2.02, 2.23 and 2.0, respectively. Similarly, in the case of anion resins, maximum increase in pH was observed for macro anion resin in the OH form (i.e. MAIX-OH) and a minimum in the carbonated resins. The conductivity values of the aqueous phase also increased with dose mainly due to degradation and defunctionalization of all the resin samples. CIXs released mainly SO_4^{2-} ions and AIX indicated the formation of NH_4^+ ions

along with lower organic acids. The H_3O^+ (having high molar ionic conductivity) are formed as the counter ion to the SO_4^{2-} and other acid anions from the aqueous medium resulting in a pH decrease in CIX, whereas OH^- counter ions for NH_4^+ resulted in a pH increase in the case of AIX. Due to the generation of more and more of these ionic species with increasing absorbed doses, the overall conductivity of the aqueous medium increased (Figure 6). In metal-loaded resins (MCIX-Co and

MCIX-Cu), Cu^{2+} or Co^{2+} ions are coordinated with other exchange sites and are strongly bonded, rendering a lowering in SO_4^{2-} release. The reason behind selecting Cu^{2+} and Co^{2+} was that there is every possibility of copper ion release from the corrosion of widely used copper alloys such as cupronickel or Monel in the heat exchangers. In case there is in situ irradiation from high gamma from any radioactive nuclide, say radioactive ^{60}Co , there is a possibility of metallic copper ion release into the solution. Salt forms of resins with variable valency metal ions are reported to be more radiation resistant than H^+ forms [9,10].

This may be the reason for observing a lower SO_4^{2-} release in MCIX-Cu than MCIX-Co. The formation of lower organic acids (formate and acetate) also resulted in increased chemical oxygen demand (COD) values [11]. The ion exchange capacity of the resin decreased with dose for AIX. On the other hand, the capacity first decreased and then showed a slight increase in the case of CIX. After a dose of 160 kGy, the capacity of cation exchange resins decreased by 23% and 40% for macro-porous and gel-type cation exchange resins, respectively. This is shown below in Figure 7. An increase in capacity at higher doses may be due to the formation of new weak-acid functional groups, which can act as additional exchange sites on irradiated IX resins. About 20-65 % loss in the exchange capacity is reported in nuclear grade sulfonated polystyrene - DVB (4 %) cationic resins [12].

The surface morphological changes on the resins were observed after irradiation and the FE-SEM images are given in Figure 8. It shows some bulging-like features after irradiation in MCIX-H

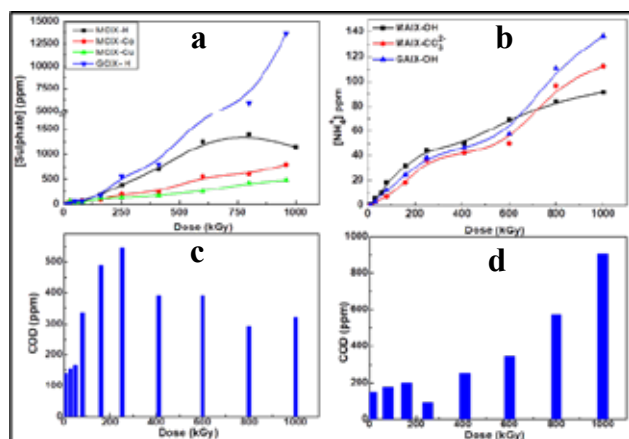


Figure 6: Variation of (a) $[SO_4^{2-}]$, (b) $[NH_4^+]$, and COD for macro cation (c) and anion (d) resins, respectively, with dose.

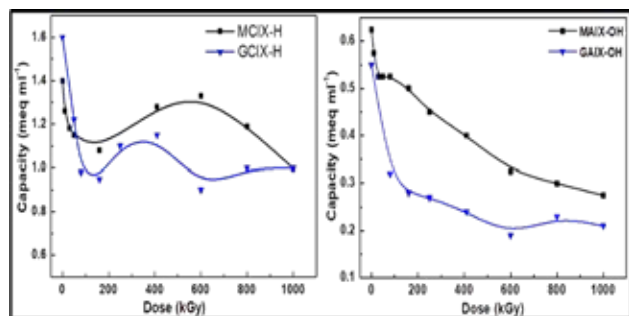


Figure 7: Change in the capacity of macro and gel resins with dose.

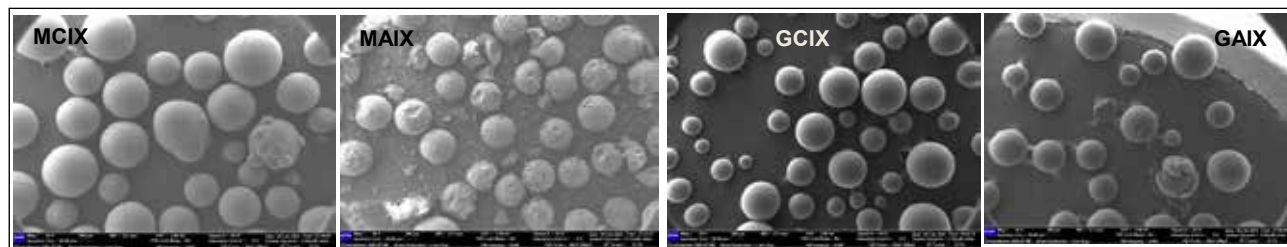


Figure 8: SEM images of macroporous and gel resins after a dose of 1000 kGy.

resins along with broken resin particles, whereas no visible change was observed in GCIX-H resins. Extensive oxidation during irradiation can contribute towards the agglomeration of resins or accumulation of gases which can be the reason behind the bulging-like features in MCIX-H. MAIX resins showed severe surface abrasion with cracked and spalled smaller fragments. These powdered forms of resin can plug the flow lines or form channelling in the resin column affecting the under-utilisation of total exchange capacities. This cracking or spallation can be due to the pressure build-up during radiolytic gaseous product formation namely H_2 , O_2 , CO , CO_2 , SO_2 , NH_3 and various hydrocarbons. The yield and process of formation of these gases is difficult to predict as it is influenced by the type of resin, absorbed dose, degree of cross-linking,

surrounding atmosphere, energy transfers and steric effects. The cation exchanger canister is reported to reach a pressure of 200 psi at about 2×10^4 kGy of exposure [12]. The major molecular products hydrogen and hydrogen peroxide yield is expected to increase in the presence of resin as the aqueous medium conductivity increases [13].

A comparison plot for hydrogen generated due to gamma irradiation of various resin samples to varying doses is shown in **Figure 9**.

An equal volume of ultrapure water without resin was taken as a blank to show the contribution from pure water radiolysis to the total volume of generated hydrogen. It was found that the amount of hydrogen (given as the percentage of hydrogen in the total headspace volume) linearly increased with the absorbed dose for all the resin samples.

The H_2 yield was observed to be higher for AIX than CIX due to the formation of extra H_2 from the quaternary ammonium group and was highest for GAIX-OH. The variation in the H_2 yield can be due to the difference in the linear energy transfer properties in varied compositions and densities of the polymers. Metal ion-substituted macro-porous resins showed a slight lowering in hydrogen yield. The variation in H_2 yield from different type of polymer makes it difficult to predict the H_2 generation during operation. For instance, the G-value for H_2 is

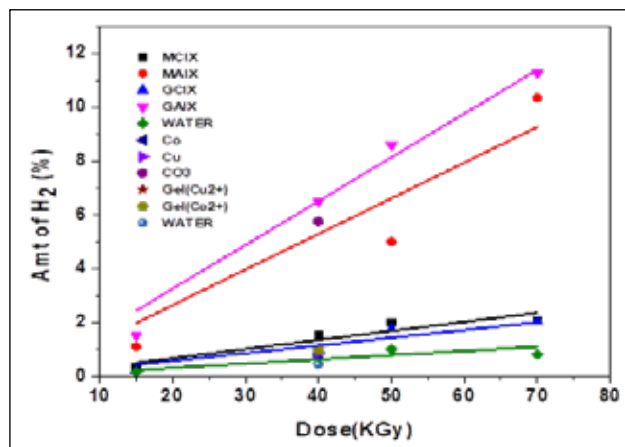


Figure 9: Percentage of H_2 generated from IX irradiation.

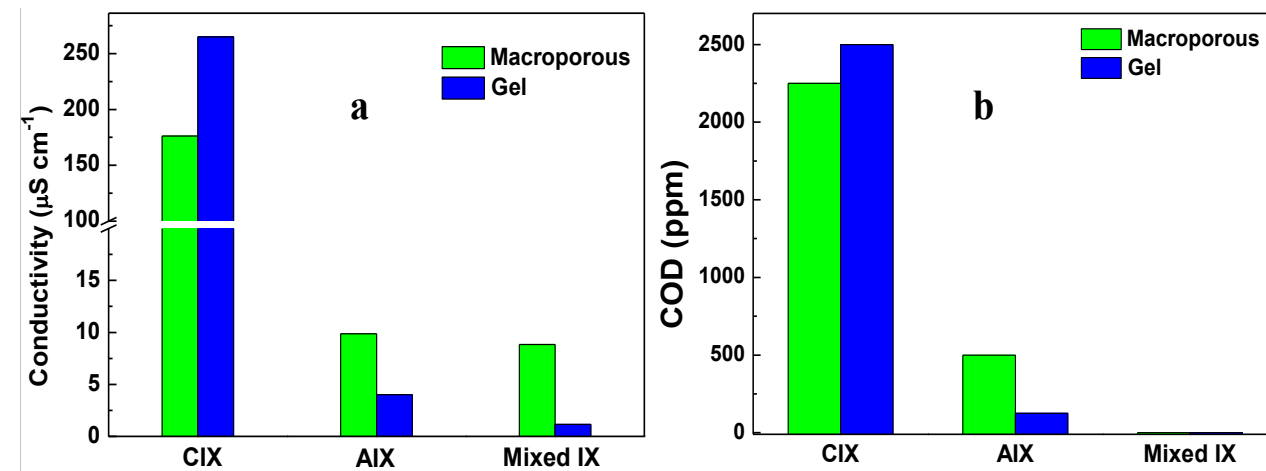


Figure 10: Change in (a) conductivity (b) COD after oxidative treatment with H_2O_2 .

0.342 $\mu\text{M J}^{-1}$ in polyethylene and 0.0034 $\mu\text{M J}^{-1}$ for polystyrene [14]. On the contrary, H_2O_2 yield was observed only with CIX resins and was highest for GCIX-H. With anion resin or mixed bed resin, no measurable H_2O_2 yield was noticed. When resins were exposed to H_2O_2 (~20 ml of 200 ppm with 5 ml resin) almost complete decomposition of H_2O_2 was observed instantly for both macro-porous (MAIX) and gel type (GAIX) anion resins and also for their mixed bed counterparts whereas, in the case of cation resins decomposition of H_2O_2 was only about ~35-40 %. **Figure 10** shows the change in conductivity and COD values from the above environment. Only the hydroxide form of the resin was reported to absorb peroxide to a great extent as compared to CO_3^{2-} forms [15].

3. Conclusions

Variations in system pH and temperature can influence the rates of oxide film growth and dissolution without affecting the oxide composition. On the other hand, gamma radiation significantly impacts the corrosion behavior and nature of the oxide film formed by increasing the electrochemical potential at the oxide-aqueous interface. This alteration in electrochemical potential dictates the formation of specific oxide phases on the steel surface. Under mildly basic conditions, the presence of ionizing radiation promotes the formation of a more protective passive film consisting of a mixture of Fe_3O_4 and $\gamma\text{-Fe}_2\text{O}_3$. Prolonged exposure to radiation can embrittle carbon steel, reducing its ductility and careful monitoring and periodic inspections are crucial to ensure the safety and reliability of the components. High-dose gamma irradiation of ion exchange resins induces chemical bond breakage, leading to the formation of various ionic species and gaseous products. While these high doses may not be typical during normal operation, significant radiation exposure does arise from short-lived radionuclides (e.g., ^{16}N , ^{17}N) and longer-lived isotopes (e.g., ^{60}Co , ^{137}Cs) accumulated on the resins. This radiation damage reduces ion exchange capacity and thus can pose a threat of radionuclide release creating

operational challenges.

Gel resins, due to their structural flexibility, exhibit greater damage. The release of sulphate ions from the sulphonic acid functional groups of cation resins will lower pH, potentially impacting the integrity of storage canisters. On the other hand, the release of ammonium ions from the ammonium functional groups of anion resins will increase pH and H_2 generation. Hydrogen gas generation requires proper venting to prevent flammability. Dewatering of resin slurries before disposal can minimize radiolytic product generation and mixed bed resins also exhibit lesser decomposition than their counterparts. A clear knowledge of the acceptable dose limits for different types of resins will facilitate informed resin selection for specific applications.

4. References

1. K. Bobrowski, K. Skotnicki, T. Szreder, in: M. Venturi, M. D'Angelantonio (Eds.), *Appl. Radiat. Chem. Fields Ind. Biotechnol. Environ.*, Springer International Publishing, Cham, 2017: pp. 147-194.
2. M. Jonsson, *Isr. J. Chem.* 54 (2014) 292-301.
3. R.S. Glass, G.E. Overturf, R.A. Van Konyenburg, R.D. McCright, *Corros. Sci.* 26 (1986) 577-590.
4. K. Daub, X. Zhang, L. Wang, Z. Qin, J.J. Noël, J.C. Wren, *Electrochim. Acta.* 56 (2011) 6661-6672.
5. S.I. Giannakandropoulou, H. Desjonqueres, C. Wittebroodt, G. Baldacchino, *Radiat. Phys. Chem.* 206 (2023) 110742.
6. D. Mal, P. Rajesh, R. Srinivasan, V. Sankaralingam, Effect of radiation on carbon steel corrosion, in: 14th Bienn. DAE BRNS Symp. Nucl. Radiochem., Mumbai, 2019.
7. F.L. Rizzo, Outlook and Desires of Ion Exchange Resin Technology Development in the Nuclear Field, in: L. Liberti, J.R. Millar (Eds.), *Fundam. Appl. Ion Exch.*, Springer Netherlands, Dordrecht, 1985: pp. 25-33.
8. Z. Hubicki, D. Kołodyńska, Selective Removal of Heavy Metal Ions from Waters and Waste Waters Using Ion Exchange Methods, in: A. Kilislioglu (Ed.), *Ion Exch. Technol.*, IntechOpen, Rijeka, 2012.
9. T. Ichikawa, Z. Hagiwara, *J. Nucl. Sci. Technol.* 10 (1973) 746-752.
10. E.D. Kiseleva, K. V. Chmutov, N. V. Kuligina, *Russ. J. Phys. Chem.* 44 (1970) 264.
11. D. Mal, R. Puspallata, S. Amirthapandian, S. Bera, T.V.K. Mohan, 211 (2023).
12. K.K.S. Pillay, *J. Radioanal. Nucl. Chem.* 102 (1986) 247-268.
13. D. Mal, R. Puspallata, S. Rangarajan, S. Velmurugan, *Radiat. Phys. Chem.* 138 (2017).
14. Z. Chang, J.A. Laverne, *J. Polym. Sci. Part A Polym. Chem.* 38 (2000) 1656-1661.
15. E.W. Baumann, Reactions of hydrogen peroxide and ion exchange resins.pdf, South Carolina, 1960.

	<p>Dr. Puspallata Rajesh completed her MSc from Ravenshaw University, Orissa and joined 37th batch of BARC Training school in 1993. She completed PhD from university of Mumbai in 2004 and post-doctoral research from University of Notre Dame, US during 2005-2007. She worked in Applied Chemistry Division, BARC, Mumbai, from 1994 - 1999 and later continued in Water & Steam Chemistry Division, Kalpakkam. Her research interests include radiolysis, electrochemical corrosion, decontamination, ion exchange resins/membranes for minimizing active waste and nano-oxide synthesis.</p>
	<p>After obtaining MSc degree from IIT Kanpur, Shri Debasis Mal joined WSCD, BARCF, Kalpakkam, in 2013, through 56th batch of BARC Training school. His research interests are electrochemical corrosion compatibility of structural materials, gamma radiolysis studies related to AHWR moderator and nano noble metal synthesis.</p>
	<p>After graduating from Manonmaniam Sundaranar University, Tirunelveli, Shri Muniyasamy L. completed one year CAT-I training and joined PRPD, BARC Facilities, Kalpakkam during 2006. He completed M.Sc., Chemistry from Madurai Kamarajar University in 2013. Currently he is working as Technical Officer. He has been involved in the analysis and maintenance of water chemistry parameters of various water cooling systems and auxiliary systems.</p>
	<p>Shri R. Ramakrishnan is currently heading the chemistry section in PRPD, BARC Facilities, Kalpakkam. He is from the 37th batch of BARC Training School. He completed his MSc (Chemistry) from Bharathidasan University, Tamilnadu in 1993. He has more than thirty years of experience in reactor water chemistry, corrosion and ion exchange resins.</p>
	<p>Dr. Santanu Bera is currently heading Surface Characterisation & Mass Transport Studies Section of Water & Steam Chemistry Division, Kalpakkam. He joined BARC during 1995 after completing his PhD from NPL, Delhi. He was awarded with STA fellowship and completed his post-doctoral fellowship from National Institute for Materials Science, Japan. His areas of interest are surface analysis, thin films and hydrothermal synthesis.</p>
	<p>Dr. T V Krishna Mohan is from 34th Batch of BARC Training school. He joined DAE after completing B. Tech (Chemical Egg.) and M.B.A. (Marketing) from Osmania University. He completed his Ph.D. in Eng. Sciences from HBNI, DAE, Mumbai, during 2016. His field of specialization is design, installation, commissioning and operation of simulated engineering loops to carry out water chemistry, biology and heat transfer experiments. He is an Outstanding Scientist and currently holding the positions of Facility Director, BARC Facilities, Head, Water and Steam Chemistry Division, Kalpakkam and Chairman of COSWAC.</p>

Extensive Modulation of Fluorescence Quantum Yield in Quantum Dots by the Presence of Permanent Dark Particles: A Single Particle Level Study

K. Kaushik[‡], C. Rao[‡], A. Salam[‡] and C. K. Nandi ^{‡*}

[‡]*School of Chemical Sciences, Indian Institute of Technology Mandi, HP-175075, India*

Email: chayan@iitmandi.ac.in

Abstract

Semiconductor quantum dots (QDs) are known for their unique optical properties resulting from quantum confinement. The surface engineering of these QDs makes them promising candidates for various optoelectronic applications. Unfortunately, the quantum yield (QY) of the QDs is extensively influenced by the intrinsic fluorescence intermittency, which is also affected by ligand engineering and the surrounding environment. The present study enlightens the understanding of fluorescence intermittency in CdTe QDs (CQDs). Our results suggested the presence of permanent dark particles by the protein surface engineering of the CQDs. These dark particles do not fluoresce at any condition and lead to a substantial decrease in the overall QY of CQDs in solution. The single-particle level analysis and fluorescence correlation spectroscopy (FCS) data confirmed the existence of the “dark fraction” that contributed to the observed phenomena upon protein conjugation.

1. Introduction

QDs, with a typical size of 2-10 nm, are a class of nanoparticles that exhibit unique optical properties due to the quantum confinement effect.¹ QDs possess size-dependent energy levels, resulting in tunable emission across the electromagnetic spectrum. They also have very high QY and narrow emission band, which makes them a suitable candidate for various optoelectronic applications. Ligand engineering² and surface functionalization³ further, make them for photonic devices,⁴ single-photon sources,⁵ and single-molecule localization microscopy.⁶ However, the intrinsic fluorescence intermittency (blinking), which occurred by the sudden jump from fluorescent “ON” state to non-fluorescent “OFF” state, restricted their applications.⁷ Controlling the fluorescence intermittency in QDs is extremely crucial for their long-term applications. The low QY is often associated with higher rates of non-radiative decay. The presence of non-radiative pathways can lead to the trapping of excitonic charge carriers, causing

a drop in QY. These trap states are often linked to various types of defects, such as crystal defects⁸ or surface defects.⁹ QY can also be affected by the photoionization of QD nanocrystals.¹⁰ When QDs are excited by light, the formation of multiexcitons leads to the creation of a charged trionic state, as one hole or electron becomes trapped or ionized at the surface. This trionic state typically exhibits low or negligible QY, contributing to an overall decline in QY.

Efforts to address these challenges have focused on enhancing the QY of QD systems. To passivate surface defects, QDs are often functionalized with electron donor species, such as sulfur-based¹¹ and they are brighter and far more photostable than organic dyes. However, severe intermittence in emission (also known as blinking or nitrogen-based ligands.¹² Additionally, a shell of high bandgap material may be formed around the QD core to prevent electrons or holes from tunneling out.^{13,14} very little is known about CGASS QDs at the single particle level. Photoluminescence blinking

dynamics of four differently emitting (blue $\lambda_{em} = 510$ nm) ions are also used to fill trap states in a manner similar to electron donor species.¹⁵ Furthermore, variations in trap state density at different energy levels imply that the choice of excitation wavelength can influence QY due to differences in the trap states.¹⁶ Interestingly, some studies suggest that increasing QD concentration may enhance the accessibility of trap states among different QDs, resulting in increased fluorescence intermittency.¹⁷

In addition to fluorescence intermittency and trionic states, some QDs in a solution may not emit at all. This finding was first observed using correlative fluorescence-AFM for various QDs.¹⁸ A higher ratio of non-emitting QDs was found in low QY QD solutions, while a lower ratio was observed in high QY samples. Similar results were noted in the solution phase, where a non-radiant fraction of QDs was identified using confocal fluorescence coincidence analysis and FCS.¹⁹ Easily excited fluorescence and high photostability. Although the frequent erratic blinking and substantial dark (never radiant) fraction is referred to as the fluorescence “dark” fraction, as it absorbs light without emitting it or emits very low-intensity light, leading to an overall decrease in QY. This dark fraction may coexist with fluorescence intermittency and could be independent of it. The fluorescent dark fraction is affected by the pH of the solution, with lower pH levels increasing its proportion.²⁰ The presence of H⁺ ions is speculated to enhance the fluorescence dark fraction. Other studies have confirmed that H⁺ ions increase dark fractions due to surface functionalization, solvent interactions, or ion interactions.^{21,22} Additionally, protein self-assembly has been shown to cause QDs to enter complete dark states.²³ The formation of completely dark particles is attributed to very rapid non-radiative processes, representing an extreme case of the dark state; interestingly, this process is reversible.

This article illustrates the bovine serum

albumin (BSA) mediated tuning of single particle blinking of water soluble CdTe QDs in biocompatible phosphate buffered saline (PBS) buffer. The ensemble data suggested a substantial decrease in the fluorescence intensity of QDs that leads to a decrease in the QY when conjugated with the protein. On the contrary, single-particle fluorescence analysis suggested an increased “ON state” time upon protein conjugation. FCS was very useful in understanding the underlying mechanism of such discrepancy in ensemble and single particle observations. FCS confirmed the existence of a “dark fraction” that contributes to the decreased QY in ensemble solution upon protein conjugation. The overall PBS-BSA media, with their rich electron center, showed great potential to reduce the trap states, tune the ON-OFF time, and finally increase the photons per cycle substantially, leading to enormous improvements in photon count rate at a single particle.

2. Results and Discussion

Water-soluble colloidal CQDs were synthesized using cadmium chloride hemipentahydrate and sodium tellurite.²⁴ Mercaptosuccinic acid was employed for surface functionalization, while sodium borohydride and hydrazine hydrate served as reducing agents. The synthesized CQDs exhibited a broad absorption spectrum from 200 to 450 nm, indicating a high density of states in both the conduction and valence bands, with a band edge absorption peak around 560 nm (**Fig. 1a**). Under ambient light, the CQDs appeared red, whereas they emitted an orange color under UV illumination. Their emission spectrum displayed a narrow profile (FWHM ~50 nm) with a maximum peak at approximately 580 nm (**Fig. 1b**). X-ray photoelectron spectroscopy (XPS) analysis confirmed the presence of cadmium, tellurium, and sulfur in the CQDs (**Fig. 1c**). High-resolution transmission electron microscopy (HR-TEM) revealed that the CQDs have an average size of 3.8 nm (**Fig. 1d**).

To understand the protein surface engineering effect on the photoluminescence properties of CQDs, they were first freeze-dried and for a comparative study, three samples were prepared by incubating 1 mg of freeze-dried CQDs in 1 ml of water (W-QDs), 1 ml of 1X PBS (P-QDs), and 1 mg of BSA in 1 ml of 1X PBS (BP-QDs). To confirm the conjugation of BSA with CQDs, FCS was utilized. The BSA-conjugated CQDs displayed a larger size and mass compared to the bare CQDs, which resulted in slower diffusion rates. FCS analysis of W-QDs and BP-

QDs revealed a diffusion time that supported the successful conjugation of BSA to the CQDs, indicated by an increase in diffusion time from 174 to 237 microseconds as seen in **Fig. 2a**. The ζ -potential measurements (**Fig. 2b**) indicated that W-QDs had a high value of -36.6 mV. However, this value decreased in P-QDs due to the presence of ions in PBS, resulting in a ζ -potential of -14.8 mV. BP-QDs displayed an even lower ζ -potential of -7.8 mV. This measurement is similar to that of BSA in a PBS solution, which is -7.5 mV. This similarity suggests a complete overlap of BSA on the surface of the CQDs. The circular dichroism (CD) spectrum in **Fig. 2c** also showed distinctive peaks at 208 and 222 nm for both BP-QDs and BSA in PBS only, indicating that the α -helicity of the BSA structure was preserved.

Next, we performed ensemble photophysical studies of these CQDs. The UV-Vis absorption spectrum for P-QDs and BP-QDs closely resembled that of W-QDs, as seen in **Fig. 3a**, with BP-QDs exhibiting a small peak around 280 nm (**Fig. 3a inset**) corresponding to the absorption of tryptophan, present in BSA. The emission spectrum profiles of all CQDs appeared similar, suggesting that the emission originated from comparable quantum states across the systems (**Fig. 3b**). The photoluminescence quantum yield (QY) was measured at 488 nm excitation, yielding 33% for W-QDs. This QY increased slightly for P-QDs to 36% but decreased significantly to 19% for BP-QDs (**Fig. 3c**). BP-QDs had previously been utilized for super-resolution microscopy

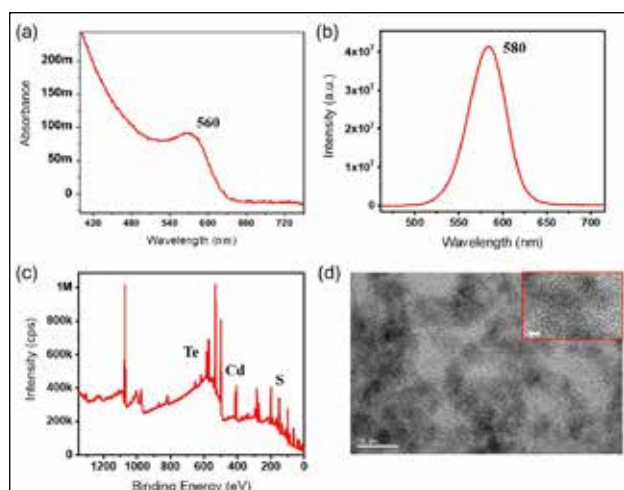


Fig. 1: (a) UV-Vis absorption spectrum for CQDs with band edge absorption at ~ 560 nm. (b) Fluorescence emission spectrum with emission maxima at ~ 580 nm. (c) XPS survey spectrum showing the presence of cadmium, tellurium and sulphur in CQDs. (d) HR-TEM showing CQDs with inset showing fringes of CdTe lattice.

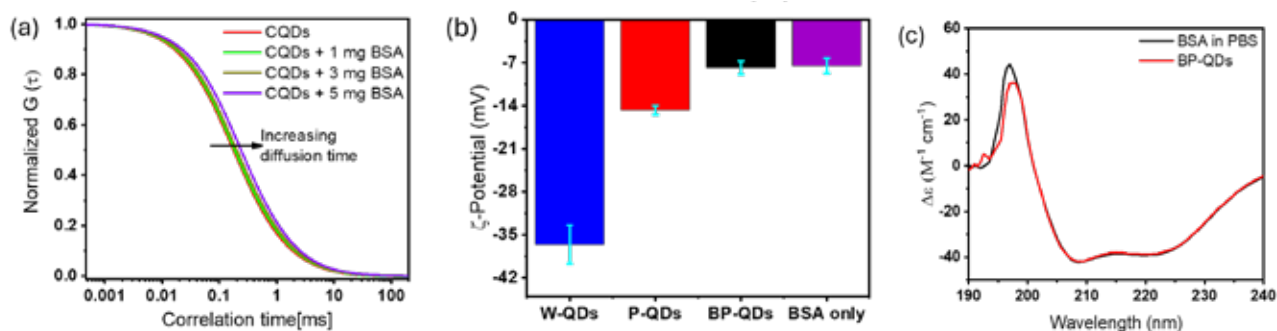


Fig. 2: (a) Diffusion time for CQDs increases with the increase in BSA concentration. (b) ζ -potential of W-QDs, P-QDs, BP-QDs and BSA in PBS. (c) CD spectrum for BSA in PBS and BP-QDs suggesting intactness of α -helicity in BP-QDs similar to BSA in PBS.

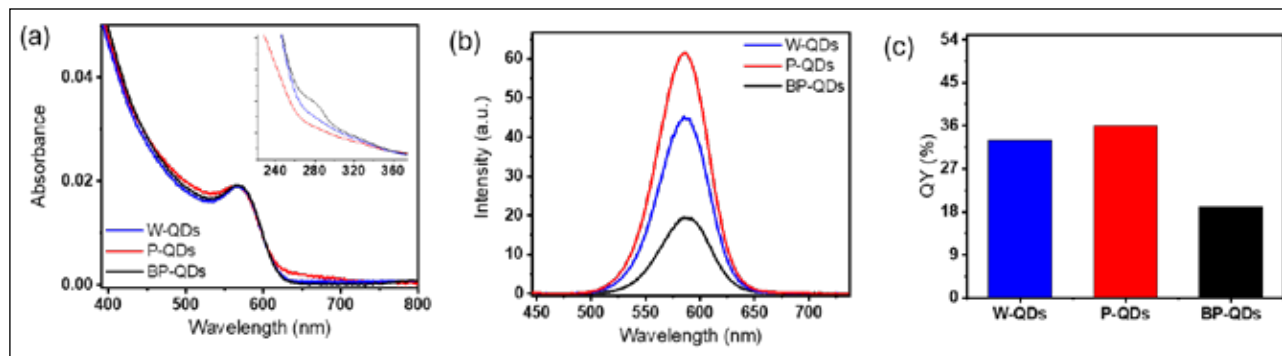


Fig. 3: (a) UV-Vis absorption spectrum of W-QDs, P-QDs, and BP-QDs showing the same band edge absorption. The inset shows a small peak at 280 nm from tryptophan of BSA. (b) fluorescence emission spectrum showing increased emission in P-QDs and decreased emission intensity in BP-QDs. (c) QY in W-QDs, P-QDs and BP-QDs.

of lysosomes, but the decrease in QY could not be fully explained earlier through bulk studies alone.²⁵ Consequently, we conducted single-particle fluorescence studies. Very dilute samples of W-QDs, P-QDs, and BP-QDs were first spin-coated onto a glass coverslip and excited using a 532 nm laser with total internal reflection fluorescence (TIRF) illumination. The emitted light was captured using a high numerical aperture (NA 1.49), 100x oil immersion Nikon objective. The captured light contained both excitation and emission, which were separated using a high-pass dichroic filter. The emission light was then directed toward an electron-multiplying charge-coupled device (EMCCD) camera filtered with a 580/70 bandpass filter. We captured several videos consisting of approximately 10,000 frames taken at 50 ms intervals (20 fps). Each video featured 70-120 individual CQDs spatially separated. We analyzed these videos using MATLAB and ImageJ macro language scripts. The QDs demonstrated significant fluorescence intermittency, with the fluorescence emission from individual CQDs switching ON and OFF stochastically.

We analyzed nearly 400 W-QDs, P-QDs, and BP-QDs by examining their fluorescence intensity-time traces and studying the ON-OFF time distribution and finally calculated the total photons coming out from single QDs. **Fig. 4a-c** presents representative time traces for W-QDs, P-QDs, and BP-QDs, respectively. W-QDs

exhibited very short bursts of photons, while P-QDs and BP-QDs displayed longer ON dwell times. We extracted individual ON-OFF times from all analyzed QDs and compiled the data into histograms in **Fig. 4d** and **Fig. 4f**. Fluorescence ON and OFF times are fitted with truncated power law and inverse power law (**Fig. 4e** and **Fig. 4g**) with the below equations.

$$\text{Truncated Power Law: } P_{\text{event}} = a \times t_{\text{event}}^{-m} \times e^{-kt_{\text{event}}} \dots (1)$$

$$\text{Power Law: } P_{\text{event}} = a \times t_{\text{event}}^{-m} \dots (2)$$

The fluorescence ON time distribution followed a truncated power law, while W-QDs and BP-QDs exhibited inverse power law behavior (Equation 2). ON time statistics indicates the trapping rate, and OFF time statistics suggest the detrapping rate of excited state electrons in different time scales. It is observed that the short ON times for all three QDs are similar (yellow region, **Figure 4e**), while the long ON of P-QDs and BP-QDs is significantly different from W-QDs (blue region, **Figure 4e**). The long ON times increased from W-QDs to P-QDs and BP-QDs. This data suggests that the trapping rate in all QDs is the same at lower time scales, while the trapping rate decreased for P-QDs and BP-QDs significantly at higher time scales in comparison to W-QDs. On the other hand, the OFF-time statistics are found to follow the inverse power law for all QDs (Eq

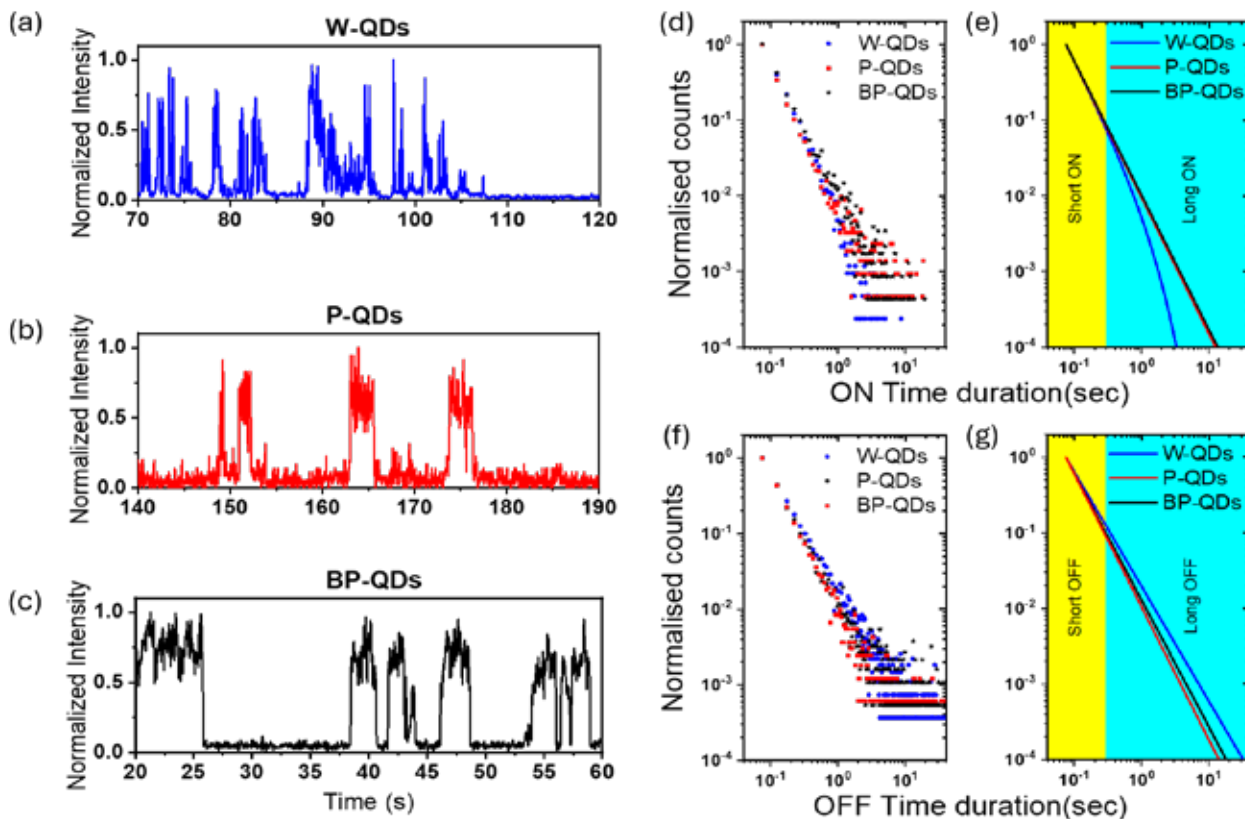


Fig. 4: (a) Representative fluorescence intensity time traces from single (a) W-QD, (b) P-QD, and (c) BP-QD. ~400 W-QDs, P-QDs, and BP-QDs were analyzed, and (d) ON times and (f) were histogrammed. (e) ON and (g) OFF times were fitted with inverse power law and truncated power law.

2). Here, both short OFF (**Figure 4g**, yellow) and long OFF (**Figure 4g**, blue) times were different for all three QDs, suggesting that detrapping rate was affected significantly both at lower and higher time scales. Both short and long OFF times decreased from W-QDs to P-QDs and BP-QDs. This data suggests that detrapping rate is increasing for P-QDs and BP-QDs, notably both at lower and higher time scales. The distinction between short (yellow region) and long (blue region) times indicates the presence of two different types of trap states. One state is influenced by the external environment, while the other is not affected. It could be proposed that one of the states, originating from surface-associated defects, is accessible to PBS ions and BSA present on the surface. These can be termed surface accessible (SA)

trap states, which are responsible for the long ON/OFF observations (blue region). The other states, attributed to core-related defects, can be called as surface inaccessible (SI) trap states, resulting in observations within the yellow region.²⁶ This is plausible since PBS and BSA can fill the SA trap states with electrons, thereby altering the trapping and detrapping rates from these states, leading to the observed long ON/long OFF times. The power law exponent, denoted as ' m_{off} ' was found to be highest for P-QDs and lowest for W-QDs (as shown in **Table 1**). This implies that electrons can more easily detrapp from the trap states in P-QDs and BP-QDs compared to W-QDs. Additionally, the smaller values of m_{off} in all three QDs relative to their monomer signifies that longer OFF events are more likely to occur than prolonged ON events.

Table 1: The power law fitting exponent for W-QDs, P-QDs, and BP-QDs when excited with a 532 nm laser.

Sample \ Parameter	m_{on}	m_{off}	t_c
W-QD	1.75	1.52	1.23 s
P-QD	1.8	1.76	--
BP-QD	1.77	1.68	--

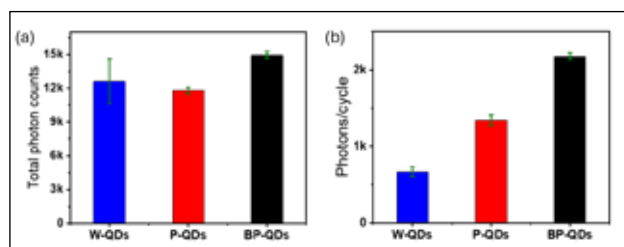


Fig. 5: Photon counting statistics from W-QDs, P-QDs, and BP-QDs. (a) average of the total photons and (b) average photons/cycle collected from ~400 QDs.

Interestingly, it was also observed that although the total number of photons did not change significantly at the single-particle level for the CQDs, the number of photons per cycle increased more than three-fold when comparing W-QDs to BP-QDs. W-QDs emitted an average total of approximately 10000 photons, P-QDs emitted about 12000 photons, and BP-QDs emitted around 14000 photons (**Fig. 5a**). The photons per switching cycle were approximately 700 for W-QDs, 1350 for P-QDs, and 2100 for BP-QDs (**Fig. 5b**). The total photon counts increased slightly in the CQDs environment, whereas the photons per cycle increased by approximately threefold at the single-particle level. Conversely, at the ensemble level, CQDs displayed different results, with the quantum yield (QY) slightly increasing from W-QDs to P-QDs before drastically decreasing in BP-QDs.

The decrease in QY may be attributed to four main factors: (1) a decrease in brightness (photon counts) of the CQDs;²⁷ (2) a decrease in the fluorescence ON time of the CQDs;²⁸ (3) an increase in the fluorescence dark fraction of

the CQDs;¹⁸ and (4) a combination of all or part of factors 1-3.^{20,26} The fluorescence dark fraction absorbs light but does not emit it. In this study, we observed an increase in fluorescent ON times, an increase in photons per cycle, and total photons, indicating that points (1), (2), and (4) are not relevant here. This supports the possibility of a fluorescent dark fraction present in the solution, which could explain the discrepancy in ensemble and single-particle fluorescence studies. The confirmation of this fluorescent dark fraction was established through detailed FCS analysis. At very low power, the FCS decay followed a pure diffusion model. By fitting the FCS curves for W-QDs and BP-QDs, we found that as the concentration of BSA in the solution increased, the number of emitters in the confocal volume decreased, while the concentration of CQDs remained constant across all solutions. This decrease in the number of emitters in the confocal volume suggests that a portion of BP-QDs entered a completely dark state. Additionally, it was noted that even with the same final concentration of QDs in all solutions, the spin-coating process did not yield the same density of dispersed QDs. Nearly three times the volume of BP-QDs was required to obtain the same density as W-QDs.

The proposed mechanism of trapping and detrapping is illustrated in Figure 6. Typically, one or two electron-hole pairs are generated following the absorption of photons by QDs. The radiative recombination of these pairs leads to the radiative ON state. However, when excited, QDs usually exhibit a positive charge.^{29,30} This has been attributed to the trapping of electrons from an exciton or biexciton pair in surface or core-related trap states (SA or SI), resulting in a system rich in holes. This condition prevents the radiative recombination of excitons, generating a trionic OFF state and leading to high fluorescence intermittency with a short OFF state. In the context of BSA, the negative charge present at pH 7, along with the combination of electron-donating amino acids, can contribute to the prefilling of trap states by PBS, which results

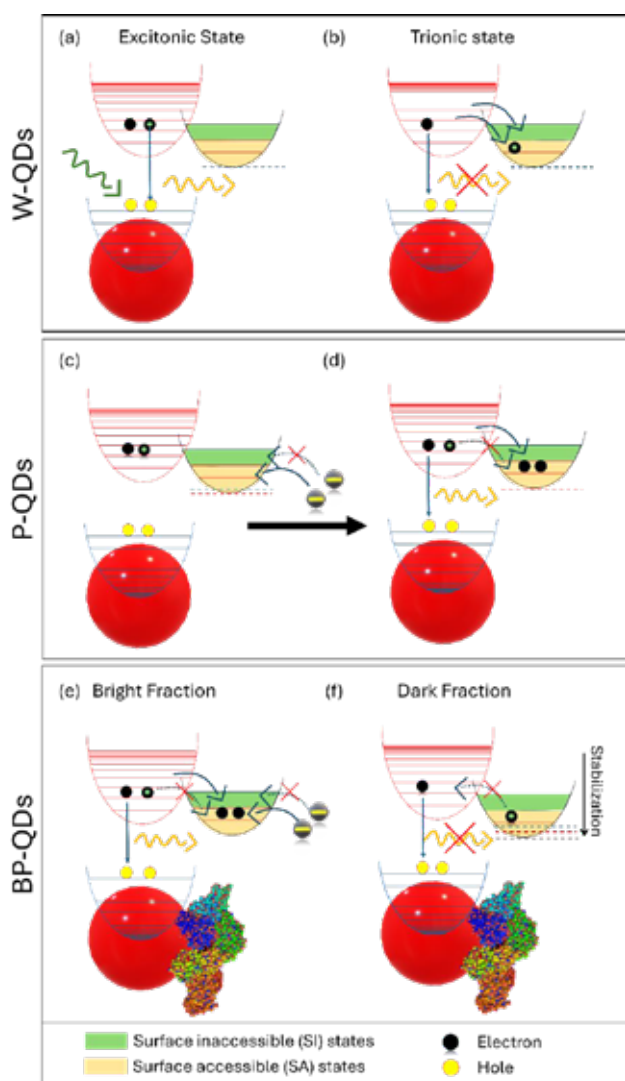


Figure 6: (a) Represents the biexcitonic state resulting in fluorescence “ON” state in QDs in water. (b) Shows the generation of trionic state, which is the reason for the fluorescence “OFF” state. (c and d) Show the plausible reason for the change in blinking behaviour due to the presence of negative ions in PBS. This prefills the SA trap states, making them inaccessible for excited state carrier electrons. SI states are not affected by the environmental factors, (e) elucidates the plausible reason for brighter fraction and enhanced “ON” time in BP-QDs, and (f) Elucidates the reason for the generation of dark fraction due to which fluorescence intensity and QY reduces.

in the bright fraction. It has been shown that positively charged species, such as H^+ ions, when in excess, can shift the band position of trap states to a lower energy level.^{19,20} This shift facilitates

electron trapping while making detrapping more challenging, thereby generating a higher number of dark states. The reduction in the band position of trap states may be more significant in BSA due to its physical interaction with QDs, which effectively decreases its surface energy. Consequently, a lower amount of dark fraction was noted in P-QDs due to the presence of anions in PBS solution, whereas an increased amount of dark state fractions was observed in BP-QDs. The bulk fluorescence intensity and quantum yield were lower in BP-QDs, necessitating a greater volume of the BP-QDs sample for spin coating to achieve the same density on glass coverslips as W-QDs for single molecule measurements. These observations corroborate the generation of dark fractions in BP-QDs, while the increase in photons per cycle confirms the presence of the bright fraction.

3. Conclusion





In this study, we analyzed the fluorescence of CdTe quantum dots under protein surface engineering various. Our ensemble photophysical studies revealed a slight increase in quantum yield for quantum dots in PBS buffers, while it decreases substantially when conjugated with protein. Interestingly, single-particle fluorescence studies showed longer ON times and shorter OFF times for protein conjugated CdTe with enhanced brightness. Through systematic studies at both bulk and single-particle levels, we identified the reasons for this discrepancy. This mismatch in fluorescent properties between ensemble and single-particle levels suggested the presence of a fraction of quantum dots that remain completely dark, referred to as the “dark fraction.” This was further confirmed by a highly sensitive fluorescence correlation spectroscopy study.

4. Acknowledgements

CKN is thankful to the Science and Engineering Research Board (SERB), India’s core research grant (CRG), for project number CRG/2020/000268. CKN is thankful for the facilities at the AMRC centre of IIT Mandi, India.

5. References

1. Murray, C. B., Kagan, C. R. & Bawendi, M. G. Synthesis and Characterization of Monodisperse Nanocrystals and Close-Packed Nanocrystal Assemblies. *Annu. Rev. Mater. Res.* **30**, (2000) 545–610.
2. Zhou, J., Liu, Y., Tang, J. & Tang, W. Surface ligands engineering of semiconductor quantum dots for chemosensory and biological applications. *Mater. Today* **20**, (2017) 360–376.
3. Karakoti, A. S., Shukla, R., Shanker, R. & Singh, S. Surface functionalization of quantum dots for biological applications. *Adv. Colloid Interface Sci.* **215**, (2015) 28–45.
4. Prabhakaran, P., Kim, W. J., Lee, K.-S. & Prasad, P. N. Quantum dots (QDs) for photonic applications. *Opt. Mater. Express* **2**, (2012) 578–593.
5. Zhu, C. *et al.* Room-Temperature, Highly Pure Single-Photon Sources from All-Inorganic Lead Halide Perovskite Quantum Dots. *Nano Lett.* **22**, (2022)3751–3760.
6. Xu, J., Tehrani, K. F. & Kner, P. Multicolor 3D Super-resolution Imaging by Quantum Dot Stochastic Optical Reconstruction Microscopy. *ACS Nano* **9**, (2015) 2917–2925.
7. Rombach-Riegraf, V. *et al.* Blinking effect and the use of quantum dots in single molecule spectroscopy. *Biochem. Biophys. Res. Commun.* **430**, (2013) 260–264.
8. Kiravittaya, S. & Schmidt, O. G. Quantum-dot crystal defects. *Appl. Phys. Lett.* **93**, (2008)173109.
9. Jiang, R., Wu, H., Manzani, D., Zhang, W. & Liu, C. Effect of surface defects on photoluminescence properties of CdSe quantum dots in glasses. *Appl. Surf. Sci.* **622**, (2023)156931.
10. Xu, X. Enhanced trion emission from colloidal quantum dots with photonic crystals by two-photon excitation. *Sci. Rep.* **3**, (2013)3228.
11. Hohng, S. & Ha, T. Near-Complete Suppression of Quantum Dot Blinking in Ambient Conditions. *J. Am. Chem. Soc.* **126**, (2004)1324–1325.
12. Mandal, A. & Tamai, N. Suppressed blinking behavior of thioglycolic acid capped CdTe quantum dot by amine functionalization. *Appl. Phys. Lett.* **99**, (2011)263111.
13. Roy, D., Mandal, S., De, C. K., Kumar, K. & Mandal, P. K. Nearly suppressed photoluminescence blinking of small-sized, blue–green–orange–red emitting single CdSe-based core/gradient alloy shell/shell quantum dots: correlation between truncation time and photoluminescence quantum yield. *Phys. Chem. Chem. Phys.* **20**, (2018)10332–10344.
14. Chen, Y. *et al.* “Giant” Multishell CdSe Nanocrystal Quantum Dots with Suppressed Blinking. *J. Am. Chem. Soc.* **130**, (2008) 5026–5027.
15. Quinn, S. D. *et al.* Surface Charge Control of Quantum Dot Blinking. *J. Phys. Chem. C* **120**, (2016)19487–19491.
16. Geißler, D., Würth, C., Wolter, C., Weller, H. & Resch-Genger, U. Excitation wavelength dependence of the photoluminescence quantum yield and decay behavior of CdSe/CdS quantum dot/quantum rods with different aspect ratios. *Phys. Chem. Chem. Phys.* **19**, (2017)12509–12516.
17. Murphy, G. P., Zhang, X. & Bradley, A. L. Temperature-Dependent Luminescent Decay Properties of CdTe Quantum Dot Monolayers: Impact of Concentration on Carrier Trapping. *J. Phys. Chem. C* **120**, (2016)26490–26497.
18. Ebenstein, Y., Mokari, T. & Banin, U. Fluorescence quantum yield of CdSe/ZnS nanocrystals investigated by correlated atomic-force and single-particle fluorescence microscopy. *Appl. Phys. Lett.* **80**, (2002)4033–4035.
19. Yao, J., Larson, D. R., Vishwasrao, H. D., Zipfel, W. R. & Webb, W. W. Blinking and nonradiant dark fraction of water-soluble quantum dots in aqueous solution. *Proc. Natl. Acad. Sci.* **102**, (2005)14284–14289.
20. Durisic, N., Wiseman, P. W., Grütter, P. & Heyes, C. D. A common mechanism underlies the dark fraction formation and fluorescence blinking of quantum dots. *ACS Nano* **3**, (2009)1167–1175.
21. Wen, Q. *et al.* Impact of D₂O/H₂O Solvent Exchange on the Emission of HgTe and CdTe Quantum Dots: Polaron and Energy Transfer Effects. *ACS Nano* **10**, (2016)4301–4311.
22. Durisic, N. *et al.* Probing the “Dark” Fraction of Core-Shell Quantum Dots by Ensemble and Single Particle pH-Dependent Spectroscopy. *ACS Nano* **5**, (2011)9062–9073.
23. Pons, T. *et al.* Single-Molecule Colocalization Studies Shed Light on the Idea of Fully Emitting versus Dark Single Quantum Dots. *Small* **7**, (2011)2101–2108.
24. Tan, J. *et al.* Facile synthesis of CdTe-based quantum dots promoted by mercaptosuccinic acid and hydrazine. *New J. Chem.* **39**, (2015)4488–4493.
25. Kaushik, K. *et al.* Protein Conjugation Helped CdTe Quantum Dots for the Specific Labeling and Super-Resolution Imaging of Lysosomes. *ChemNanoMat* **8**, (2022) e202200235.
26. Heyes, C. D. Quantum dots in single molecule spectroscopy. in *Spectroscopy and Dynamics of Single Molecules* (Elsevier, 2019)163–228. DOI:10.1016/b978-0-12-816463-1.00004-3.
27. Wong, K.-L., Bünzli, J.-C. G. & Tanner, P. A. Quantum yield and brightness. *J. Lumin.* **224** (2020)117256.
28. De, C. K. *et al.* Ultrafast Dynamics and Ultrasensitive Single-Particle Intermittency in Small-Sized Toxic Metal Free InP-Based Core/Alloy-Shell/Shell Quantum Dots: Excitation Wavelength Dependency Toward Variation of PLQY. *J. Phys. Chem. C* **123**, (2019)28502–28510.
29. Yuan, G., Gómez, D. E., Kirkwood, N., Boldt, K. & Mulvaney, P. Two Mechanisms Determine Quantum Dot Blinking. *ACS Nano* **12**, (2018)3397–3405.
30. Li, B. *et al.* Biexciton Dynamics in Single Colloidal CdSe Quantum Dots. *J. Phys. Chem. Lett.* **11**, (2020)10425–10432.

	<p>Kush Kaushik completed his B.Sc. (H) in Chemistry from Jamia Millia Islamia and subsequently earned his M.Sc. in Chemistry from IIT Mandi, Himachal Pradesh, India. He is currently pursuing a Ph.D. in Chemistry at the School of Chemical Sciences, IIT Mandi, under the supervision of Prof. Chayan Kanti Nandi. His research focuses on studying the fundamental photophysical properties of quantum dots at both single-particle and ensemble levels to gain a deeper understanding of their true nature. Additionally, he is exploring the use of quantum dots as single-photon sources for applications in quantum computing.</p>
	<p>Chethana Rao procured her Master's degree in physical science from the National Institute of Technology Karnataka, Surathkal, India. She completed her Ph.D. in 2022 under the supervision of Prof. Chayan Kanti Nandi at the Indian Institute of Technology Mandi, India. Her research was based on exploring methods of using carbon dots for bioimaging applications using Fluorescence lifetime imaging and Transmission Electron microscopy. It also involved the development of doxorubicin delivery nanocarriers with high efficacy at low dosage. Currently, she is working on applying expansion microscopy to study septins as a postdoc at Freie University with Prof. Helge Ewers</p>
	<p>Abdul Salam earned his M.Sc. in Chemistry from the Indian Institute of Technology (IIT) Mandi, India, in 2018. Since 2021, he has been pursuing his Ph.D. at IIT Mandi under the guidance of Prof. Chayan Kanti Nandi. His research primarily focuses on the development of photoluminescent metal probes for single-molecule spectroscopy, with a particular focus on their application in tracking cellular dynamics using super-resolution microscopy.</p>
	<p>Chayan Kanti Nandi, currently Professor in Physical Chemistry in the School of Chemical Sciences Indian Institute of Technology Mandi. He completed his PhD from Indian Institute of Technology Kanpur India in 2006 and moved to Germany in 2006 as an Alexander von Humboldt (AvH) fellow and then went Princeton University USA in 2009 to complete another post-doctoral research before joining to Indian Institute of Technology Mandi as an assistant Professor in 2010. He focuses his research on the interdisciplinary area of physical and biophysical chemistry, particularly spectroscopy and super resolution microscopy to understand the various organellar dynamics in living conditions. He has developed custom built single molecule spectroscopy and Stochastic Optical reconstruction Microscopy (STORM) techniques for the use of fluorescent nanomaterials in optical imaging and single photon emission. Due to his outstanding contribution Chemical Research Society of India (CRSI) awarded him the CSRI bronze medal. He has been awarded as the prestigious Fellow of Royal Society of Chemistry (FRSC) and the fellow of Indian Chemical Society (FICS).</p>

Application of Pseudorotaxane and Rotaxane in Anion-Responsive Studies

M. Jaiswal[#] and S. Dasgupta[#]

[#]National Institute of Technology Patna, Patna -800005, Bihar, India

E-mail: suvankar@nitp.ac.in

Abstract

A strong pseudo[2]rotaxane complex involving secondary ammonium salt **1-H** PF₆ and a biphenyl-23-crown-7-ether (BP23C7) is reported, with an association constant value equal to $1.6 \times 10^5 \text{ M}^{-1}$. Both the dialkylammonium salt **1-H** PF₆ and the macrocycle BP23C7 are comprised of fluorophores, *i.e.*, anthracene and catechol respectively. Energy transfer from BP23C7 to **1-H** PF₆ is observed at the excited state in the pseudo[2]rotaxane complex, leading to fluorescence quenching of BP23C7 and consequent fluorescence enhancement of anthracene. Exposure to fluoride and chloride anions disassembled the pseudo[2]rotaxane complex, invoking fluorescence recovery in BP23C7 and concomitant fluorescence quenching in anthracene due to ion-pair formation. To discriminate between the hard halide anions, a metastable [2]rotaxane (**3-H** PF₆) is synthesized, which involves 23-crown-7-ether (23C7) macrocycle interlocked with an axle comprising anthracene and cyclohexyl stoppers. The [2]rotaxane, **3-H** PF₆, exhibited deslippage of 23C7 only in presence of fluoride anions, resulting in dramatic fluorescence quenching. Adding excess amount of chloride, bromide and iodide anions did not perturb the [2]rotaxane architecture. Furthermore, this system could be used for detecting fluoride anions in acetonitrile-water (v/v = 99/1) down to $7.36 \times 10^{-7} \text{ M}$.

1. Introduction

Non covalent forces such as hydrogen-bonding and electrostatic interactions are directed toward creating interpenetrated supramolecular architectures, *i.e.*, pseudo[2]rotaxanes, which can be covalently captured to obtain mechanically interlocked molecules (MIMs) by organic transformations.^{1,2} The simplest topology of MIMs are catenane and rotaxane. A pseudo[2]rotaxane architecture constitutes an axle penetrated through the cavity of a macrocycle due to intercomponent non covalent interactions. A [2]rotaxane is obtained upon kinetically locking the macrocycle by stoppering the termini of the axle of a pseudo[2]rotaxane (**Figure 1a**). In addition a [2]rotaxane could also be generated by protocols such as “slippage” of a macrocycle over an axle and “clipping” of macrocyclic precursor over an axle (**Figure 1b & 1c**).

Typically weak non-covalent interactions

present in pseudo[2]rotaxanes and [2]rotaxanes are exploited to cause disassembly of the axle and macrocycle components, making such molecules ideal candidate for stimuli-responsive investigations.³ Consequently, an array of application as responsive polymers,⁴ responsive nanofibres,⁵ fluorescent sensors,⁶ anion sensors,⁷ molecular electronics,⁸ molecular information ratchet,⁹ metal-organic frameworks,¹⁰ superbases,¹¹ mechanically chiral molecules,¹² catalysis,¹³ nanovalves,¹⁴ controlled drug release,¹⁵ molecular switches and machines,¹⁶ have been reported. However, fluoride anion responsive studies with rotaxane remain limited. Although fluoride anion is crucial for maintaining dental and skeletal health in animals, but excessive intake of fluoride can lead to fluoride toxicity or fluorosis.¹⁷ Developing selective fluoride anion sensors are challenging especially due to the difficulty in distinguishing between two closely related hard anions fluoride and chloride.

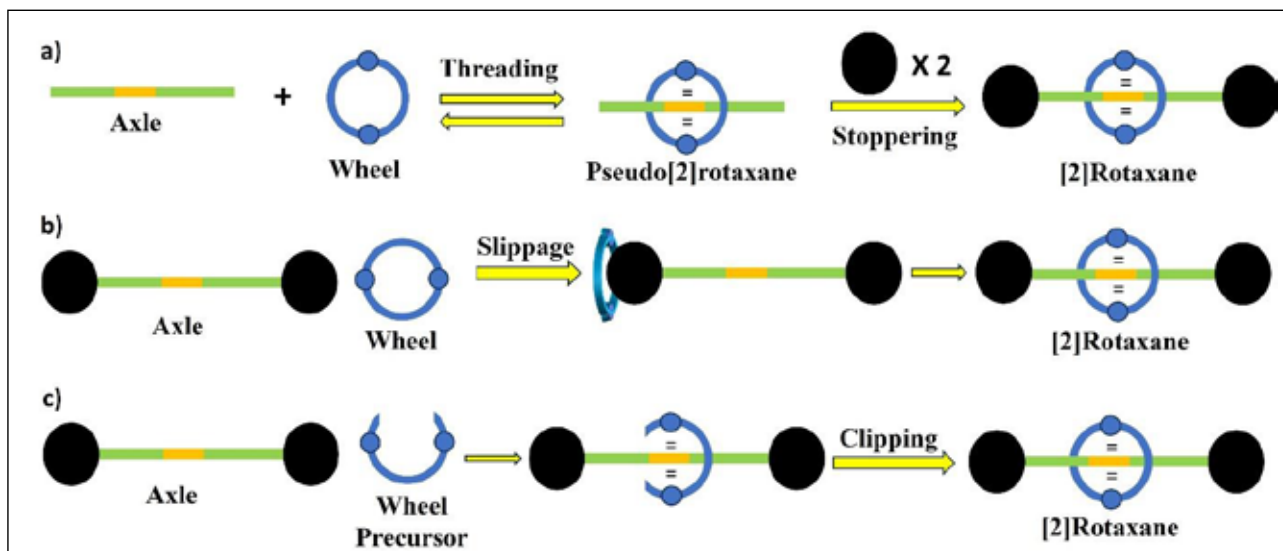


Figure 1: Cartoonic representation of protocols for synthesis of [2]rotaxane: a) Threading-followed-by-stoppering, b) slippage and c) clipping.

So far, rotaxane-based fluoride anion sensors employed three strategies. An earlier strategy relied on binding of fluoride in the preorganized binding pocket of a [2]rotaxane.¹⁸ Self-immolative rotaxane involved silyl ether stoppers which destructively reacted with fluoride anion leading to dethreading of the axle from the macrocycle cavity, causing a change in fluorescence output.¹⁹ Lastly, bistable [2]rotaxane involved macrocycle switching from one recognition station to another in presence of fluoride anion, triggering a change in NMR as well as fluorescence spectroscopy.²⁰ However, the selectivity and response time in such prior arts need improvement. To address the above issues, we designed a pseudo[2]rotaxane ($1\text{-H}\subset\text{BP23C7}\cdot\text{PF}_6$), a metastable [2]rotaxane ($3\text{-H}\cdot\text{PF}_6$), and extensively investigated their halide anion-responsiveness.

2. Results and discussion

Anthracene terminated pseudo[2]rotaxane $1\text{-H}\subset\text{BP23C7}\cdot\text{PF}_6$

Herein, we use an equimolar mixture of biphenyl-23-crown-7-ether (BP23C7) and an anthracene stoppered dialkylammonium salt $1\text{-H}\cdot\text{PF}_6$ for generating a pseudo[2]rotaxane $1\text{-H}\subset\text{BP23C7}\cdot\text{PF}_6$ (Figure 2). BP23C7 is an

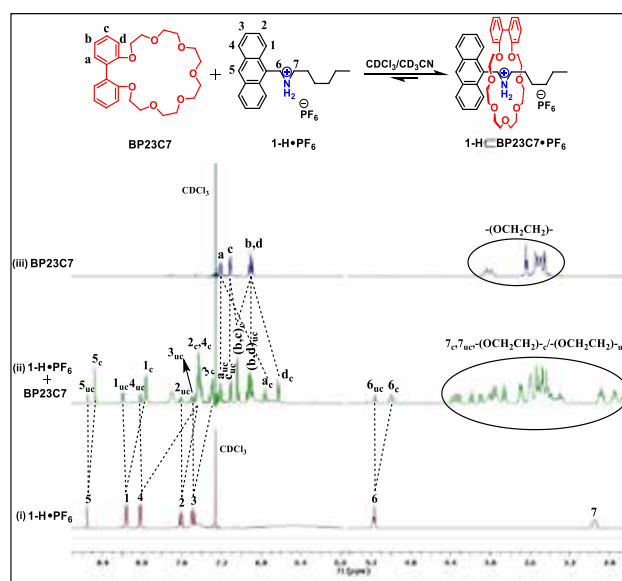


Figure 2. ^1H NMR (500 MHz, $\text{CDCl}_3/\text{CD}_3\text{CN}=11:1$, 5mM) spectra of (i) $1\text{-H}\cdot\text{PF}_6$, (ii) Equimolar mixture of $1\text{-H}\cdot\text{PF}_6$ and BP23C7, (iii) BP23C7. Dotted lines are drawn to indicate the presence of complexed and uncomplexed species, highlighting the formation of the pseudo[2]rotaxane species $1\text{-H}\subset\text{BP23C7}\cdot\text{PF}_6$.

aromatic crown ether and exhibits fluorescence due to the presence of catechol moiety. The dialkylammonium salt ($1\text{-H}\cdot\text{PF}_6$) comprised of hexyl end group threaded through the cavity of BP23C7, which resulted in the appearance of complexed (H_{c}) and uncomplexed benzylic

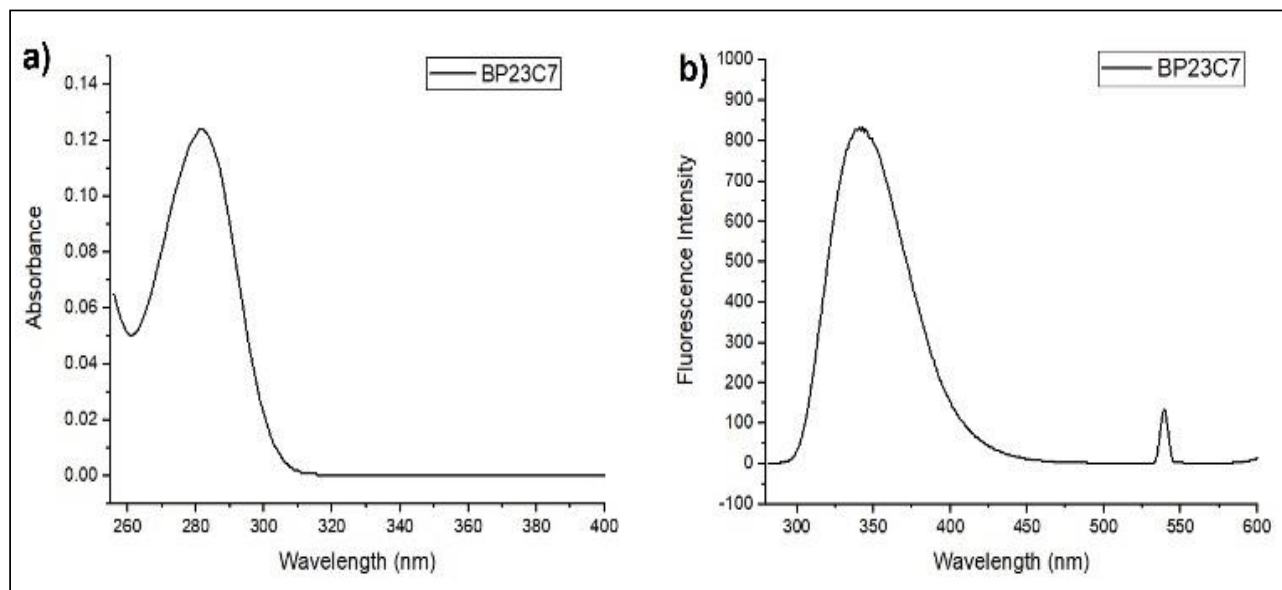


Figure 3. (a) Absorption spectrum (CH_2Cl_2 , 298 K) of BP23C7 (2×10^{-5} M); (b) Fluorescence spectrum ($\lambda_{\text{exc}} = 270$ nm, CH_2Cl_2 , 298 K) of BP23C7 (2×10^{-5} M).

protons ($\text{H}_{6\text{uc}}$) in NMR spectroscopy (**Figure 2(ii)**), unambiguously indicating the pseudo[2] rotaxane geometry. All the aromatic protons (H_{1-5}) of the axle $\mathbf{1-H} \cdot \text{PF}_6$ displayed both complexed and uncomplexed protons, with the complexed protons being upfield shifted (**Figure 2(ii)**). Similarly, the aromatic protons ($\text{H}_{\text{a-d}}$) of BP23C7 experienced both upfield and downfield shifts (**Figure 2(ii)**). The ethylene glycol protons (of BP23C7) exhibited complexed and uncomplexed peaks, ranging from 2.7-4.3 ppm, which also included the complexed ($\text{H}_{7\text{c}}$) and uncomplexed peak ($\text{H}_{7\text{uc}}$) of the axle $\mathbf{1-H} \cdot \text{PF}_6$. All the above observation implies the pseudo[2]rotaxane $\mathbf{1-H} \subset \text{BP23C7} \cdot \text{PF}_6$ formation is slow on NMR timescale. Furthermore, the nominal ESI-MS spectrum of the equimolar mixture of BP23C7 and salt $\mathbf{1-H} \cdot \text{PF}_6$, displayed a strong peak at $m/z = 724.5$, corresponding to the monocationic species $\mathbf{1-H}^+ \subset \text{BP23C7} [\text{M} \cdot \text{PF}_6]^+$.

To the best of our knowledge, photophysical studies with BP23C7 has never been reported. The absorption spectrum of BP23C7 in dichloromethane provided λ_{max} at 282 nm (**Figure 3a**) and excitation of the same solution at 270 nm afforded a fluorescence band from

300-400 nm with a λ_{max} at 340 nm (**Figure 3b**). Spectrofluorometric experiments involving BP23C7 and axle $\mathbf{1-H} \cdot \text{PF}_6$ are performed in dichloromethane solution in the concentration range of 10^{-5} M. Upon one equivalent addition of the axle $\mathbf{1-H} \cdot \text{PF}_6$ to a 2×10^{-5} M solution of BP23C7 in dichloromethane, significant fluorescence quenching of BP23C7 is observed along with the sensitization of anthracene fluorescence ($\lambda_{\text{exc}} = 270$ nm), which is due to the energy transfer at the excited state (**Figure 4b**).^{21,22} Further addition of one more equivalent of the axle $\mathbf{1-H} \cdot \text{PF}_6$ led to complete quenching of the BP23C7 fluorescence and consequent fluorescence sensitization of the anthracene. Corresponding absorbance study of the 1:1 mixture of BP23C7 and the axle $\mathbf{1-H} \cdot \text{PF}_6$ (2×10^{-5} M) in dichloromethane, reveals typical absorption peaks of both BP23C7 ($\lambda_{\text{max}} = 282$ nm) and anthracene moiety ($\lambda_{\text{max}} = 355$, 370, and 390 nm) in the absorption spectrum (**Figure 4a**, dashed line). **Figure 4a** also depicts the absorbance of the 1:2 mixture of BP23C7 and the axle $\mathbf{1-H} \cdot \text{PF}_6$ (solid line), highlighting the increase in absorbance of the anthracene band corresponding to increase in concentration of the axle $\mathbf{1-H} \cdot \text{PF}_6$ (4×10^{-5} M).

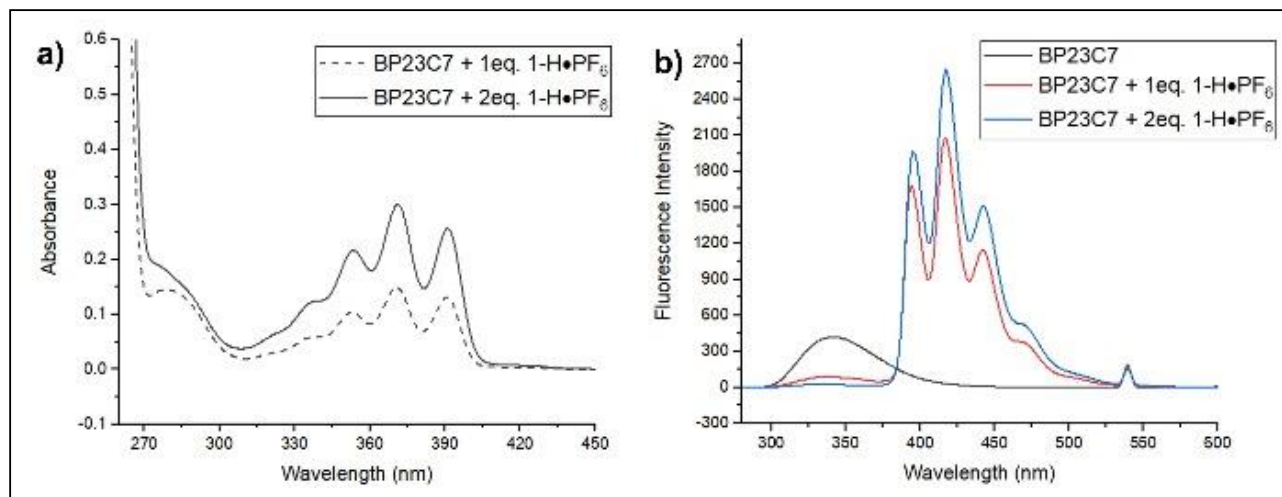


Figure 4. a) Absorption spectra (CH₂Cl₂, 298 K) of BP23C7 (2 x 10⁻⁵ M) + 1eq. 1-H·PF₆ (dashed), BP23C7 + 2eq. 1-H·PF₆ (solid); b) Fluorescence spectra (λ_{exc} = 270 nm, CH₂Cl₂, 298 K) of BP23C7 (black, 2 x 10⁻⁵ M), BP23C7 + 1eq. 1-H·PF₆ (red), and BP23C7 + 2eq. 1-H·PF₆ (blue).

Stimuli-responsive investigations of 1-H⊂BP23C7·PF₆

The energy transfer from BP23C7 to the anthracene moiety is possible due to their proximity in the pseudo[2]rotaxane species 1-H⊂BP23C7·PF₆. Any stimulus which favours the dissociation of pseudo[2]rotaxane 1-H⊂BP23C7·PF₆ will thus possibly be detected through fluorescence recovery of the BP23C7 in this system. Thus, we contemplated to use this pseudo[2]rotaxane system (1 eq. BP23C7 + 2 eq. 1-H·PF₆) for fluoride anion and chloride anion sensing (Figure 5a). As anticipated, addition of two equivalents of TBAF (i.e. one equivalent w.r.t. to the axle 1-H·PF₆) to this system, resulted in the fluorescence “turn-on” of BP23C7 with concomitant decrease in the fluorescence intensity of the anthracene band (Figure 5c). This is caused by the formation of an ion-pair 1-H·F followed by neutralization in dichloromethane, leading to the dissociation of BP23C7 from the pseudo[2]rotaxane geometry and consequent fluorescence recovery of BP23C7.²³ Further addition of TBAF did not alter the fluorescence output, indicating saturation. Surprisingly, the anthracene fluorescence band has significantly quenched. This phenomenon cannot be solely due to the dethreading of the anthracene axle

1-H⁺ from the BP23C7 cavity but also due to the generation of the neutral amine 1 in the non-polar medium.

Next, we investigated the effect of chloride anion addition into the pseudo[2]rotaxane system (1 eq. BP23C7 + 2 eq. 1-H·PF₆). Upon addition of two equivalents of TBACl to this system (i.e. one equivalent w.r.t. to axle 1-H·PF₆), fluorescence “turn-on” of BP23C7 has been observed yet again along with simultaneous decrease in the fluorescence intensity of the anthracene band (Figure 5c). This is caused by the formation of an ion-pair 1-H·Cl in dichloromethane, leading to the dissociation and fluorescence recovery of BP23C7. Further addition of TBACl did not alter the fluorescence output, indicating saturation. The observations for TBAF and TBACl additions to the pseudo[2]rotaxane system are very similar as far as the fluorescence “turn-on” output of BP23C7 is concerned. However, a striking difference between the two can be observed by zooming into the anthracene band, where for the same concentration, TBAF addition resulted in more than 50% quenching than the TBACl addition (Figure 5c). The corresponding absorbance data, after addition of both TBAF (solid line) and TBACl (dashed line) to the pseudo[2]rotaxane (1 eq. BP23C7 + 2 eq.

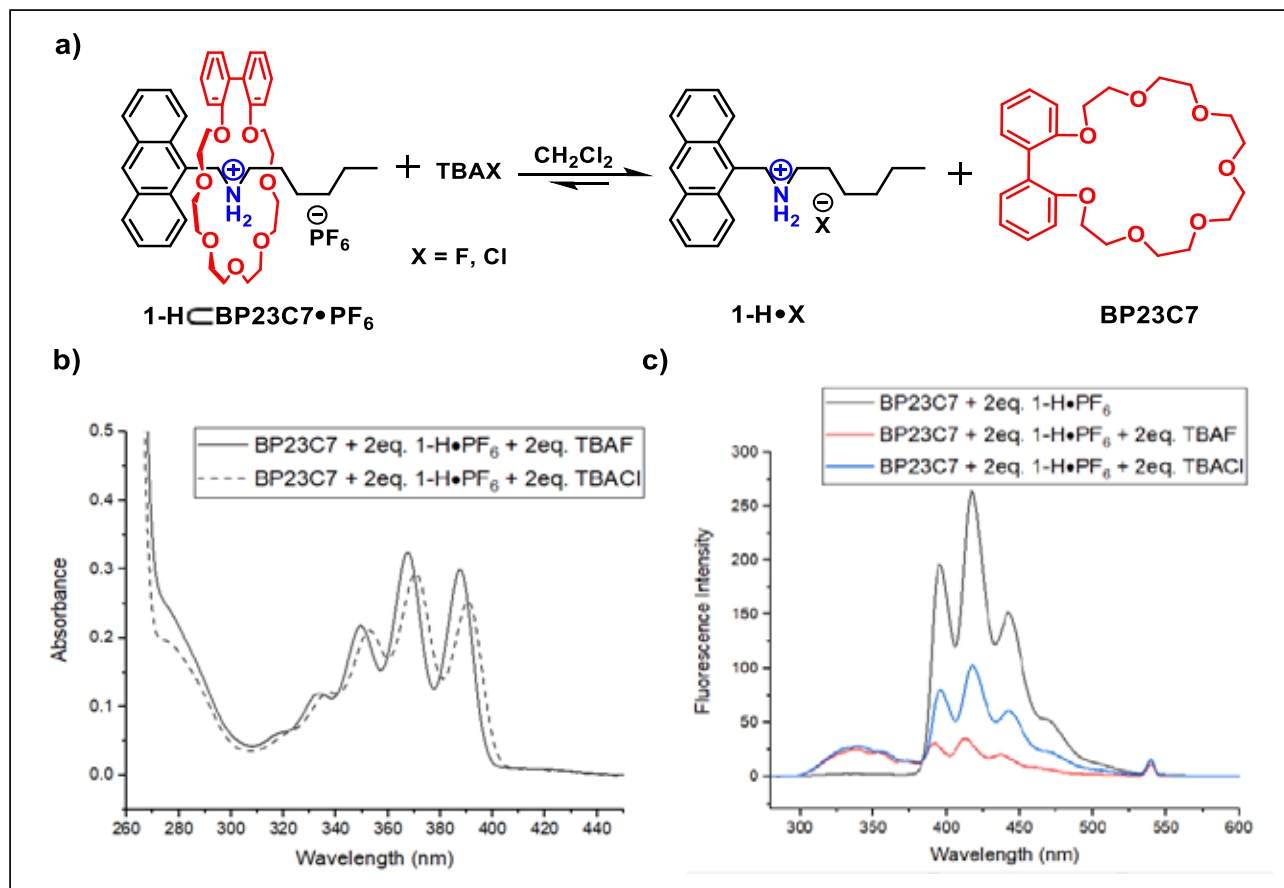


Figure 5. a) Scheme depicting dissociation of pseudo[2]rotaxane species $1\text{-H}\subset\text{BP23C7}\cdot\text{PF}_6$ in presence of stimuli (TBAF and TBACl); b) Absorption spectra (CH_2Cl_2 , 298 K) of BP23C7 ($2 \times 10^{-5} \text{ M}$) + 2eq. $1\text{-H}\cdot\text{PF}_6$ + 2eq. TBAF (solid), and BP23C7 + 2eq. $1\text{-H}\cdot\text{PF}_6$ + 2eq. TBACl (dashed); c) Fluorescence spectra ($\lambda_{\text{exc}} = 270 \text{ nm}$, CH_2Cl_2 , 298 K) of BP23C7 ($2 \times 10^{-5} \text{ M}$) + 2eq. $1\text{-H}\cdot\text{PF}_6$ (black), BP23C7 + 2eq. $1\text{-H}\cdot\text{PF}_6$ + 2eq. TBAF (red), and BP23C7 + 2eq. $1\text{-H}\cdot\text{PF}_6$ + 2eq. TBACl (blue).

$1\text{-H}\cdot\text{PF}_6$) system, can be observed in **figure 5b**. To corroborate the formation of an ion-pair $1\text{-H}\cdot\text{Cl}$ and its reduced tendency to bind with BP23C7, association constant evaluation by fluorescence titration was done with both $1\text{-H}\cdot\text{PF}_6$ and $1\text{-H}\cdot\text{Cl}$. The change in fluorescence quenching of BP23C7 was plotted with increasing guest concentrations (**Figure 6a & 6c**). The association constant values, evaluated using Benesi-Hildebrand equation indicates 10-fold weaker binding constant for $1\text{-H}\cdot\text{Cl}$ with BP23C7 in comparison with $1\text{-H}\cdot\text{PF}_6$ (**Figure 6b & 6d**). Therefore, it is not surprising that the addition of TBACl triggered dissociation of $1\text{-H}\subset\text{BP23C7}\cdot\text{PF}_6$.

As we understand, a simple pseudo[2] rotaxane species $1\text{-H}\subset\text{BP23C7}\cdot\text{PF}_6$ can detect both fluoride and chloride anions at low

concentrations ($\sim 10^{-5} \text{ M}$). Although fluorescence recovery of BP23C7 for both fluoride and chloride anions are same for the same concentration, the distinguishing feature between the two lies in the extent of quenching of the anthracene fluorescence band. However, this feature alone may not be enough to distinguish between the fluoride and chloride anions. Consequently, we contemplated to use a dialkylammonium salt terminated with a bulkier end group to increase the resistance of the macrocycle from undergoing extrusion, which may bring about selectivity in halide anion-responsive studies.

Synthesis of a [2]rotaxane $3\text{-H}\cdot\text{PF}_6$

A dialkylammonium axle comprising cyclohexyl end group and anthracene stopper,

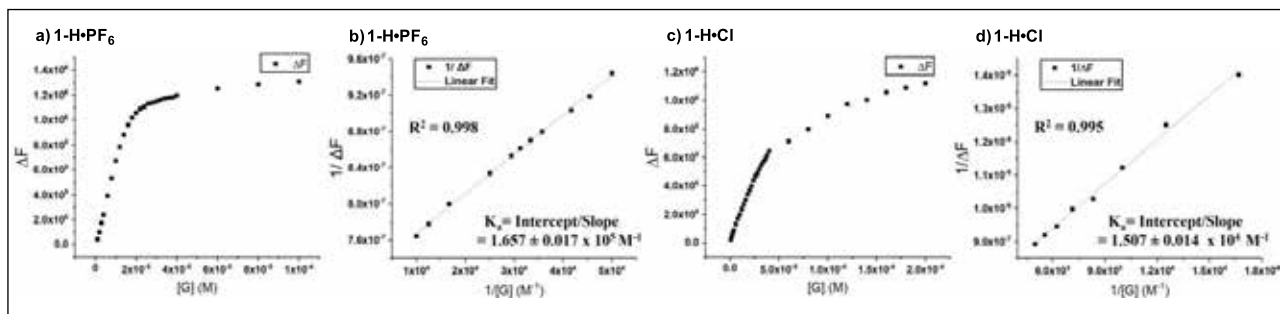


Figure 6. a) Plot of change in fluorescence quenching of BP23C7 with concentration of $1\text{-H}\cdot\text{PF}_6$; (b) Benesi-Hildebrand plot from fluorescence titration data of (a); c) Plot of change in fluorescence quenching of BP23C7 with concentration of $1\text{-H}\cdot\text{Cl}$; d) Benesi-Hildebrand plot from fluorescence titration data of (c). The concentration of BP23C7 is 2×10^{-5} M.

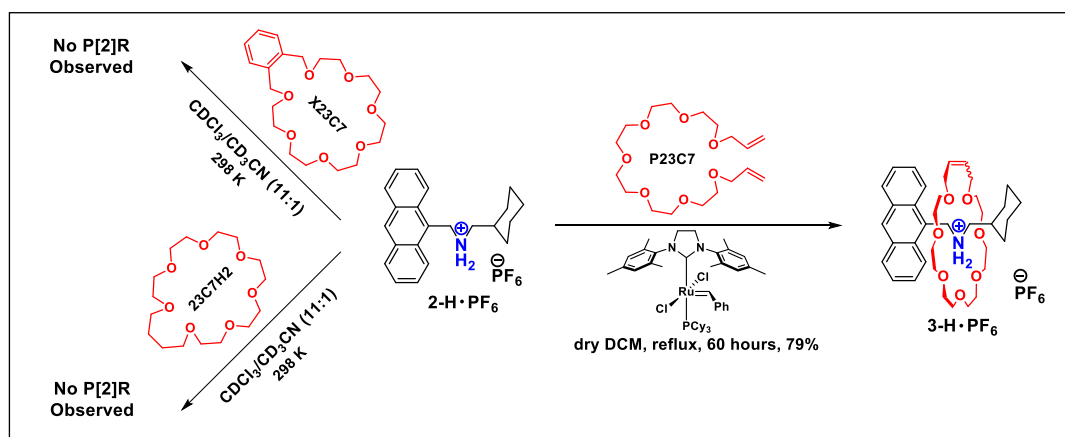
$2\text{-H}\cdot\text{PF}_6$, was chosen. Equimolar mixture of $2\text{-H}\cdot\text{PF}_6$ and *o*-xylene-capped [23]crown-7-ether (X23C7) did not generate any pseudo[2]rotaxane complexed species (**scheme 1**). A more flexible alternative of [23]crown ether (23C7H₂) failed as well to generate a pseudo[2]rotaxane with $2\text{-H}\cdot\text{PF}_6$, projecting cyclohexyl moiety as stoppers in [2]rotaxanes with [23]crown ether. Consequently, a [2]rotaxane synthesis was attempted with ring-closing-metathesis (RCM) of diolefin terminated precursor of [23]crown-7-ether (P23C7)²⁴ in the presence of axle $2\text{-H}\cdot\text{PF}_6$ (**Scheme 1**). Two equivalents of P23C7, Grubbs second generation catalyst (5 mol %) and refluxing in dichloromethane for 60 hours, followed by quenching and purification, afforded the pure isolated [2]rotaxanes, $3\text{-H}\cdot\text{PF}_6$ (79%).

The stacked ¹H NMR spectra (**Figure 7**) indicates the formation of a [2]rotaxane, $3\text{-H}\cdot\text{PF}_6$.

Downfield shift of the axle protons, upfield shift of the 23C7 protons and splitting of the H_A protons of 23C7 into H_a and H_{a'}, denote the interlocked nature of the [2]rotaxane $3\text{-H}\cdot\text{PF}_6$ (**Figure 7(ii)**). The glycol protons exhibited splitting as well. NOE cross peaks correlated the glycol protons of 23C7 with the aromatic (H_r, H_s), benzylic (H_b) and cyclohexyl (H_{Cy}) protons of the axle in $3\text{-H}\cdot\text{PF}_6$. In addition, peak at *m/z* = 638.4042 along with isotopic distribution in the HR ESI-MS spectrum, unambiguously confirmed the isolation of pure [2]rotaxane $3\text{-H}\cdot\text{PF}_6$.

Kinetic stability of $3\text{-H}\cdot\text{PF}_6$ in C₂D₂Cl₄ at high temperature

Subsequently, the integrity of the [2]rotaxane $3\text{-H}\cdot\text{PF}_6$ in non-polar media (tetrachloroethane-d₂, C₂D₂Cl₄) was investigated. On heating a 10 mM solution of $3\text{-H}\cdot\text{PF}_6$ in C₂D₂Cl₄ up to 373



Scheme 1. Axle $2\text{-H}\cdot\text{PF}_6$ failed to thread through the cavity of X23C7 and 23C7H₂ to generate pseudo[2]rotaxane. Ring-closing-metathesis (RCM) with P23C7 in presence of $2\text{-H}\cdot\text{PF}_6$ afforded a [2]rotaxane, $3\text{-H}\cdot\text{PF}_6$.

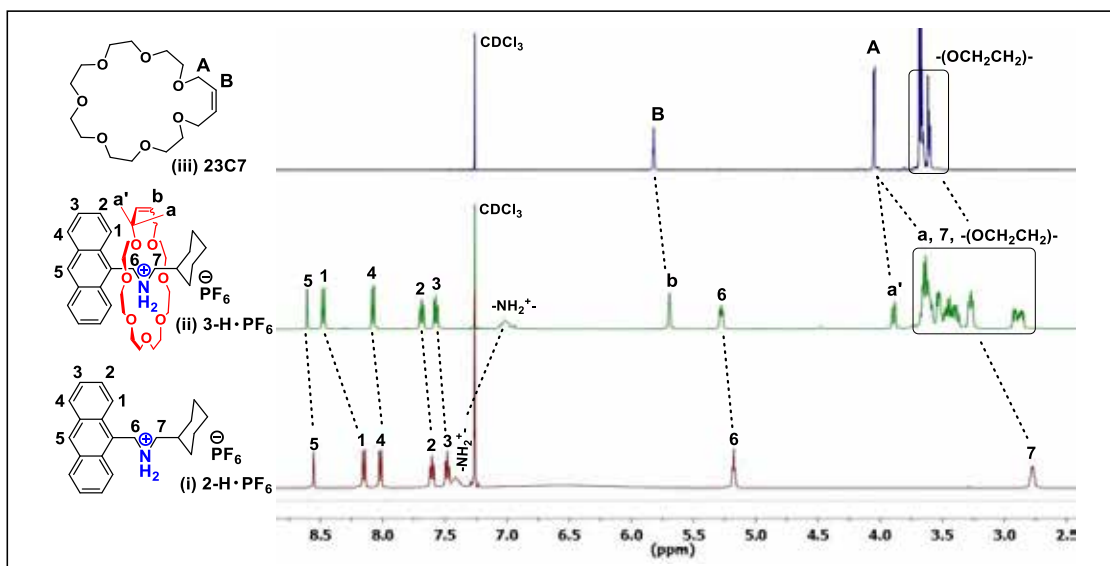


Figure 7. ^1H NMR (500 MHz, CDCl_3 , 10 mM) of (i) axle $2\text{-H}\cdot\text{PF}_6$; (ii) [2]rotaxane $3\text{-H}\cdot\text{PF}_6$; (iii) 23C7. Dotted lines indicate the downfield shifts experienced by the axle component in [2]rotaxane $3\text{-H}\cdot\text{PF}_6$. The upfield shifts and splitting are observed for 23C7 crown ether.

K, neither free macrocycle (23C7) nor free axle ($2\text{-H}\cdot\text{PF}_6$) could be observed. None of the proton NMR peaks of $3\text{-H}\cdot\text{PF}_6$ displayed any shift, splitting or coalescing, during the entire process of heating from 293 K to 373 K (Figure 8), demonstrating the kinetic stability of this [2]rotaxane in non-polar media. Based on the ability of secondary ammonium moieties to undergo ion-pair formation with halide anions in non-polar media,²⁰ we contemplated to investigate the kinetic lability of $3\text{-H}\cdot\text{PF}_6$ in presence of halide anions in CDCl_3 at room temperature.

Stimuli-responsive investigations of $3\text{-H}\cdot\text{PF}_6$

Accordingly, a 10 mM equimolar mixture of $3\text{-H}\cdot\text{PF}_6$ and TBAF was instantaneously characterized by ^1H NMR

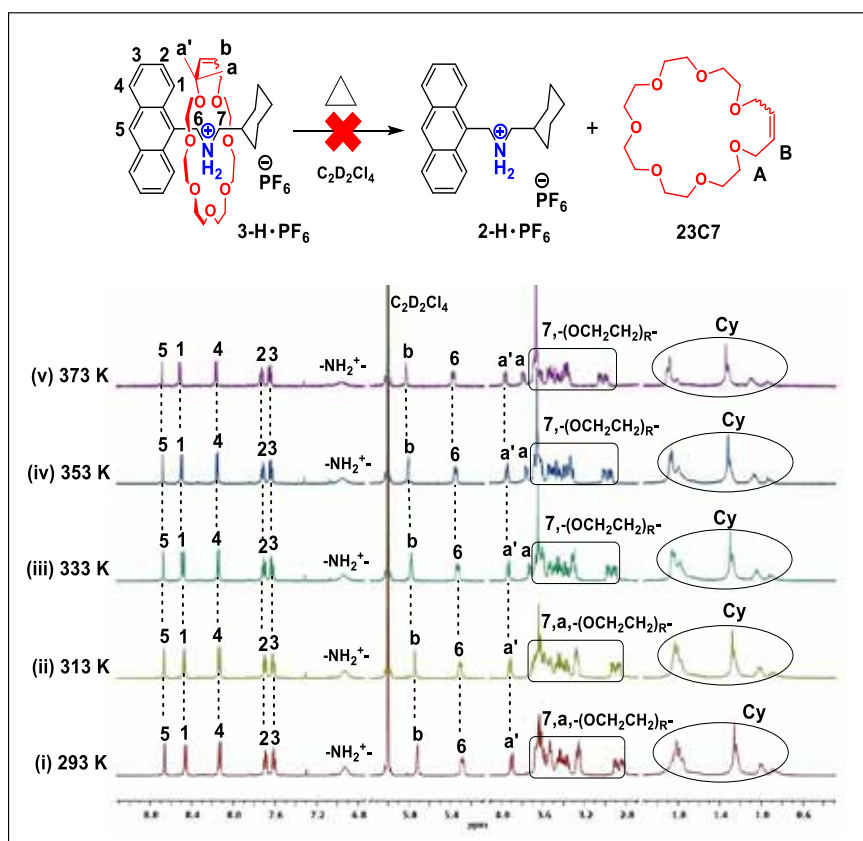


Figure 8. Stack ^1H NMR (500 MHz, $\text{C}_2\text{D}_2\text{Cl}_4$, 10mM) spectrum of [2]rotaxane $3\text{-H}\cdot\text{PF}_6$ at i) 298 K; ii) 313 K; iii) 333 K; iv) 353 K; v) 373 K. There is neither generation of new peaks corresponding to the free axle and 23C7, nor any peak shift observed until heating at 373 K.

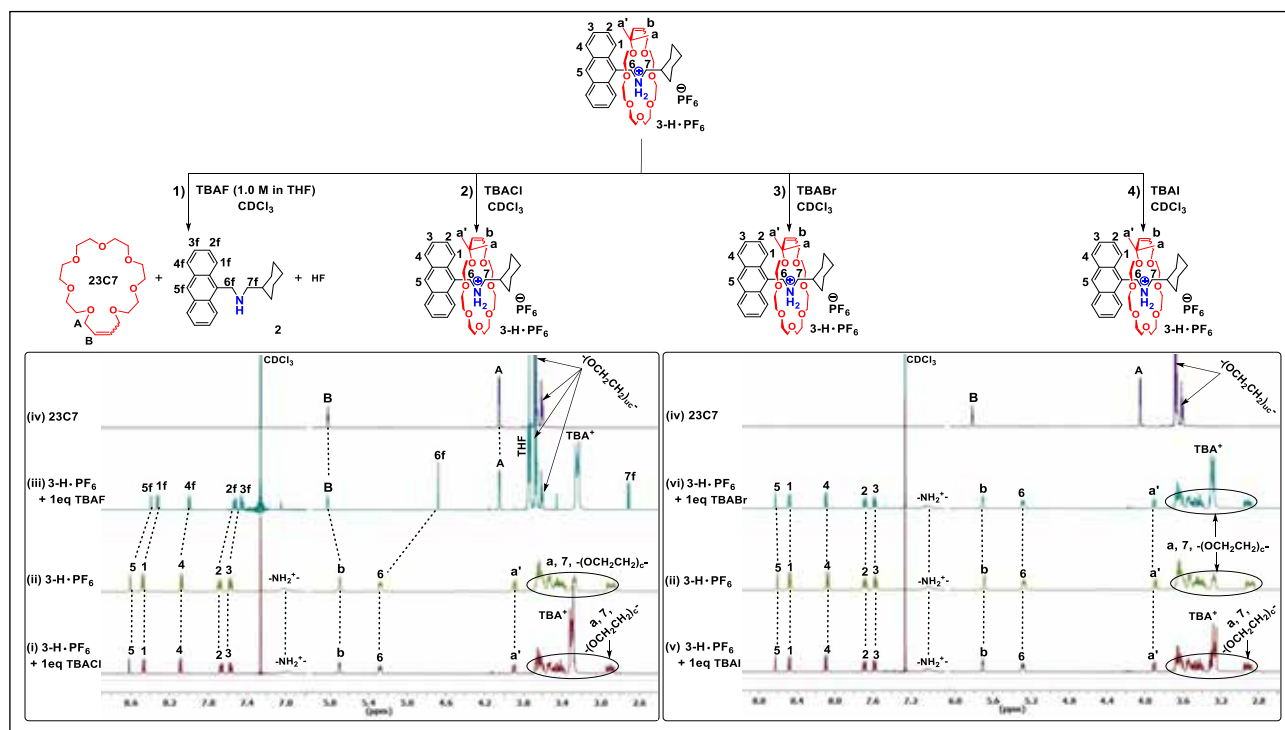


Figure 9. ^1H NMR (500 MHz, CDCl_3 , 10 mM) of (i) $3\text{-H}\cdot\text{PF}_6$ + 1.0 eq. TBACl; (ii) $3\text{-H}\cdot\text{PF}_6$; (iii) $3\text{-H}\cdot\text{PF}_6$ + 1.0 eq. TBAF; (iv) 23C7; (v) $3\text{-H}\cdot\text{PF}_6$ + 1.0 eq. TBAI; (vi) $3\text{-H}\cdot\text{PF}_6$ + 1.0 eq. TBABr.

spectroscopy (**Figure 9(iii)**), which displayed peaks corresponding to the free 23C7 and neutralized axle **2**. As expected, fluoride ion-pair assisted deslippage followed by neutralization,²³ generated axle **2** and HF. The coalescence of H_a & H_a into H_A , merging of glycol protons, downfield shift of H_b to H_B is possible only with the generation of the free macrocycle (**Figure 9(iii)**), whereas the axle protons exhibited upfield shift w.r.t. $3\text{-H}\cdot\text{PF}_6$, and the peak for benzylic protons H_{6n} appeared to be a singlet instead of a multiplet H_6 . Subsequently, equimolar mixture of TBACl and $3\text{-H}\cdot\text{PF}_6$ was investigated. Surprisingly, the ^1H NMR spectrum indicates neither deslippage of the macrocycle 23C7 nor generation of the ion-pair $2\text{-H}\cdot\text{Cl}$ (**Figure 9(i)**). Adding one equivalents of TBABr failed to induce deslippage, as the proton NMR spectrum of the mixture remained identical (**Figure 9(vi)**). Investigation with softer halide anion TBAI neither produced free 23C7 macrocycle nor generated ion-pair $2\text{-H}\cdot\text{I}$ (**Figure 9(v)**), showcasing the fluoride anion selective metastability of $3\text{-H}\cdot\text{PF}_6$!

Buoyed by the selective metastability exhibited for fluoride anions, we intended to exploit the fluorescence response of anthracene moiety in $3\text{-H}\cdot\text{PF}_6$ for the same. Consequently, control study of the axle component, *i.e.* $2\text{-H}\cdot\text{PF}_6$, was performed with TBAX (X = F, Cl, Br, I) in dichloromethane (**Figure 10**). Severe fluorescence quenching of anthracene band was observed upon adding one equivalent TBAF (**Figure 10a**), which remained constant upon further addition, indicating saturation attained. Formation of tight ion-pair in non-polar medium such as dichloromethane, with consequent neutralization resulted in the generation of neutral axle **2**, which accounts for fluorescence quenching via photoelectron transfer (PET) to the anthracene moiety.²⁵ The TBACl addition led to the generation of ion pair $2\text{-H}\cdot\text{Cl}$ in dichloromethane, which caused blue shift of the anthracene band by 3 nm (**Figure 10b**). Next, TBABr addition produced the ion-pair $2\text{-H}\cdot\text{Br}$ in dichloromethane, which exhibited approximately four-fold fluorescence quenching due to heavy atom effect (**Figure 10c**).²⁵

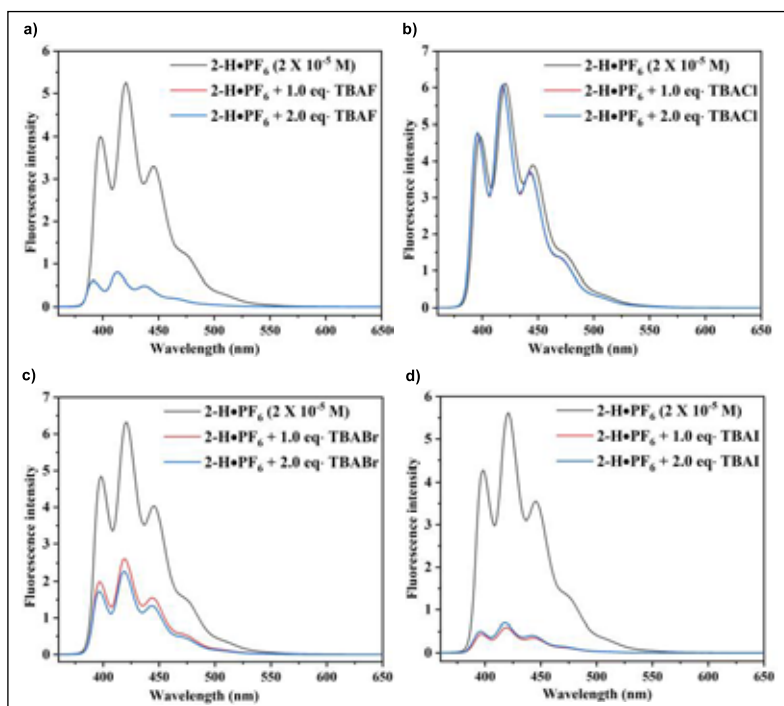


Figure 10. Fluorescence spectra ($\lambda_{exc} = 345 \text{ nm}$, CH_2Cl_2 , 293 K, $2 \times 10^{-5} \text{ M}$) of $2\text{-H}\cdot\text{PF}_6^-$: (i) + 1.0 - 2.0 eq. TBAF, (ii) + 1.0 - 2.0 eq. TBACl, (iii) + 1.0 - 2.0 eq. TBABr, (iv) + 1.0 - 2.0 eq. TBAI.

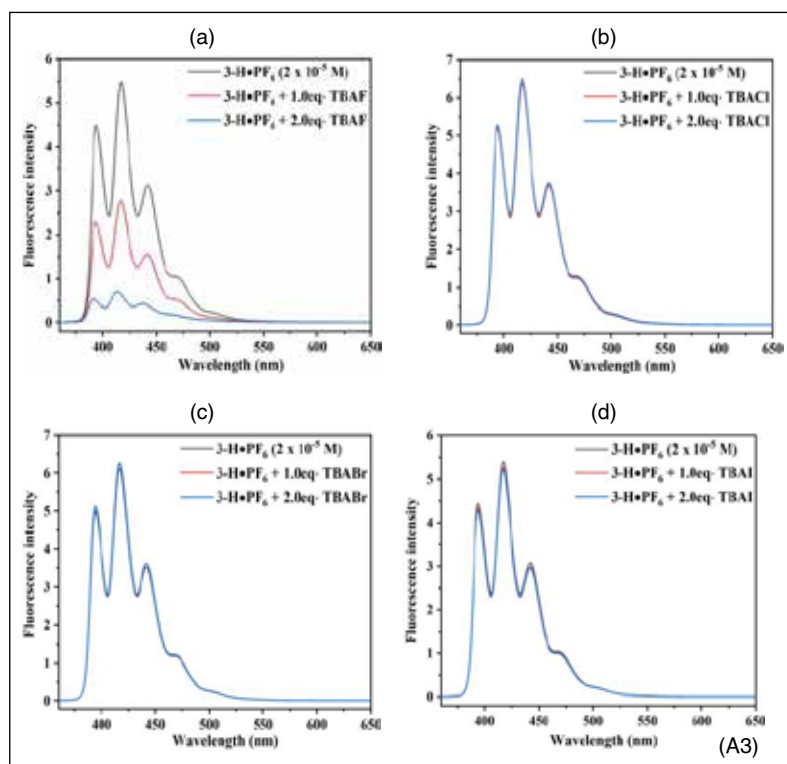


Figure 11. Fluorescence spectra ($\lambda_{exc} = 345 \text{ nm}$, CH_2Cl_2 , 293 K, $2 \times 10^{-5} \text{ M}$) of $3\text{-H}\cdot\text{PF}_6^-$: (i) + 1.0 - 2.0 eq. TBAF, (ii) + 1.0 - 2.0 eq. TBACl, (iii) + 1.0 - 2.0 eq. TBABr, (iv) + 1.0 - 2.0 eq. TBAI.

Likewise, adding TBAI to the axle $2\text{-H}\cdot\text{PF}_6^-$ afforded the ion-pair $2\text{-H}\cdot\text{I}$, which exhibited approximately ten-fold fluorescence quenching (Figure 10d).²⁵

Subsequently, $3\text{-H}\cdot\text{PF}_6^-$ ($2 \times 10^{-5} \text{ M}$) was treated with TBAX in dichloromethane (Figure 11). Two equivalents TBAF addition resulted in ten-fold fluorescence quenching and reproduced similar fluorescence response (Cf. Figure 11a & 10a), due to the generation of the neutralized axle 2. Thus, metastability in $3\text{-H}\cdot\text{PF}_6^-$ could also be followed by spectrofluorimetric method. TBACl addition expectedly did not induce metastability, as no blue shift of the anthracene band could be observed (Cf. Figure 11b & 10b). Furthermore, two equivalents TBABr and TBAI did not invoke any change in the fluorescence output of $3\text{-H}\cdot\text{PF}_6^-$ (Figure 11c & 11d), as expected from the NMR studies.

Control studies with 10 eq. TBAX (X = Cl, Br, I), produced no or marginal fluorescence quenching of anthracene band. Consequently, we switched to a more relevant solvent system for detection of fluoride anion, *i.e.*, acetonitrile containing 0.5% (v/v) water, which turned out to be far more responsive as quenching at saturation is now 108-fold (Figure 12a). Accordingly, limit of detection (LOD) from the TBAF titration was obtained as $7.36 \times 10^{-7} \text{ M}$, using the expression $3\sigma/s$, where “ σ ” is the standard deviation and “ s ” is the slope of the linear fit of calibration curve (Figure 12b). Plot of TBAF titration with $3\text{-H}\cdot\text{PF}_6^-$ ($2 \times 10^{-5} \text{ M}$) in absence and presence of ten equivalents of interfering anions (TBAX, where X =

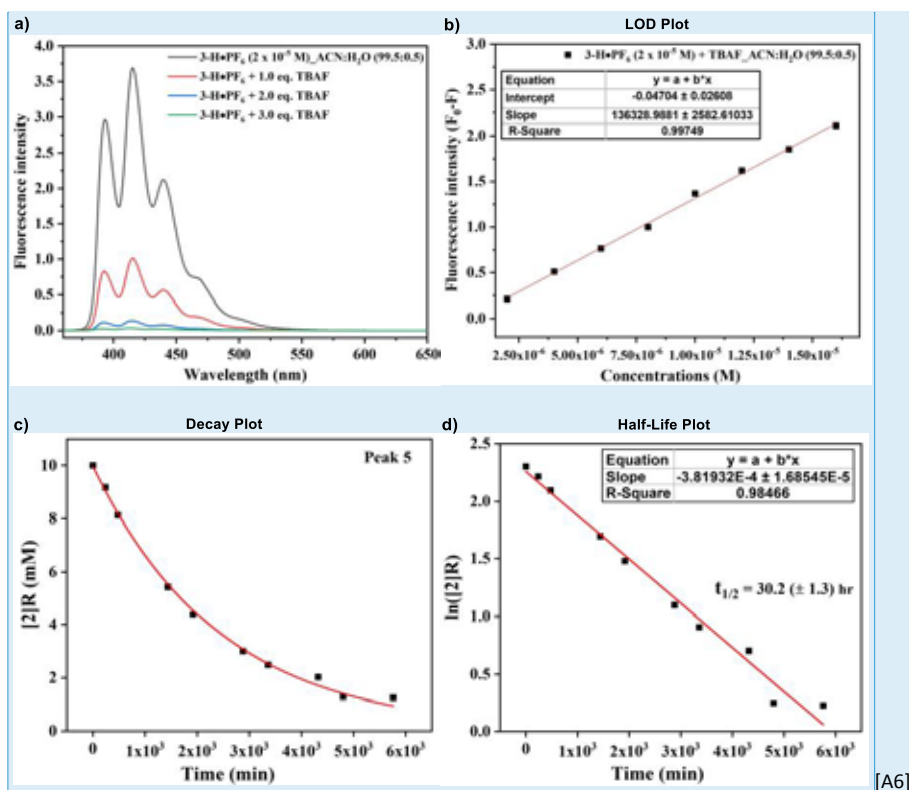


Figure 12. (a) Fluorescence spectra ($\lambda_{exc} = 345$ nm, CH₃CN/H₂O = 99.5/0.5, 293 K, 2×10^{-5} M) of 3-H·PF₆ + TBAF, (b) Linear curve fitting for limit of detection of fluoride anion, (c) Plot of concentration of 3-H·PF₆ (DMSO-*d*₆, 10 mM) w.r.t. time, (d) Plot of logarithmic concentration of 3-H·PF₆ (DMSO-*d*₆, 10 mM) w.r.t. time.

Cl, Br, I), displayed complete superimposition in the region 2-20 PPM, highlighting the selectivity!

Furthermore, metastability of 3-H·PF₆ in polar (DMSO-*d*₆) medium, was probed. Slow deslippage kinetics in 3-H·PF₆ was observed (Figure 12c), which followed a first order decay kinetics with a half-life of 30.2 (± 1.3) hour (Figure 12d).

3. Experimental section

All reagents and starting materials were bought from commercial suppliers and used without further purification. Anhydrous dichloromethane (DCM) was obtained from dry distillation of its analytical grade by refluxing over CaH₂. Anhydrous tetrahydrofuran (THF) was obtained by distilling its analytical grade by refluxing over sodium-benzophenone. Anhydrous acetonitrile and DMF purchased from CDH. Always freshly distilled dry solvents were used.

Column chromatography was performed on silica gel (100-200 mesh). Deuterated solvents (Sigma-Aldrich) for NMR spectroscopic analyses were used as received. All NMR spectra were recorded on Bruker 400 MHz FT-NMR spectrometer or Bruker's Avance-III 500 MHz NMR spectrometers. All chemical shifts are quoted in ppm with multiplicities being denoted by s (singlet), d (doublet), t (triplet), q (quartet), m (multiplet), and br (broad). Mass spectra were recorded in ESI mode on SCIEX X-500R (Q-TOF) Mass spectrometer with Agilent 1200 HPLC system. Structural assignments were made with additional information from NOESY NMR experiments.

Absorption studies were conducted in Thermo Fisher Scientific Evolution 300 spectrophotometer. Fluorescence spectra were recorded in Horiba Scientific Fluoromax-4 spectrofluorometer, where both excitation and emission slit widths are 2 nm.

Synthesis of [2]Rotaxane, 3-H PF₆

Compound 2-H·PF₆ (0.1 g, 0.223 mmol) and P23C7 (0.162 g, 0.45 mmol) were dissolved in the mixed solvent (40 ml, CHCl₃/CH₃CN = 3:1 (v/v)). The solution was stirred for 12 hours, followed by removal of the solvent under vacuum without heating. The residue was dissolved in dry DCM (180 ml, 0.0025 M) under nitrogen atmosphere. Grubbs' 2nd generation catalyst (0.019 g, 0.02 mmol, 0.05 eq w.r.t P23C7) was added and the resulting mixture was refluxed for 60 hours. The reaction mixture was cooled and quenched with ethyl vinyl ether. The excess solvent was removed in vacuum and the residue was subjected to

column chromatography (silica gel: Acetone/DCM = 1:20) to give the desired product **3-H** PF₆ (0.139 g, 79 %). ¹H NMR (500 MHz, CDCl₃): δ ppm = 8.60 (s, 1H, Ar), 8.48 (d, *J* = 8.8 Hz, 2H, Ar), 8.08 (d, *J* = 8.8 Hz, 2H, Ar), 7.69-7.66 (m, 2H, Ar), 7.58-7.55 (m, 2H, Ar), 7.02 (br, 2H, NH₂⁺), 5.69 (br, 2H, C(H)=C(H)), 5.29-5.26 (m, 2H, C(H₂)NH₂⁺), 3.90 (d, *J* = 9.1 Hz, 2H, C(H₂)C=C of 23C7), 3.67-3.36 (br, 2H+2H+20H, C(H₂)C=C of 23C7 + NH₂⁺C(H₂)Cy + OCH₂CH₂), 2.90-2.84 (m, 4H, OCH₂CH₂), 1.80-1.72 (br, 6H, Cy), 1.21-1.20 (br, 3H, Cy), 1.02-0.95 (br, 2H, Cy). ¹³C{¹H} NMR (125 MHz, CDCl₃): δ ppm = 131.18, 131.10, 130.5, 130.3, 129.3, 127.5, 125.6, 124.3, 122.2, 71.6, 71.0, 70.95, 70.91, 70.7, 70.6, 70.1, 55.9, 45.9, 35.7, 30.6, 25.9, 25.8. HRMS (ESI) *m/z*: [M-PF₆]⁺ Calcd for C₃₈H₅₆NO₇, 638.4051; Found 638.4042.

4. Conclusions

In conclusion, we employed a pseudo[2]rotaxane (**1-H**BP23C7·PF₆) for halide anion responsive investigation, whereby fluorescence “turn-on” of the macrocycle BP23C7 could be observed with concomitant fluorescence quenching of the anthracene band of the axle. However, this system could not distinguish between fluoride and chloride anions, although fluoride anion caused much sharper fluorescence quenching of the anthracene band. So, an anthracene stoppered metastable [2]rotaxane (**3-H** PF₆) comprising a cyclohexyl end group was synthesized by RCM in very good yield (79%). Replacing linear hexyl chain of **1-H** PF₆ with a bulkier cyclohexyl end group in **3-H** PF₆ would definitely restrict the freedom of the macrocycle to get disassembled or extrude from the axle, which might enhance the selectivity towards fluoride anion over other halide anions. Surprisingly, **3-H** PF₆ exhibited metastability only in presence of fluoride anions, while excess chloride, bromide and iodide anions did not perturb the integrity of **3-H** PF₆, signifying a correlation between selectivity in anion recognition with the bulk of slippage stoppers. Furthermore, the anthracene component in **3-H** PF₆ enabled selective detection of fluoride anion through fluorescence turn-

off by PET, with the LOD being 7.3 × 10⁻⁷ M in acetonitrile containing 0.5% (v/v) water. Besides, the metastability in **3-H** PF₆ could also be manifested in polar medium (DMSO-d₆), whereby slow deslippage kinetics of 23C7 was observed. This concept of halide anion induced metastability of [2]rotaxanes offers both novelty and practical applications, which can be extended for cation recognitions as well. In essence, we have developed a fluoride anion selective sensor based on a [2]rotaxane architecture, using the concept of metastability.

5. Acknowledgement

Financial support from RSC Research Fund (R21-1196462483) and DST-SERB (ECR/2016/001724) is gratefully acknowledged. M. Jaiswal thanks NIT Patna for scholarship. We thank SAIF & Department of Chemistry IIT Patna, SAIF CDRI Lucknow and IISER Bhopal for all NMR and HRMS characterizations.

6. Reference

1. C. J. Bruns and J. F. Stoddart, “*The Nature of the Mechanical Bond: From Molecules to Machines*,” John Wiley & Sons, Inc.: Hoboken, NJ (2016).
2. S. Dasgupta and J. Wu in “*Comprehensive Supramolecular Chemistry II*,” Vol. 6 (Ed.: J. L. Atwood), Elsevier, Amsterdam (2017) pp. 251.
3. M. Xue, Y. Yang, X. Chi, X. Yan and F. Huang, *Chem. Rev.*, **115** (2015), 7398.
4. L. Chen, X. Sheng, G. Li and F. Huang, *Chem. Soc. Rev.*, **51** (2022), 7046.
5. V. Fasano, M. Baroncini, M. Moffa, D. Iandolo, A. Camposeo, A. Credi and D. Pisignano, *J. Am. Chem. Soc.*, **136** (2014), 14245.
6. J. T. Wilmore and P. D. Beer, *Adv. Mater.* **36** (2024), 2309098.
7. A. Docker, Y. C. Tse, H. M. Tay, A. J. Taylor, Z. Zhang and P. D. Beer, *Angew. Chem., Int. Ed.*, **61** (2022), e202214523.
8. C. Yang and H. Chen, *ACS Appl. Nano Mater.*, **5** (2022), 13874.
9. Y. Ren, R. Jamagne, D. J. Tetlow and D. A. Leigh, *Nature*, **612** (2022), 78.
10. B. H. Wilson and S. J. Loeb, *Chem*, **6** (2020), 1604.
11. M. J. Power, D. T. J. Morris, I. J. Vitorica-Yrezabal and D. A. Leigh, *J. Am. Chem. Soc.*, **145** (2023), 8593.
12. J. R. J. Maynard and S. M. Goldup, *Chem*, **6** (2020), 1914.
13. K. Eichstaedt, J. Jaramillo-Garcia, D. A. Leigh, V. Marcos, S. Pisano and T. A. Singleton, *J. Am. Chem. Soc.*, **139** (2017), 9376.
14. E. Aznar, M. Oroval, L. Pascual, J. R. Murguía, R. Martínez-Mánez and F. Sancenón, *Chem. Rev.*, **116** (2016), 561.
15. Y. Zhou, L. L. Tan, Q. L. Li, X. L. Qiu, A. Di Qi, Y. Tao and

- Y. W. Yang, *Chem. Eur. J.*, **20** (2014), 2998.
16. S. Erbas-Cakmak, D. A. Leigh, C. T. McTernan and A. L. Nussbaumer, *Chem. Rev.*, **115** (2015), 10081.
 17. S. Ahmad, R. Singh, T. Arfin and K. Neeti, *Environ. Sci. Adv.*, **1** (2022), 620.
 18. M. J. Langton, O. A. Blackburn, T. Lang, S. Faulkner and P. D. Beer, *Angew. Chem., Int. Ed.*, **53** (2014), 11463.
 19. Q. Li, Y. Wu, Y. Liu, L. Shangguan, B. Shi and H. Zhu, *Org. Lett.*, **22** (2020), 6662.
 20. H. Zhang, J. Hu and D. H. Qu, *Org. Lett.*, **14** (2012), 2334.
 21. M. Montalti and L. Prodi, *Chem. Commun.*, **2** (1998), 1461.
 22. E. Ishow, A. Credi, V. Balzani, F. Spadola and L. Mandolini, *Chem. Eur. J.*, **5** (1999), 984.
 23. K. Nakazono and T. Takata, *Chem. Eur. J.*, **16** (2010), 13783.
 24. S. Dasgupta and J. Wu, *Chem. Sci.*, **3** (2012), 425.
 25. A. Chmyrov, T. Sandén and J. Widengren, *J. Phys. Chem. B* **114** (2010), 11282.



Dr. Suvankar Dasgupta completed his B.Sc chemistry from presidency university (erstwhile presidency college) in 2005. He obtained his masters in chemistry from IIT Madras, Chennai in 2007. Then, he received his PhD degree in chemistry from National University of Singapore, Singapore in 2012. After postdoctoral stints in NTU, Singapore and IISc Bangalore, he joined department of chemical science and technology (erstwhile department of chemistry) in December 2014. His research interest includes supramolecular chemistry, host-guest based assemblies, mechanically interlocked molecules, responsive pseudorotaxanes, metastable rotaxanes, rotaxane-based molecular switches in solutions and on nanoparticle surfaces.



Mr. Mukesh Jaiswal received his Integrated M.Sc. Degree in Chemistry from National Institute of Technology, Patna in 2020. He joined department of chemical science and technology (erstwhile department of chemistry), NIT Patna in 2022 as a PhD research scholar under the supervision of Dr. Suvankar Dasgupta. His research topic includes investigation of metastability and molecular switchability in rotaxanes, in response to stimuli such as fluoride and cyanide.

Unravelling Cyanide Sensing Mechanisms of Colorimetric and Fluorometric Sensors

G. L. P. Anisha[‡], S. S. B. Rayudu[‡], Dhananjay[‡], R. K. Kanaparthi^{‡*}

[‡]Department of Chemistry, Central University of Kerala, Tejaswini Hills, Periyar PO, Kasaragod – 671 320, Kerala, India.

Corresponding Author: rkchem@cukerala.ac.in

Abstract

This mini review article presents various mechanisms for detecting cyanide, a highly toxic chemical with widespread industrial uses. Four main sensing mechanisms: Intramolecular Charge Transfer (ICT), Aggregation Induced Emission (AIE), Single Electron Transfer (SET), and Excited State Intramolecular Proton Transfer (ESIPT) are discussed highlighting their strengths and limitations, including detection limits and practical applications. The review also discusses challenges, such as reproducibility and real sample analysis, and suggests future research directions for improving cyanide sensors.

1. Introduction

Cyanide is a highly toxic chemical compound containing a cyano group (CN), consisting of a carbon atom triple-bonded to a nitrogen atom. It can exist in various forms, such as hydrogen cyanide gas, cyanide salts (e.g., potassium cyanide), and cyanogenic compounds in plants. Cyanide interferes with cellular respiration by inhibiting cytochrome c oxidase, an enzyme crucial for energy production in cells. This blockage prevents cells from using oxygen, leading to rapid suffocation of tissues and organs. Cyanide poisoning can occur through inhalation, ingestion, or skin absorption, and is potentially fatal if not treated immediately. The WHO has suggested a short-term health-based value for cyanide in drinking water (0.17 mg/L), which is considered extremely conservative, in light of the cyanide toxicity issues mentioned above. Cyanide is widely used in the mining industry to extract gold and silver from ores through a process called cyanidation. In this process, cyanide dissolves the gold or silver from the rock, allowing it to be separated and purified [1]. Cyanide is an essential building block in the synthesis of various chemicals. For example, for the synthesis of acrylonitrile used in the production of plastics, synthetic rubber, and fibers [2]. Similarly, cyanide

is the main source for synthesizing many nitrile compounds that include adiponitrile in the nylon production [3]. Cyanide is the main ingredient for synthesizing hydrogen cyanide which is the precursor for acetonitrile, methyl methacrylate, and various pesticides [2]. Further, cyanide solutions are used in electroplating to deposit metals like gold, silver, copper, and nickel onto surfaces. It has been proved that usage of cyanide solutions ensures a smooth and durable coating on jewellery, electronics, and coins [4].

Despite of its widespread usage in the industry, the cyanide on the other hand found to be notorious because of extreme toxicity. Studies have showcased the fact that cyanide is lethal even at extreme low levels to humans as well as aquatic life. Since, cyanide is widely used across industrial purposes, and is lethal to forms of life, it brings out an urgent need for developing sensors that can detect cyanide in different samples. Considering the significance of cyanide detection, several researchers are working extensively for developing a method/molecular probes. From the last five years 336 articles (Scopus search using 'Cyanide Sensors' as key word) have been published in the literature. In a review article, various scaffolds that have been used for the developing the cyanide sensors

have been discussed [20]. The latest review article highlights exclusively indolium-based fluorescent probes reported in the literature especially their effectiveness and limitations towards cyanide detection [20]. However, there is no review article that gives deeper insights into the various principles involved in the detection of cyanide. To address this gap, herein we provide a comprehensive overview of different cyanide sensing mechanisms that were reported in the literature. We firmly believe that understanding the existing cyanide sensing mechanisms would be a beneficial for developing efficient cyanide sensor for real time applications.

2. Mechanisms for Cyanide Sensing

Four major sensing mechanisms that have been studied extensively for developing cyanide sensors are discussed below.

2.1. Intramolecular Charge Transfer (ICT):

This is the most widely used concept for developing cyanide sensors in which the charge transfer occurs within a single molecule. The ICT involves the movement of an electron from a donor group to an acceptor group within a single molecule. This transfer typically occurs in molecules with conjugated systems, where the electron density can shift between different parts of the molecule, often leading to changes in the molecule's electronic and optical properties.

The ICT is crucial in various fields, such as photochemistry, where it influences absorption and emission spectra, and in organic electronics, affecting the efficiency of light-emitting diodes (LEDs) and solar cells. The phenomenon also plays a role in molecular sensors and fluorescence-based imaging techniques.

Several researchers have made use of ICT phenomena to design novel fluorophores and sensors for cyanide ions (CN^-). A cyanide sensor based on pyrene and dicyanovinyl moieties was reported and it has been observed that the ICT from pyrene to the dicyanovinyl group is responsible for its fluorescence quenching.[5] The detection limit was found to be extremely low as 1.76 nM. Benzothiazole and 1,3-indanedione electron donor-acceptor molecule was demonstrated as efficient cyanide sensor. [6] The nucleophilic addition of cyanide at the vinyl carbon disrupts the ICT and causes dramatic spectral changes, especially, color changes and an increase in fluorescence emission intensity. The detection limit was found to be 5.97 nM. In addition to having a detection limit way less than the permissible limit set by WHO, this cyanide sensor does not respond to any pH changes in the range of 6.0-12.0 making it useful in different environments. The sensor was also exploited in detecting cyanide in real samples and successfully verified the purity of water samples. Further

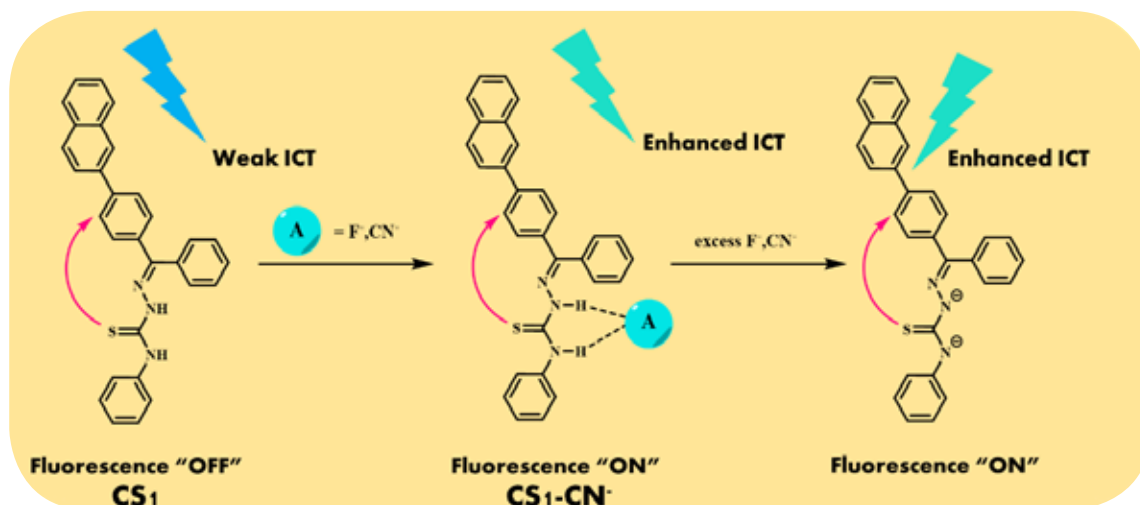


Figure 1. A schematic representation of naphthalene-based cyanide sensing fluorophore via ICT mechanism.

the ICT sensing mechanism was confirmed by $^1\text{H-NMR}$ analysis. The cyanide sensor CS_1 (**Figure 1**) was designed with naphthalene core and an amino-thiourea group [7]. The results suggest that the hydrogen-bonding of the N-H group with F^-/CN^- enhances the ICT character, leading to changes in UV-vis absorption and fluorescence spectra. A new cyanide sensor bearing 3H-benzo[f]chromene core and ethylcyanoacetate was reported and its ICT gets modified due to the loss of π -conjugation, leading to both colorimetric spectral changes and fluorescence quenching.[8] The detection limit was estimated to be $0.70 \mu\text{M}$.

A dicyanovinyl-substituted benzofurazan derivative was demonstrated as an excellent ratiometric chemosensor for detecting cyanide anion in aqueous acetonitrile solution [9]. The results suggest that the nucleophilic addition of cyanide at the α -position of dicyanovinyl group inhibits the ICT character which in turn exhibits a significant shift in both fluorescence emission and absorption. Colorimetric and fluorometric cyanide sensing behavior was further confirmed by the time-dependent density functional theory calculations (TDDFT) revealing that the cyanide attack hinders the ICT character of the molecule.

Another interesting work utilizes an off-the-shelf compound, 6,7-dihydroxycoumarin which forms a complex with copper ions (**Figure 2**) [10]. The detection of cyanide occurs via a

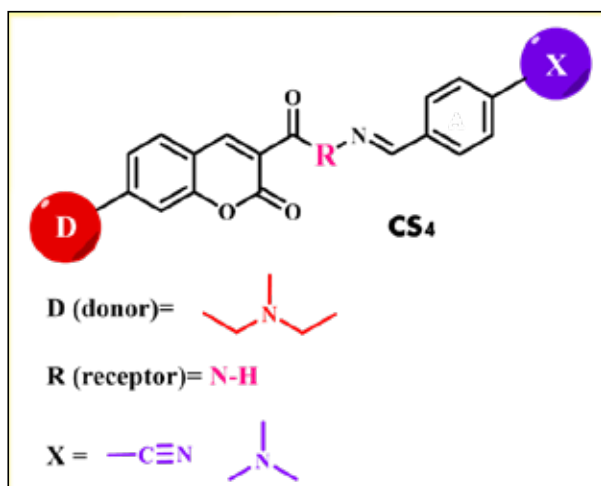


Figure 2. A schematic representation of ICT cyanide sensing mechanism of coumarin based sensor.

metal displacement mechanism, where cyanide displaces copper from the complex, leading to a change in fluorescence. However, this paper does not explicitly discuss about the time needed for detection and just states that the sensing is rapid. The authors did talk about the time taken for cell imaging which is 30 minutes. The displacement of metal ion disrupts the ICT process which is found to be the underlying mechanism for sensing. Not only this work helped the chemists, it was further explored for its clinical applications wherein rat's serum infused with cyanide was tested using the same.

In another research, a high-performance fluorescence chemosensor CS_5 that selectively detects cyanide without interference from other ions [11]. UV-vis and fluorescence spectroscopy were used to evaluate the spectrum responses of CS_5 to cyanide anion (**Figure 3**). The detection limit was reported to be $2.8 \mu\text{M}$ which is substantially lower than the permissible values set by the World Health Organization. The study shows that the interaction between CS_5 and the cyanide ion involves a deprotonation followed by a nucleophilic addition of CN^- at the probe. This process inhibits the ICT, thus quenching the fluorescence. The found results were validated with $^1\text{H-NMR}$, ESI-MS, and Density Functional Theory investigations. Ultimately, the probe CS_5 was successfully exploited to detect cyanide ions in various dietary samples, and then construct an XOR molecular logic gate, thus connecting the realms between organics and semiconductors. In yet another experiment using the ICT mechanism, a group of researchers developed sensors to detect cyanide ions in industrial waste and food samples. Still, it did not provide with specific values of detection limit [12].

The molecule CS_6 is based on a D- π -A (donor- π -acceptor) molecular system (**Figure 4**), with phenothiazine acting as the electron donor and benzothiazole as the electron acceptor. These units are linked by an ethylene group which acts as a π spacer. A biphenyl group is attached to the phenothiazine to enhance its electron-

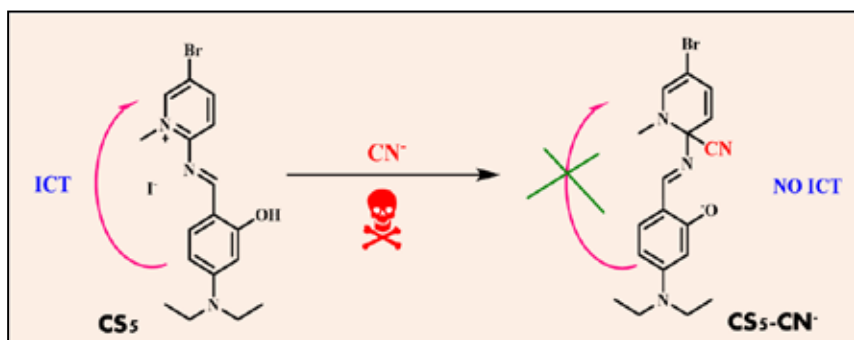


Figure 3. A representation of N-diethyl substituted benzene-based ICT mechanism towards cyanide detection.

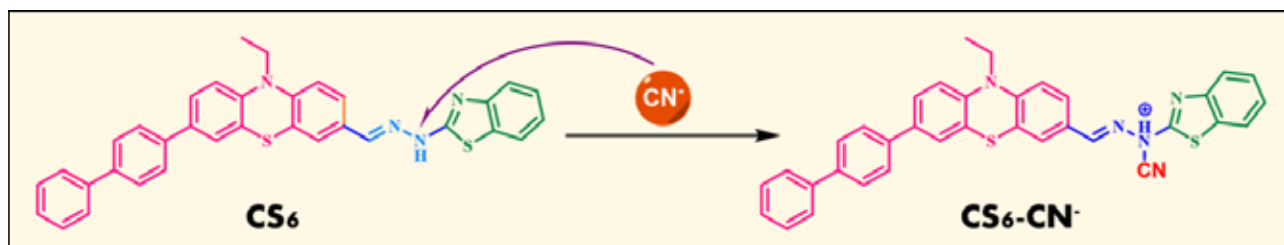


Figure 4. ICT based sensing mechanism of phenothiazine as an electron donor and benzothiazole as an electron acceptor for sensing cyanide ions [21].

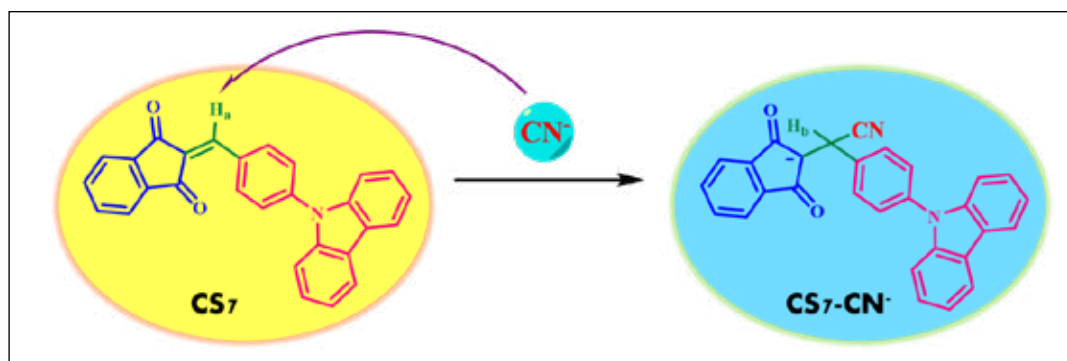


Figure 5. Cyanide sensing mechanism of carbazole based sensor.

donating properties. The -NH moiety of CS₆ interacts with cyanide ions through hydrogen bonding, leading to deprotonation of the -NH group. This deprotonation increases electron density on the conjugated system, enhancing the intramolecular charge transfer (ICT). CS₆ shows high sensitivity and selectivity towards cyanide ions. The detection limit for cyanide using CS₆ sensor is 1.36 μM by UV-vis spectroscopy and 0.13 nM by fluorescence spectroscopy [21].

The molecule CS₇ which has Carbazole moiety as electron donor and 1,3 Indanedione as an electron acceptor in D- π -A architecture discusses about the detection of cyanide in

Tapioca in THF/Water medium (**Figure 5**). The authors focus on discussing about the specificity of the fluorophore for cyanide ions and is attributed to the ICT mechanism. The limit of detection is reported to be 0.43 μM , which is less than the permissible limits set by the World Health Organization [13].

2.2. Aggregation Induced Emission (A.I.E):

Tetraphenylethylene and triphenylamine are commonly studied AIEgens. The phenyl rings are connected to the core group bond in the architecture of propellers attached to a plane. These are highly soluble in common solvents

such as DCM, CHCl_3 , ACN, THF, and DMSO, but are insoluble in water. The rotation of the phenyl rings of the secluded molecules around the core group in solution is very dynamic, converting excitational photon energy into heat. The excited tetraphenylethylene molecules undergo non-radiative decay, leading to quasi-fluorescence in a dilute solution. However, in the case of non-planar tetraphenylethylene, on the other hand upon aggregation or solid state, the rotational motion of phenyl rings is hindered leading to increase in fluorescence emission intensity. Molecules such as tetraphenylethylene can be attacked by nucleophiles like cyanide. The optical characteristics of CS_8 , CS_9 , and CS_{10} in **Figure 6** would be altered by nucleophilic addition of cyanide, which would break off the direct conjugation between the electron donor and acceptor moiety. This explains why the

charge transfer absorption bands of the three compounds collapsed upon the addition of cyanide. Thus, it was hypothesized that anionic species were formed when cyanide was added to the CS_8 , CS_9 , and CS_{10} sequentially. These anionic species, however, seem to be easily protonated. However, these compounds produce blue fluorescence when they aggregate at high water proportions in THF/water mixtures. In 90% water, the $\text{CS}_8\text{-CN}^-$ and $\text{CS}_9\text{-CN}^-$ aggregates had relative quantum yields of 0.22 and 0.21, respectively [14].

This mechanism was further confirmed by conducting ^1H NMR titration experiment of triphenylamine based CS_{11} with sequential addition of CN^- (**Figure 7**). The vinyl proton signal at 7.45 ppm became weaker when CN^- was added, but a new up field peak of hydrogen steadily increased at 5.22 ppm. In the meantime,

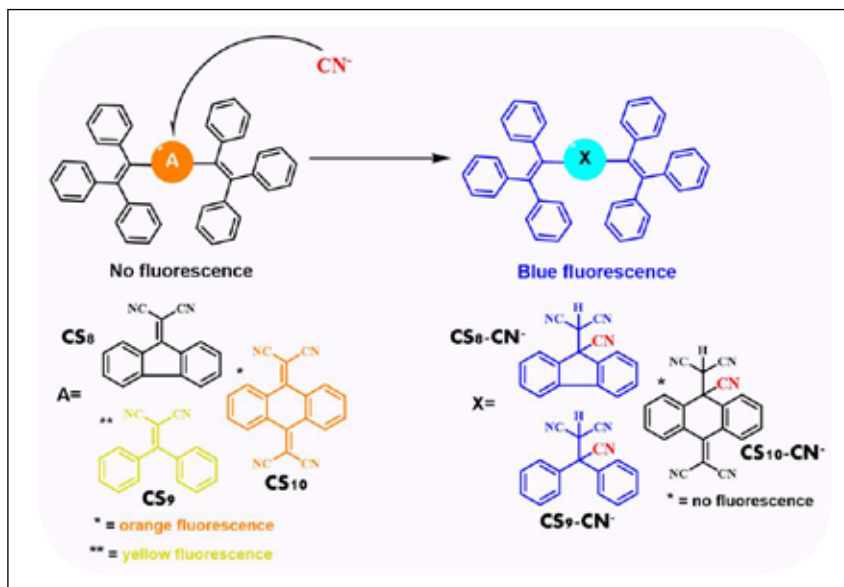


Figure 6. Tetraphenyl ethylene based molecules showing AIE sensing mechanism towards cyanide detection.

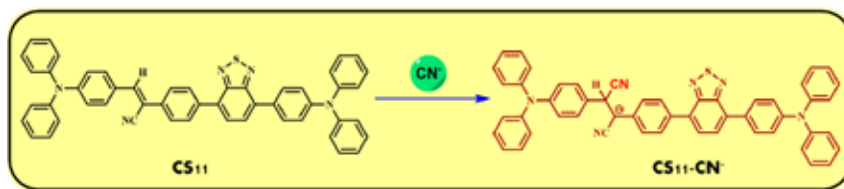


Figure 7. Triphenylamine as donor and benzo[*c*]thiadiazol as acceptor based cyanide sensor via AIE mechanism.

the aromatic protons moved away from their initial locations as cyanide targeted the vinyl group and broke the molecule's conjugation, producing the different types of charge density surrounding the aromatic protons and the fluorescence intensity increased which suggested that the recognition mechanism of nucleophilic addition of cyanide to the vinylic position in $\text{CS}_{11}\text{-CN}^-$ [15].

2.3. Single Electron Transfer (SET) Mechanism:

The single electron transfer (SET) mechanism is a fundamental process in fluorescence that involves the transfer of an electron from the electron rich moiety to electron-deficient moiety to form a radical cation and anion. This mechanism plays a crucial role in various applications, including single-molecule

fluorescence spectroscopy, where it can provide insights into molecular dynamics and interactions within nano-environments. There have been some instances where SET have been employed for cyanide detection (**Figure 8**). To provide multimodal signal outputs, cyanide anion and CS_{12} can react quickly using SET [16]. The $CS_{12}\text{-CN}^-$ radical anion was discovered to have exceptional signal read-out capabilities, spanning from multichannel UV-vis-NIR absorption to scattering (Raman and HRS)-based processes. The cyanide anion can be detected, in particular, using the strong 840 nm NIR absorption peak, without the background interference present in living materials. Crucially, a very sensitive portable electronic gadget has been created using CS_{12} conductive characteristic. With multi-order distinction between closely related anions, the apparatus effectively transforms the SET-based chemical event into an electrical signal output.

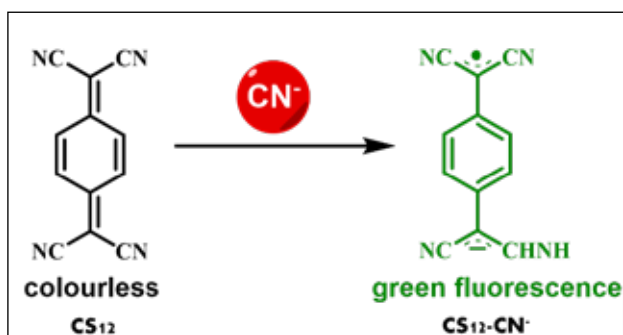


Figure 8. Sensing mechanism of tetracyanoquinodimethane based cyanide sensor via SET.

Another novel SET-driven reaction-based method for cyanide detection using indicators with low LUMO values is described. In addition to producing an air-stable radical anion marker, the cyanide-specific reaction yields multimodal signal outputs due to its spin, charge, and SOMO-LUMO-based electronic transition. Compared to other reducing anions, high selectivity and sensitivity (0.2-16 μM) were noted. This new system of indicators demonstrates dip-stick sensing and regenerability, and it shows how to fabricate an electrical cyanide sensing device [17].

2.4. Excited State Intramolecular Proton Transfer (ESIPT) Mechanism:

Excited state intramolecular proton transfer (ESIPT) is a phenomenon that has the potential to be exploited for cyanide detection in gas phase as well as in non-polar solvents. Compounds that exhibit ESIPT have drawn significant attention because of their potential applications in optical devices that can benefit from the salient properties like ultrafast reaction state and large fluorescent Stokes Shift. In ESIPT-based sensor CS_{13} , a proton is transferred from a hydroxyl group to a nearby acceptor group in the excited state as depicted in **Figure 9**. An intramolecular hydrogen bond facilitates this process and often leads to a shift in the fluorescence emission spectrum [18].

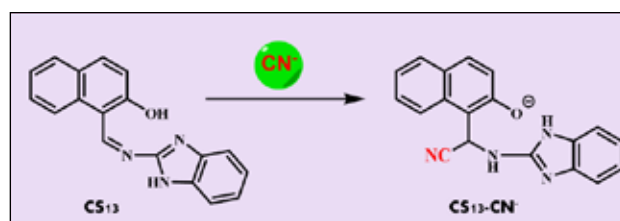


Figure 9. A naphthalene based schematic representation of ESIPT mechanism towards cyanide detection.

The presence of an aldehyde group ortho to the hydroxyl group is crucial for the ESIPT mechanism. This arrangement creates a highly reactive site due to resonance-assisted hydrogen bonding (RAHB) [19]. This also helps in selective and ratiometric detection of cyanide. Upon interaction with cyanide ions, the nucleophilic cyanide attacks the aldehyde group, forming a $CS_{13}\text{-CN}^-$. This reaction disrupts the ESIPT process, which results in changes of the fluorescence signal that can be used to detect the presence of cyanide which is extremely toxic to physiological systems.




3. Challenges and Future Directions

Major challenges for all the reported cyanide sensors that were developed based on different mechanisms (ICT, AIE, SET, ESIPT) are reproducibility, practical utility in

analyzing real samples, stability and durability especially in harsh environmental conditions or in complex sample matrices. Besides, most of the cyanide sensors reported till today are solution based sensors suitable for analyzing liquid samples. Future, research can focus on improving the reproducibility and lifespan of these sensors. The combination of these sensors with microelectronics could lead to on-site, real-time detection. There is growing interest in combining ICT, AIE, SET, and ESIPT-based sensors into multifunctional devices capable of detecting cyanide alongside other pollutants or toxins, improving the versatility of these sensors for complex environmental monitoring applications. The use of these sensor methods could be extended to biological systems, where it is necessary to detect cyanide in human or animal fluids in real time, or to environmental monitoring, where it can be used to quickly identify contamination in soil, water, and air.

4. References:

1. N. Kuyucak and A. Akcil, *Minerals Engineering*. 50-51 (2013) 13-29.
2. J.L. Dubois and S. Kaliaguine, in "Industrial Green Chemistry", (J. L. Dubois and S. Kaliaguine; De Gruyter, Berlin, Boston (2021) 31-62.
3. A. Martin and V.N. Kalevaru, *ChemCatChem*. 2 (2010) 1504-1522.
4. E.C. Gugua, C.O. Ujah, C.O. Asadu, D.V.V. Kallon and B.N. Ekwueme, *Hybrid Adv*. 7 (2024) 100286.
5. T.M. Ebaston, G. Balamurugan and S. Velmathi. *Anal. Methods*. 8 (2016) 6909-6915.
6. D. Jothi, S. Munusamy, S.M. Kumar, S. Enbanathan and S.K. Iyer. *RSC Adv*. 12 (2022) 8570-8577.
7. X.M. Song, H.F. Ye, J.L. Song, Y.J. Xi and Y. Wu. *J. Photochem. Photobiol. A Chem*. 459 (2025) 116069.
8. Y.F. Song, W.N. Wu, X.L. Zhao, Y. Wang, Y.C. Fan, X.Y. Dong and Z.H. Xu. *Spectrochimica Acta - Part A*. 280 (2022) 121540.
9. Z. Liu, X. Wang, Z. Yang and W. He. *J. Org. Chem*. 76 (2011) 10286-10290.
10. R. Kaushik, A. Ghosh, A. Singh, P. Gupta, A. Mittal and D.A. Jose. *ACS Sens*. 1 (2016) 1265-1271.
11. M. Nelson, S. Ayyanar, M. Selvaraj and M.A. Assiri. *J. Mol. Struct*. 1321 (2025) 140018.
12. M.T. Waseem, H.M. Junaid, S. Majeed, A.M. Khan, T. Mahmood and S.A. Shahzad. *Microchem. Journ*. 173 (2022) 107018.
13. M. Singh, S. Nadendla and R.K. Kanaparthi. *J. Photochem. Photobiol. A Chem*. 485 (2025) 115957.
14. M.H. Chua, H. Zhou, T.T. Lin, J. Wu and J. Xu. *J. Mater. Chem. C*. 5 (2017) 12194-12203.
15. K. Deng, L. Wang, Q. Xia, R. Liu and J. Qu. *Sens. Actuators B Chem*. 296 (2019) 126645.
16. M.R. Ajayakumar, K. Mandal, K. Rawat, D. Asthana, R. Pandey, A. Sharma, S. Yadav, S. Ghosh and P. Mukhopadhyay. *ACS Appl. Mater. Interfaces*. 5 (2013) 6996-7000.
17. M.R. Ajayakumar, P. Mukhopadhyay, S. Yadav and S. Ghosh. *Org. Lett*. 12 (2010) 2646-2649.
18. S. Chakraborty, S. Paul, P. Roy and S. Rayalu. *Inorganic Chemistry Comm*. 128 (2021) 108562.
19. S. Goswami, A. Manna, S. Paul, A.K. Das, K. Aich and P.K. Nandi. *Chem. Commun*. 49 (2013) 2912-2914.
20. A. Ranolia, Kiran, J. Sindhu, P. Kumar and S. Kumar. *Coordination Chemistry Rev*. 498 (2024) 215463.
21. P. Jayasudha, R. Manivannan and Y.A. Son. *Spectrochimica Acta - Part A*. 329 (2025) 125512.

	<p>Dr. Ravi Kumar Kanaparathi currently working as Assistant Professor, Department of Chemistry, Central University of Kerala. Dr. Ravi Kumar received M.Sc. (2005) and Ph.D. (2011) degrees from University of Hyderabad. Subsequently, he joined as a Research Associate in CSIR-Indian Institute of Chemical Technology (IICT), Hyderabad, India and worked for two years (2011-2013). Subsequently, he joined in the Department of Chemistry as Assistant Professor in 2013. He received Medal from the University of Hyderabad, CSIR-UGC Junior Research Fellowship (JRF) and Senior Research Fellowship (SRF), and DST-Young Scientist award from DST, Govt. of India. His research group mainly focused on new materials for efficient solar energy harvesting, sensing toxic metals and small molecules, fluorescent molecular nanomaterials and optoelectronic devices. At present, he is actively involved in developing new efficient sensitizers for dye sensitized solar cells (DSSCs) based on tetrapyrrolic (porphyrin, phthalocynine and corroles) systems and fluorescent organic molecules. Dr. Ravi Kumar is an expertise in the fabrication of DSSCs, organic and metal nanoparticles, optical & electron microscopy, studying the ultra-fast dynamics (electron and energy transfer reactions) by steady-state and time-resolved fluorescence techniques.</p>
	<p>Gummadi Leela Prabha Anisha obtained her M.Sc. degree in Chemistry in 2022 from Visvesvaraya National Institute of Technology, Nagpur. Currently a Ph.D. (Chemistry) Student under the supervision of Dr. Ravi Kumar Kanaparathi at Central University of Kerala. Her research interest involves fluorescent molecular materials for bioimaging and biosensing applications.</p>
	<p>Rayudu Surya Sekhar Babu is currently a Ph.D Scholar at Central University of Kerala, Kasaragod. His research interests involve designing and developing fluorescence-based sensors for various applications like OLED, DSSC and monitoring water pollution. He completed his master's degree in chemistry from Central University of Kerala.</p>
	<p>Dhananjay earned his M.Sc. degree in Theoretical and Computational Chemistry in July 2023 from Central University of Punjab. Later that year, he joined his doctorate under the supervision of Dr. Ravi Kumar Kanaparathi at Central University of Kerala. His research interests lie in theoretical exploration of materials for optical and energy harvesting applications.</p>



INDIAN SOCIETY FOR RADIATION AND PHOTOCHEMICAL SCIENCES

(Reg. No. 617/1985, GBBSB, Bombay; Trust No. F-10965)

Radiation & Photochemistry Division

Bhabha Atomic Research Centre, Mumbai - 400 085

Member Enrolment Form

1. Name in Block Letters:
2. Date of Birth:
3. Highest Academic Qualification:
4. Present Position:
5. Addresses:

Photograph

Office	Residence
Telephone	Telephone
E-mail	E-mail

6. Address for Correspondence: Office / Residence
7. Category of Membership Applied for: Annual / Life / Corporate member

Category	Fees	Admission fee	Total Amount
Annual	Rs 200/-	Rs 100/-	Rs 300/-
Life Member	Rs 2000/-	Rs 100/-	Rs 2100/-
Corporate Member	Rs 20000/-	Rs 1000/-	Rs 21000/-

8. *Remittance: DD in favour of 'ISRAPS' payable at MUMBAI
For Bank Transfer:

A/c No.10536133801, SBI, BARC Branch, IFSC SBIN0001268
(e-mail the money transfer details along with the details requested above
to: israps.secretary@gmail.com and copy to mathip@barc.gov.in)

**Payment can be made after the approval of application by Secretary, ISRAPS*



9. Brief Resume of activities and research interests:
(min. 500 words, in a separate attachment)
10. List of memberships of other professional bodies, if any:
11. List of prizes/awards/fellowships received, if any:
12. Number of Publications
(Pl. attach complete list)

I agree to abide by the constitution and bye-laws, and rules and regulations of the SOCIETY.

Place:

Signature

Date:



40 years of serving Indian Research Community

SIMCO

most trusted technology trade partner

share your research and requirement: contact@simcoglobal.com

OEMs SIMCO represents

PICOQUANT

TOPTICA

MPD
MICRO PHOTON DEVICES

NIREOS

AIXTRON

Quantum Opus

SLT
Sensor- und Lasertechnik

piezosystemjena
incredibly precise

Laurell

KLOE

SAMCO
PARTNERS IN PROGRESS

ibs
Innovative Ion Implant

HARRICK
PLASMA

SRS
Stanford Research Systems

OAI

LUMIBIRD
MORE THAN LASERS

PACIFIC
LASERTEC™

protemics

core crystal

pi imaging



www.simcoglobal.com

<https://www.linkedin.com/company/simcogts/>



IBACO SERVICES

IBACO SERVICES

INNOVATIVE.. BOLD.. ADAPTABLE.. COMMITTABLE..



CUSTOMIZED GLOVE BOX



AUTO DESICCATOR



ROTARY EVAPORATOR



MOBILE FUME HOOD

RK Chambers, Door no. 7-8-38 ,3rd Floor , Opp EleCtrical Sub Station , Gajuwaka,Visakhapatnam,A.P : 530026
Ph No : 0891-2512719 (Fax) , 09848404144.



With Best Compliment from :

Analytical Instruments Sales & Service Pvt.Ltd.

P-123, C.I.T Road, Scheme IV M, Belegkata, Kolkata-700010

The market leader in Spectroscopy.

We are representing HORIBA in Fluorescence Spectroscopy, Particle Size Analyzer, Raman Spectroscopy.

We are also dealing with Probe Sonicator, Freeze Dryer and other Laboratory Instruments.



Transient Absorption Setup



Raman Spectrometer



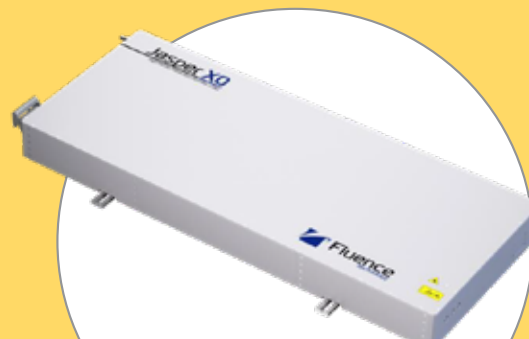
Class AAA Small Light Spot Solar Simulator



Quantum Optical Components



2 Photon Microscopy Laser



Fiber fs Laser for Micromachining

CONTACT DETAILS

sales@trokutsolutions.com, www.trokutsolutions.com, +91-22-40124404

IT'S WHAT'S INSIDE THAT COUNTS...

FLUORESCENCE

- SNR 10,000:1
- UV-VIS-NIR measurement
- TCSPC down to 25ps
- Micro-PL upgrade



F5

FLUORESCENCE



FLS1000

- SNR 35,000:1
- Hexagonal sample chamber
- AGILE supercontinuum Laser
- Customized design and configuration

CONFOCAL RAMAN

- Truly Confocal
- Integrated narrowband Raman Laser
- Five position grating turret
- InGaAs array, CCD, EMCCD

RM5



CONFOCAL RAMAN



RMS1000

- Truly Confocal
- Dual Spectrograph
- Four simultaneous detector
- FLIM, PL microscopy, Time-resolved



EDINBURGH
INSTRUMENTS

DISCOVER THE
SPECTROSCOPY



Contact: Mr. Rajib Saha | +91 9748191360 | rajib@simc.co.in

Contents

Message from the President and Secretary, ISRAPS	i
Editor's Desk	iii
Probing conformational preferences of small peptides in condensed and gas phase	1
<i>S. Kumar, S. Mandal and A. Das</i>	
Versatility of Carbon Dots as a Photosensitizer	14
<i>Somen Mondal</i>	
Design of Defect Engineered Intrinsic White Light Emitting Non-Rare-Earth Phosphors: State-of-the-art	20
<i>A. K. Dehury, R. Kaında, S. Khatoı, R. C. Mallick and Y. S. Chaudhary</i>	
Water radiolysis and its impact on reactor materials	34
<i>R. Puspallata, D. Mal, L. Muniasamy, R. Ramakrishnan, S. Bera and T.V. Krishna Mohan</i>	
Extensive Modulation of Fluorescence Quantum Yield in Quantum Dots by the Presence of Permanent Dark Particles: A Single Particle Level Study	42
<i>K. Kaushik, C. Rao, A. Salam and C. K. Nandi</i>	
Application of Pseudorotaxane and Rotaxane in Anion-Responsive Studies	51
<i>M. Jaiswal and S. Dasgupta</i>	
Unravelling Cyanide Sensing Mechanisms of Colorimetric and Fluorometric Sensors	63
<i>G. L. P. Anisha, S. S. B. Rayudu, Dhananjay, R. K. Kanaparthi</i>	